

PROMPT PHOTONS IN PHOTOPRODUCTION AND DEEP INELASTIC
SCATTERING AT HERA

by

ERIC C BROWNSON

A dissertation submitted in partial fulfillment of the
requirements for the degree of

DOCTOR OF PHILOSOPHY
(PHYSICS)

at the

UNIVERSITY OF WISCONSIN – MADISON

2008

© Copyright by Eric C Brownson 2008

All Rights Reserved

Abstract

Isolated prompt photons with an associated jet in photoproduction with the ZEUS detector at HERA have been measured using an integrated luminosity of 77 pb^{-1} . Differential cross sections are presented for the photon transverse energy and pseudorapidity range $5 < E_T^\gamma < 16 \text{ GeV}$, $-0.74 < \eta^\gamma < 1.1$ with an associated jet in the transverse energy and pseudorapidity range of $6 < E_T^{jet} < 17$, $-1.6 < \eta^{jet} < 2.4$. The differential cross section for the fraction of the exchange photon's momentum involved in the hard scatter has also been measured.

Isolated prompt photons in deep inelastic scattering have also been measured using an integrated luminosity of 109 pb^{-1} . Cross sections are presented for the photon transverse energy and pseudorapidity range $5 < E_T^\gamma < 20 \text{ GeV}$, $-0.7 < \eta^\gamma < 0.9$ without an associated jet requirement.

Acknowledgements I would like to thank the University of Wisconsin Physics Department for the opportunity to learn and perform research with an outstanding group of physicists at an outstanding university. I would especially like to acknowledge the guidance, support, and dedication of Wesley Smith and Don Reeder throughout my graduate school experience. Alexandre Savin, Dorian Kçira, and Sergei Chekanov are owed a special acknowledgment for the guidance they provided while I was at DESY.

I would also like to thank the members of the ZEUS Collaboration who made this analysis possible. A very special thanks are due to my colleagues from Argonne National Laboratory and the University of Glasgow whose tireless dedication to the advancement of physics has been essential to the success of this analysis.

I give special thanks to my parents and family for all of their support and encouragement.

Contents

Abstract	i
Acknowledgements	ii
1 Introduction	1
1.1 The Standard Model	2
1.1.1 Leptons and Quarks	3
1.1.2 Bosons	4
1.2 Quantum Electrodynamics	4
1.3 Quantum Chromodynamics	5
1.3.1 Perturbative Quantum Chromodynamics	5
1.4 Lepton Nucleon Scattering	7
1.4.1 Photoproduction	9
1.4.2 Deep Inelastic Scattering	10
1.4.3 Cross Section and Structure Functions	10
1.4.4 Prompt Photons	12
1.4.5 Prompt Photons in ep Scattering at ZEUS	13

2	Experimental Studies of Prompt Photons	15
2.1	Prompt photons at the Tevatron	16
2.1.1	D0	16
2.1.2	CDF	18
2.2	Large Hadron Collider	19
3	Experimental Setup	21
3.1	Deutsches Elektronen Synchrotronen	21
3.2	HERA Accelerator	22
3.2.1	Lepton Injection and Acceleration	25
3.2.2	Proton Injection and Acceleration	25
3.2.3	Beam Circulation and Collision	27
3.3	Particle Interactions	27
3.3.1	Definitions	28
3.3.2	Electromagnetic Showers	30
3.3.3	Hadronic Showers	31
3.4	ZEUS Detector	31
3.4.1	ZEUS Co-ordinate System	34
3.4.2	Uranium Calorimeter	35
3.4.3	ZEUS Barrel Presampler	38
3.4.4	Central Tracking Detector	39
3.4.5	ZEUS trigger System	40
4	Monte Carlo Simulation	47
4.1	Event Generators	48

4.2	Hard Scatter and QCD Radiation	49
4.3	Hadronization	50
4.3.1	Lund String Model	50
4.3.2	Cluster Model	51
4.4	Detector Simulation	51
4.5	MC programs in HEP	53
4.5.1	PYTHIA Monte Carlo Model	54
4.5.2	HERWIG Monte Carlo Model	55
4.5.3	ARIADNE Monte Carlo Model	55
5	Event Reconstruction and Selection	57
5.1	Track and Vertex Reconstruction	57
5.2	Calorimeter Reconstruction	59
5.2.1	Calorimeter Cell Removal	60
5.2.2	Island Formation	60
5.3	Energy Flow Objects (EFO)	61
5.4	Jet Reconstruction	62
5.4.1	Cone Algorithm	64
5.4.2	k_T Cluster Algorithm (KTCLUS)	65
5.5	Electron Reconstruction	66
5.5.1	SINISTRA	67
5.5.2	ELEC5	68
5.6	DIS Kinematic Reconstruction	69
5.6.1	Electron Method	71

5.6.2	Double-Angle Method	71
5.6.3	Jacquet-Blondel Method	72
5.7	Photoproduction Kinematic Reconstruction	72
5.8	Event Selection	73
5.8.1	Offline Selection	74
5.8.2	PHP Kinematic Requirements	74
5.8.3	Jet Selection	75
5.8.4	DIS Kinematic Requirements	76
6	Photon Selection and Reconstruction	83
6.1	General Photon Requirements	85
6.2	ELEC5	85
6.3	KTCLUS	86
6.4	Photon Energy Corrections	87
6.5	f_{max}	88
6.6	$\langle \delta z \rangle$	89
6.7	Barrel Preshower Detector (BPRES)	90
6.8	Methods of photon identification using Shower Shapes and BPRES	92
7	Deeply Virtual Compton Scattering Studies	99
7.1	Introduction to DVCS	99
7.2	Event Selection	100
7.3	DVCS Simulation	101
7.4	Comparisons	102

8 Prompt photons plus jet in photoproduction	119
8.1 Prompt Photon with jet + Inclusive Dijet MC Sample	120
8.2 Correction Factor	126
8.3 Systematic Uncertainty Estimates	127
8.4 Cross sections	129
8.4.1 Comparison with H1 Results	133
9 Inclusive prompt photons in DIS	145
10 Summary	153

List of Tables

1.1	The quarks and leptons organized into their generations in order of increasing mass.	3
1.2	The bosons and their properties in the Standard Model.	4
3.1	The integrated luminosity delivered by HERA to ZEUS and the gated (recorded for physics) luminosity recorded by ZEUS for each year of HERA operation.	24
8.1	The measured prompt photon with jet in photoproduction cross section with the χ^2 per-degree-of-freedom minimum for the χ^2 fit on the BPRE distribution. The fraction of the combined prompt photon with jet + inclusive dijet MC that is from the prompt photon with jet MC is also given as the “% signal MC”.	126
8.2	The differential prompt-photon with associated jet in PHP cross sections measured in the region $5.0 < E_T^\gamma < 16.0$ GeV, $-0.74 < \eta^\gamma < 1.1$, $6.0 < E_T^{jet} < 17.0$ GeV, $-1.6 < \eta^{jet} < 2.4$, $0.2 < y < 0.8$, $Q^2 < 1$ GeV ² , and $E_T^{\gamma,(true)} > 0.9E_T^\gamma$. The uncertainties shown are statistical.	132

9.1	The measured prompt photon in DIS cross sections and χ^2 per-degree-of-freedom minimums for the different χ^2 fits for the ratio of prompt-photon PYTHIA DIS MC to inclusive background ARIADNE DIS MC. The contribution to the uncertainty by the χ^2 fit is listed separately and in parentheses.	148
-----	--	-----

List of Figures

1.1	Generic diagrams of LO, NLO, and NNLO pQCD calculations.	6
1.2	A general diagram of an interaction between a lepton with momentum k and a hadron with momentum p mediated by an exchange boson with momentum $q = k - kt$	8
1.3	The leading order diagrams for direct photoproduction (left) and resolved photoproduction (right).	9
2.1	The intrinsic momentum of partons within the proton verses the γp center-of-mass energy for several different experiments.	16
2.2	Dependence of photon purity on P_T^γ for center of mass energy of $\sqrt{s} = 1.96$ TeV at D0.	17
2.3	D0 measurement at the center of mass energy, $\sqrt{s} = 1.96$ TeV of the P_T^γ dependence of the isolated photon cross section (Left) and the ratio of the measured cross section to the NLO pQCD calculation from JETPHOX (Right).	18

2.4	The CDF measurement at the center of mass energy of $\sqrt{s} = 1.8$ TeV of the P_T dependence of the isolated prompt photon cross section compared to NLO QCD predictions. Below 30 GeV the “Conversion probability”-based method is used, where above 30 GeV unconverted photons were measured.	19
3.1	An aerial view of the DESY-Hamburg research center. The HERA and PETRA Accelerators are shown as the two large dashed circles, while the four experiments are shown as the four small solid circles.	22
3.2	A schematic diagram of the accelerator at DESY-Hamburg used for HERA beam injection.	26
3.3	The integrated HERA 1 and HERA 2 luminosity for each year of HERA operation.	28
3.4	The total combined HERA integrated luminosity.	29
3.5	A 3D diagram of the ZEUS detector showing its major components.	32
3.6	A 2D $x-y$ cross sectional view of the ZEUS detector near the interaction region.	35
3.7	A 2D $y-z$ cross sectional view of the CAL. The angular boundaries of the different calorimeter sections are shown.	36
3.8	The 3D representation of the ZEUS coordinate system.	37
3.9	A diagram of a BCAL tower. The orientation of the Barrel Presampler, 4 electromagnetic cells, and 2 hadronic cells can be seen.	39
3.10	An example of a charged particle being detected by the signal wires of a drift chamber.	41

3.11	An $x - y$ view of the ZEUS CTD. The 9 concentric superlayer rings can be seen.	42
3.12	The timing of energy deposited into the calorimeter can be used to differentiate between different types of events. Figure A shows an ep interaction, Figure B shows a beam-gas interaction, and Figure C demonstrates a cosmic muon event.	44
3.13	A diagram of the ZEUS 3 level trigger system and the DAQ system. . .	45
4.1	An illustration of the stages of a MC simulation of a HEP event. . . .	48
4.2	Diagrams of initial state radiation (a) and final state radiation (b). The virtual photon (γ^*) that takes part in the DIS interaction is also shown.	50
4.3	One possible example of the Lund String Hadronization Model in action.	51
4.4	Diagrams of the Lund String Model (left) and the Cluster Model (right).	52
4.5	An illustration of the steps for processing ZEUS data and MC events.	53
5.1	An illustration of the parameters used in helix fitting of CTD data to find tracks.	59
5.2	An illustration of the clustering of energy deposits to form CAL islands.	61
5.3	An illustration of the formation of EFOs from CAL islands and tracks.	63
5.4	A diagram of the variables used in the KTCLUS Algorithm.	66
5.5	A typical prompt photon with an associated jet event in PHP	76
5.6	Distributions for the kinematic variables Y_{jb} , Z_{vertex} , and $P_{T,miss}$ from the PHP prompt photon with jets data sample (crosses) compared to PYTHIA 6.2 (histogram) after full event selection. The vertical lines mark the placement of cuts described in Section 5.8.2.	77

5.7	Distributions for the kinematic variables $E - P_z$, Z_{vertex} , E_{el} , and Number of Vertex Tracks from the inclusive DIS prompt photon data sample (crosses) compared to the predictions from ARIADNE 4.12 (histogram) after full event selection. The vertical lines mark the placement of cuts described in Section 5.8.4.	79
5.8	The Q^2 distribution for the inclusive DIS prompt photon data sample (crosses) compared to the predictions from ARIADNE 4.12 (histogram) after full event selection.	80
5.9	A typical prompt photon in DIS event.	81
6.1	The distance, Δr (radians), between a photon candidate and the closest track for the prompt photon in DIS MC. “ELEC5 when no KTCLUS” corresponds to the subset of “ELEC5” events where ELEC5 finds a photon and KTCLUS does not. “KTCLUS when no ELEC5” corresponds to the subset of “KTCLUS” events where KTCLUS finds a photon and ELEC5 does not.	87
6.2	The distance, Δr (radians), between a photon candidate and the closest track for the fully inclusive background MC. “ELEC5 when no KTCLUS” corresponds to the subset of “ELEC5” events where ELEC5 finds a photon and KTCLUS does not. “KTCLUS when no ELEC5” corresponds to the subset of “KTCLUS” events where KTCLUS finds a photon and ELEC5 does not.	88

6.3	Correction factors for KTCLUS and ELEC5 from 2004/2005 e^- running period calculated using the dead material map, non-uniformities and BPRE.	89
6.4	Correlation between the detector and hadron levels for E_T^γ when the photon is reconstructed using the ELEC5 photon finder.	90
6.5	Correlation between the detector and hadron levels for E_T^γ when the photon is reconstructed using the KTCLUS photon finder.	91
6.6	E_T^γ resolution before and after energy corrections.	92
6.7	E_T^γ resolution in several ranges of $E_{T,reconstructed}^\gamma$ before and after energy corrections when the photon is reconstructed using the ELEC5 photon finder.	93
6.8	E_T^γ resolution in several ranges of $E_{T,reconstructed}^\gamma$ before and after energy corrections when the photon is reconstructed using the KTCLUS photon finder.	94
6.9	E_T^γ resolution in several ranges of η^γ before and after energy corrections when the photon is reconstructed using the ELEC5 photon finder. . .	95
6.10	E_T^γ resolution in several ranges of η^γ before and after energy corrections when the photon is reconstructed using the KTCLUS photon finder. . .	96
6.11	Diagram of the BCAL showing the \hat{Z} and \hat{R} axes. The front of the EMC cells are 5 cm in the z direction	98
7.1	Diagram of the DVCS (a) and BH processes (b),(c).	100
7.2	Leading contribution to DVCS in the FFS model.	102

7.3	DVCS data (crosses) compared to DVCS MC (histogram) for E_T^γ , η^γ , Number of cells in γ , BPRE signal, f_{max} , and $\langle\delta z\rangle$ when the photon was found with ELEC5.	105
7.4	DVCS Data (crosses) compared to DVCS MC (histogram) for E_T^γ , η^γ , Number of cells in γ , BPRE signal, f_{max} , and $\langle\delta z\rangle$ when the photon was found with KTCLUS.	106
7.5	DVCS Data (crosses) compared to DVCS MC (histogram) for the com- parison of the two photon finders. The differences in the number of cells, E_T^γ , f_{max} , and $\langle\delta z\rangle$ between the two photon finders is shown. . .	107
7.6	DVCS Data (crosses) compared to DVCS MC (histogram) for E_T^γ , η^γ , Number of cells in γ , BPRE signal, f_{max} , and $\langle\delta z\rangle$ when the photon was found with ELEC5 with $\langle\delta z\rangle < 0.65$	108
7.7	DVCS Data (crosses) compared to DVCS MC (histogram) for E_T^γ , η^γ , Number of cells in γ , BPRE signal, f_{max} , and $\langle\delta z\rangle$ when the photon was found with KTCLUS with $\langle\delta z\rangle < 0.65$	109
7.8	DVCS Data (crosses) compared to DVCS MC (histogram) for f_{max} in different regions of E_T^γ when the photon was found with ELEC5 with $\langle\delta z\rangle < 0.65$	110
7.9	DVCS Data (crosses) compared to DVCS MC (histogram) for $\langle\delta z\rangle$ in different regions of E_T^γ when the photon was found with ELEC5 with $\langle\delta z\rangle < 0.65$	111

7.10	DVCS Data (crosses) compared to DVCS MC (histogram) for f_{max} in different regions of η^γ when the photon was found with ELEC5 with $\langle\delta z\rangle < 0.65$	112
7.11	DVCS Data (crosses) compared to DVCS MC (histogram) for $\langle\delta z\rangle$ in different regions of η^γ when the photon was found with ELEC5 with $\langle\delta z\rangle < 0.65$	113
7.12	DVCS Data (crosses) compared to DVCS MC (histogram) for f_{max} in different regions of E_T^γ when the photon was found with KTCLUS with $\langle\delta z\rangle < 0.65$	114
7.13	DVCS Data (crosses) compared to DVCS MC (histogram) for $\langle\delta z\rangle$ in different regions of E_T^γ when the photon was found with KTCLUS with $\langle\delta z\rangle < 0.65$	115
7.14	DVCS Data (crosses) compared to DVCS MC (histogram) for f_{max} in different regions of η^γ when the photon was found with KTCLUS with $\langle\delta z\rangle < 0.65$	116
7.15	DVCS Data (crosses) compared to DVCS MC (histogram) for $\langle\delta z\rangle$ in different regions of η^γ when the photon was found with KTCLUS with $\langle\delta z\rangle < 0.65$	117
8.1	The 1999-2000 ZEUS DVCS data (points) compared to ZEUS DVCS MC (histogram).	121
8.2	Comparison between 1999-2000 ZEUS prompt photon with jet in photoproduction data and PYTHIA for the BPRE signal of the prompt photon candidate, in minimum ionizing particle units.	123

- 8.3 Comparison between 1999-2000 ZEUS prompt photon with jet in photoproduction data and combined prompt photon with jet + inclusive dijet MC sample for the E_T in the event not from the photon or the jet and distance between the photon and any track in the event. 124
- 8.4 Comparison between 1999-2000 ZEUS prompt photon with jet in photoproduction data and combined prompt photon with jet + inclusive dijet MC sample for the fraction of the photon's and jet's energy in the EMC section of the CAL. 125
- 8.5 Comparison between 1999-2000 ZEUS prompt photon with jet in photoproduction data and combined prompt photon with jet + inclusive dijet MC sample for E_T^γ , η^γ , E_T^{jet} , and η^{jet} . The contribution to the combined prompt photon with jet + inclusive dijet MC by the prompt photon with jet MC and inclusive dijet MC are also shown separately. 127
- 8.6 Comparison between 1999-2000 ZEUS prompt photon with jet in photoproduction data and combined prompt photon with jet + inclusive dijet PYTHIA for X_γ . The contribution to the combined prompt photon with jet + inclusive dijet MC by the prompt photon with jet MC and inclusive dijet MC are also shown separately. 128
- 8.7 The correction factors for the E_T^γ , η^γ , E_T^{jet} , η^{jet} , and x_γ distributions. . 135

- 8.8 The γ +jet differential cross sections as functions of E_T^γ and η^γ . The 1999-2000 data from this thesis (solid black crosses) are compared to the published ZEUS 1999-2000 data (red dashed crosses), the PYTHIA 6.3 predictions (solid histogram), and the HERWIG 6.5 predictions (dashed histogram). 136
- 8.9 The γ +jet differential cross sections as functions of E_T^γ and η^γ . The published ZEUS 1999-2000 data (points) are compared to the theoretical QCD calculations and predictions of Monte Carlo models. The bands for the KZ and LZ predictions correspond to the uncertainty in the renormalisation scale which was changed by a factor of 0.5 and 2. . 137
- 8.10 The γ +jet differential cross sections as functions of E_T^{jet} and η^{jet} . The 1999-2000 data from this thesis (solid black crosses) are compared to the published ZEUS 1999-2000 data (red dashed crosses), the PYTHIA 6.3 predictions (solid histogram), and the HERWIG 6.5 predictions (dashed histogram). 138
- 8.11 The γ +jet differential cross sections as functions of E_T^{jet} and η^{jet} . The published ZEUS 1999-2000 data (points) are compared to the theoretical QCD calculations and predictions of Monte Carlo models. The bands for the KZ and LZ predictions correspond to the uncertainty in the renormalisation scale which was changed by a factor of 0.5 and 2. . 139

- 8.12 The γ +jet differential cross sections as function of X_γ . The 1999-2000 data from this thesis (solid black crosses) are compared to the published ZEUS 1999-2000 data (red dashed crosses), the PYTHIA 6.3 predictions (solid histogram), and the HERWIG 6.5 predictions (dashed histogram). 140
- 8.13 The γ +jet differential cross sections as functions of X_γ . The published ZEUS 1999-2000 data (points) are compared to the theoretical QCD calculations and predictions of Monte Carlo models. The bands for the KZ and LZ predictions correspond to the uncertainty in the renormalisation scale which was changed by a factor of 0.5 and 2. 141
- 8.14 The inclusive prompt photon cross section in photoproduction (a,b) measured by H1 at $\sqrt{s} = 319$ GeV as functions of E_T^γ and η^γ , and with the additional requirement of a jet with $E_T^{jet} > 4.5$ GeV and $-1 < \eta^\gamma < 2.3$ (c,d). 142
- 8.15 The prompt photon cross section in photoproduction measured by H1 with the requirement of a jet with $E_T^{jet} > 4.5$ GeV and $-1 < \eta^\gamma < 2.3$ as a function of E_T^{jet} and η^{jet} (a,b). The cross section as a function of the fraction of the proton's momentum involved in the collision, X_p , and the fraction of the exchange photon's momentum involved in the collision, X_γ , are also shown (c,d). 143

- 9.1 Comparison between ZEUS prompt photon data and PYTHIA MC predictions for prompt photons in DIS with and without ARIADNE background simulation. The solid line represents the result of the best fit to the data using a mixture of the prompt photon and inclusive DIS MCs. The prompt photons were identified using the ELEC5 photon finder with $\Delta r > 0.2$ 149
- 9.2 Comparison between ZEUS prompt photon data and PYTHIA MC predictions for prompt photons in DIS with and without ARIADNE background simulation. The solid line represents the result of the best fit to the data using a mixture of the prompt photon and inclusive DIS MCs. The prompt photons were identified using the KTCLUS photon finder with $\Delta r > 0.2$ 150
- 9.3 Comparison between ZEUS prompt photon data and the predictions from prompt photon in DIS PYTHIA MC and inclusive ARIADNE MC for the distance in (η, ϕ) from the prompt photon candidate to the closest track. The photons were identified with ELEC5 (Left) and KTCLUS (Right) independently. The MC predictions are normalized to the data for $\Delta r > 1.1$ 151

Chapter 1

Introduction

Since the dawn of mankind, man has had the seemingly juvenile urge to pick up two rocks and smash them together. Would it spark? Would it break apart? Those are the types of things we wanted to figure out. Even after a millennia of refinements, from the formulation of the basis of modern atomic theory by Boscovich in 1758 to the arrangement of the elements onto the periodic table by Mendeleev in 1869, we still have the urge to bang things together and see what we get out. In modern day high-energy physics the process has been refined to the point that we smash sub-atomic particles into each other at speeds approaching the speed of light and requiring detectors the size of houses to *see* the byproducts fly out of the collision.

Modern day particle physics¹ begins in 1898 when Joseph Thompson discovered the electron. This confirmed the theories that the atoms so elegantly organized on the periodic table by Mendeleev were themselves comprised of smaller constituents. This gave rise to the “Plum pudding” model of the atom, where negatively charged electrons were like plums in the positively charged pudding of the atom. In 1909 Rutherford’s scattering experiments demonstrated that atoms contain a small positively charged

¹I use the terms “Particle physics” and “High-energy physics” interchangeably.

nucleus at their center. This led to the formulation of the Bohr model of the atom in 1913. This was soon followed by the discovery of the proton in 1919 by Rutherford. The list of the major constituents, nucleons, of atomic nuclei was rounded off in 1931 by James Chadwick's discovery of the neutron.

As always with the capriciousness of the natural world that is not the end of the story. There were still some unexplained questions. How were the nucleons held together? Why would nuclei sometimes decay? So the search continued. Soon muons were discovered. They had the same properties as electrons but were 200 times heavier. Also, an abundance of other new particles were discovered. They were briefly stable and interacted via the strong nuclear force, later labeled as hadrons. Indications began to emerge that nucleons themselves were comprised of smaller charged objects. In 1964 Gell-Mann and Zweig formulated that hadrons, including the proton and neutron, were comprised of combinations of quarks that were "glued" together with gluons. The first direct experimental evidence of gluons was found in 1979 at the PETRA electron-positron collider at DESY in Hamburg. Together with the electroweak theory [1] they form the Standard Model that is used in particle physics to this day.

1.1 The Standard Model

The standard model is currently the most complete model that explains particles and their interactions. In the standard model there are three types of elementary particles: leptons, quarks, and bosons. The bosons are responsible for mediating the interactions between particles. Each particle also has an anti-particle with opposite charge.

Quarks	u <i>up</i>	c <i>charm</i>	t <i>top</i>
	d <i>down</i>	s <i>strange</i>	b <i>bottom</i>
Leptons	ν_e <i>e neutrino</i>	ν_μ μ <i>neutrino</i>	ν_τ τ <i>neutrino</i>
	e <i>electron</i>	μ <i>muon</i>	τ <i>tau</i>
I			II
The Generations of Matter			

Table 1.1: The quarks and leptons organized into their generations in order of increasing mass.

1.1.1 Leptons and Quarks

Leptons are spin- $\frac{1}{2}$ particles that do not interact with the strong force. There are three generations of leptons: electron (e), muon (μ) and tau (τ). Each generation consists of a particle with a negative charge of one unit and a corresponding neutrino with no charge. Neutrinos have very little mass and interact via the weak force.

Quarks are spin- $\frac{1}{2}$ particles that have a fractional electric charge and also have a color charge of either red, green, or blue. The color charge is associated with the strong force. There are six types of quarks that are divided into three generations. Each generation consists of two quarks, one with a charge of $\frac{2}{3}$ and one with a charge of $\frac{-1}{3}$. Quarks are not observed as free particles due to color confinement (see section 1.3 for more details). Quarks combine to form colorless hadrons. Baryons are hadrons with three quarks, each with a different color charge (red, green, blue or anti-red, anti-green, anti-blue), *e.g.* protons and neutrons. Mesons (pions, etas *etc*) are hadrons with two quarks: one quark and its anti-quark. The quarks in a meson have opposite color

charge (*e.g.* one red and one anti-red quark or if one is blue then other is anti-blue).

The three generations of quarks and leptons are given in Table 1.1.

1.1.2 Bosons

In addition to quarks and leptons the Standard Model also has bosons which mediate particle interactions. Bosons are spin-1 particles responsible for the attraction, repulsion, annihilation and decay of particles. Not all particles can interact with or create every boson. Only particles affected by a particular force can interact with the boson that mediates that force. In nature there are four fundamental forces: electromagnetic, weak, strong, and gravity. With the exception of gravity all of the mediating bosons have been observed. Therefore gravity and its theoretical boson, the graviton, are not included in the Standard Model. Table 1.2 lists the bosons in the Standard Model and the forces that they mediate.

Boson	Mass (GeV)	Charge	Force
γ (photon)	0	0	Electromagnetic
W^\pm	80.4	± 1	Weak
Z^0	91.187	0	Weak
g (gluon)	0	0	Strong

Table 1.2: The bosons and their properties in the Standard Model.

1.2 Quantum Electrodynamics

Quantum Electrodynamics (QED) is Abelian gauge theory that describes the electromagnetic interaction. QED is described by the $U(1)$ group. Where the U signifies that the group is unitary, *i.e.* for a generator matrix M , $M^\dagger M = 1$. The 1 signifies that the matrix is 1 dimensional.

The weak force is described by the $SU(2)$ group. Where “S” stands for special, in that its determinant is 1. The $SU(2)$ group requires three generators which give rise to one neutral, Z^0 , and two charged, W^\pm , weak bosons. The combination of the $U(1)$ and $SU(2)$ groups, $SU(2)\times U(1)$, describes the combined electroweak theory.

1.3 Quantum Chromodynamics

Quantum Chromodynamics (QCD) is the non-Abelian $SU(3)$ gauge theory that describes the strong interaction. The $SU(3)$ group requires 8 generators, which correspond to the 8 possible color combinations for gluons. The non-Abelian nature of QCD means that gluons can interact with other gluons. Unlike the other forces in the standard model, the potential that describes the strong force exhibits an approximately linear dependence on the distance between the interacting particles. This gives rise to two of the most important properties of QCD: confinement and asymptotic freedom.

Confinement: Single quarks and single gluons have never been observed experimentally. In QCD particles must be unchanged under rotation in color space. In other words, observed particles must be colorless.

Asymptotic freedom: The potential that describes the strong force exhibits an approximately linear dependence on the distance between the interacting particles. As quarks move apart the strength of the color force between them increases. Conversely, if they are very close together they behave almost like free particles.

1.3.1 Perturbative Quantum Chromodynamics

Perturbative Quantum Chromodynamics, pQCD, provides the mathematical description of QCD by starting with an approximation of the interaction and adding suc-

cessively smaller corrections onto that approximation. As more and more corrections are included the pQCD calculation describes the interaction better and better.

pQCD corrections are typically done as powers of the strong coupling constant, α_s . The strong coupling constant characterizes the strength of the strong force. A full QCD calculation may contain many different orders of the strong coupling constant: α_s , α_s^2 , α_s^3 , etc. A leading order (LO) calculation only includes the lowest order Feynman diagrams possible for an interaction. A Next-to-Leading Order (NLO) calculation includes the terms with the next power of the coupling constant. Illustrations of generic Feynman diagrams to different orders of the strong coupling constant α_s are shown in Figure 1.1.

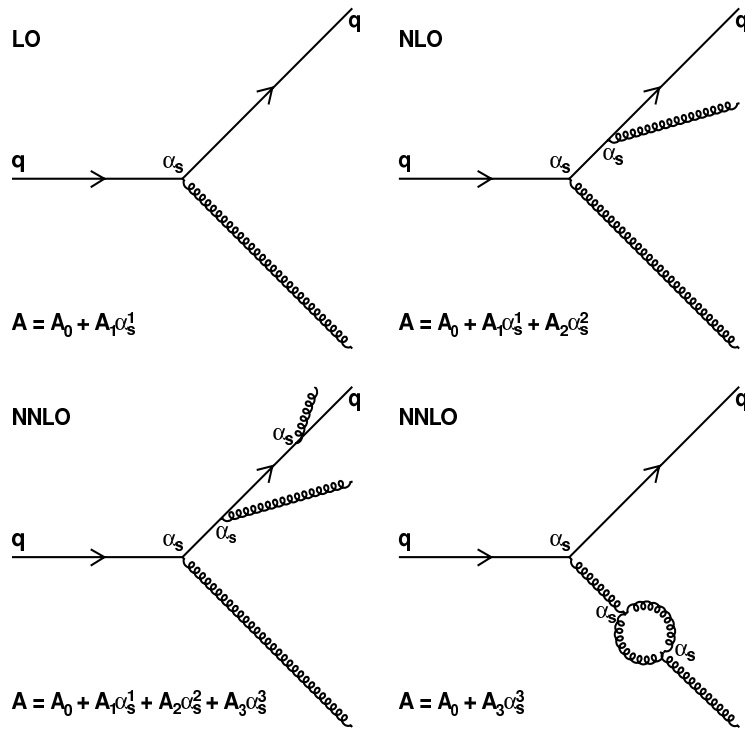


Figure 1.1: Generic diagrams of LO, NLO, and NNLO pQCD calculations.

1.4 Lepton Nucleon Scattering

Much of the testing of QCD and QED predictions is done via scattering experiments, where a beam of high energy particles bombards a target. In the case of ZEUS a lepton beam is scattered off a proton beam. This process is illustrated in Figure 1.2. When an electron and proton interact they do so by exchanging a boson. The leptonic nature of electrons prohibits the exchange boson from being a gluon. There are two types of bosons that can mediate the interaction in lepton-nucleon scattering. The first type involves the exchange of a photon or a Z^0 boson. Since neither of these carry electric charge the process is referred to as **neutral current**. The second type of scattering is mediated by the exchange of a W^\pm boson, which does carry an electric charge and is thus referred to as **charged current**.

In lepton-proton scattering a lepton with momentum vector k is scattered off a proton with momentum p to a final momentum of k' . The center-of-mass energy of the system is denoted as \sqrt{s} and is given by

$$s^2 = (p + k)^2 \quad (1.1)$$

When $p \gg m_p$ and $k \gg m_e$, the proton mass and the lepton mass are taken to be zero, and Equation 1.1 simplifies to $s = 2p \cdot k$. The 4-momentum of the exchange boson is given by $q = k - k'$. The virtuality, Q^2 , of the exchange boson is defined as the negative square of the transferred momentum.

$$Q^2 = -q^2 = -(k - k')^2 \quad (1.2)$$

When the lepton scatters off the proton it only interacts with a parton within the

proton. To leading order the fraction of the proton momentum carried by the struck parton is described by the scaling variable, x_{Bj} , introduced by Bjorken in 1969 [4] which is given by

$$x_{Bj} = \frac{Q^2}{2p \cdot q} \quad (1.3)$$

Bjorken also introduced the inelasticity, y , of the interaction, which is a measure of the lepton momentum transferred to the proton:

$$y = \frac{p \cdot q}{p \cdot k} \quad (1.4)$$

Combining definitions of the kinematic variables gives

$$Q^2 = sx_{Bj}y \quad (1.5)$$

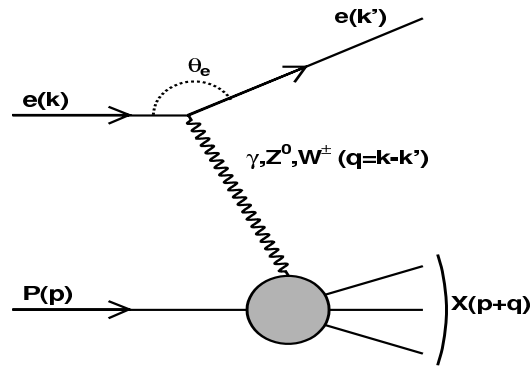


Figure 1.2: A general diagram of an interaction between a lepton with momentum k and a hadron with momentum p mediated by an exchange boson with momentum $q = k - k'$.

1.4.1 Photoproduction

In the case where Q^2 is low, *i.e.* $Q^2 < 1 \text{ GeV}^2$, the interaction is predominantly electromagnetic. This is known as photoproduction (PHP). In the case of photoproduction the exchange photon is nearly real. In photoproduction the proton is not broken apart and will escape detection. “Hard” interactions are scatterings in which high- P_T particles are produced. If the energy scale of the hard interaction is much higher than the QCD energy scale, $\Lambda_{QCD} \approx 200 \text{ MeV}$, then the strong coupling constant is sufficiently small for pQCD to be applied. In photoproduction $Q^2 \approx 0$ and does not set the scale of the interaction. In prompt-photon photoproduction the energy of the prompt photon emerging from the interaction provides the scale. At leading order the nearly real exchange photon provides two types of interactions: direct photoproduction and resolved photoproduction. Examples of each are shown in Figure 1.3.

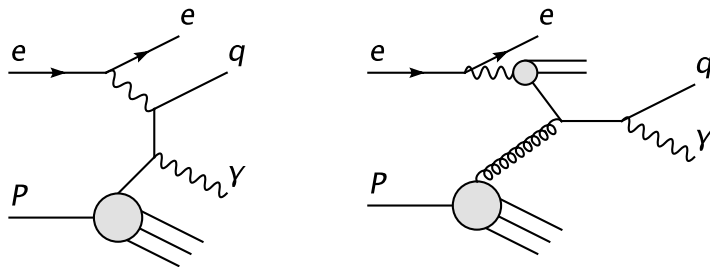


Figure 1.3: The leading order diagrams for direct photoproduction (left) and resolved photoproduction (right).

In direct photoproduction, the entire photon interacts in the hard scatter. Since photons can only interact with charged objects the hard scatter is restricted to events involving the quarks within the proton. In resolved photoproduction, the photon

briefly fluctuates into a hadronic state. While in the hadronic state the resolved photon can provide a quark or gluon to interact with the proton. This provides sensitivity to the gluon content of the proton for the resolved process. We can define the variable x_γ to describe the fraction of the exchange photon's momentum that is involved in the hard scatter. So for the direct subprocess, $x_\gamma \approx 1$. For the resolved process, $x_\gamma \lesssim 1$.

Photoproduction events are the most common event in HERA physics. The cross section for events with high virtuality is suppressed by a factor of $(\frac{1}{Q^4})$.

1.4.2 Deep Inelastic Scattering

As Q^2 increases the exchange boson moves off the mass shell and becomes more virtual. The increasing momentum carried by the highly virtual exchange photon increases the chance that the proton will break apart in the interaction. In photoproduction the hard scale was characterized by the outgoing particles. In deep inelastic scattering the virtuality of the exchange boson provides the scale that is used to characterize the interaction.

1.4.3 Cross Section and Structure Functions

In a scattering experiment the differential cross section $d\sigma$ is the probability of observing a scattered particle in a given state per unit of solid angle

$$\frac{d\sigma}{d\Omega} = \frac{\text{Scattered flux/Unit of solid angle}}{\text{Incident flux/Unit of surface}} \quad (1.6)$$

which can be integrated over the solid angle to obtain the total cross section σ . For a generic interaction, with a transition rate per unit volume of W_{fi} , the cross section

can also be expressed as

$$\sigma = \frac{W_{fi}}{\text{Initial flux}} (\text{Number of final states}) \quad (1.7)$$

At this point it is useful to define parton density functions (PDFs) that describe the probability of finding a parton at a certain Q^2 within a given range of momentum fractions of the proton, $[x, x + dx]$ within the proton. PDFs cannot be calculated from first principles, and must therefore be extracted from fits to structure function measurements. The proton structure functions expressed in terms of the PDFs and parton charge e_i are as follows:

$$F_1(x, Q^2) = \sum_i \frac{1}{2} e_i^2 f_i(x, Q^2) \quad (1.8)$$

$$F_2(x, Q^2) = \sum_i e_i^2 x f_i(x, Q^2) \quad (1.9)$$

$$F_L(x, Q^2) = F_2 - 2xF_1 \quad (1.10)$$

DIS Cross Section The DIS cross section as a function of x and Q^2 expressed in terms of these structure functions and an additional structure function F_3 is given by,

$$\frac{d^2\sigma(e^\pm p)}{dx dQ^2} = \frac{4\pi\alpha_{EM}^2}{xQ^4} [Y_+ F_2(x, Q^2) - y^2 F_L(x, Q^2) \mp Y_- x F_3(x, Q^2)] \quad (1.11)$$

where $Y_\pm = 1 \pm (1 - y)^2$. The structure function F_2 is the contribution to the cross section from the transversely polarized virtual bosons, while F_L is the contribution from longitudinally polarized bosons. F_3 comes from the parity violation from Z^0 boson exchange and only becomes important at $Q^2 \approx M_Z^2$. For this analysis Q^2 is typically $\ll M_Z^2$ so the contribution from F_3 is negligible.

PHP Cross Section When $Q^2 \approx 0$ the exchange photon is quasi-real and the lepton-nucleon scattering can be thought of as photon-proton scattering. The total ep cross section can be divided into contributions from the total γp cross section, $\sigma_{TOT}^{\gamma p}$, and the photon flux, $f_{\gamma/e}$. Similarly to the case for DIS, the cross section for photoproduction may be written as

$$\frac{d^2\sigma(e^\pm p)}{dydQ^2} = f_{\gamma/e}(y, Q^2)\sigma_{TOT}^{\gamma p}(y, Q^2) \quad (1.12)$$

where

$$f_{\gamma/e}(y, Q^2) = \frac{\alpha}{2\pi Q^4} \left[\frac{Y_+}{y} - 2 \frac{1-y}{y} \frac{Q_{min}^2}{Q^2} \right] \quad (1.13)$$

and Q_{min}^2 is the kinematic lower bound and is given by $Q_{min}^2 = m_e^2 y^2 / (1-y)$.

1.4.4 Prompt Photons

Experimentally prompt photons are high- P_T photons that are produced at the hard scatter. Here, P_T or transverse momentum is the component of the particle's momentum in a plane perpendicular to the beam direction. Prompt photons are particularly useful because they do not undergo hadronization, in contrast to quarks or gluons which must form jets due to the principle of confinement (Chapter 1.3). The kinematics of prompt-photon physics are also sensitive to parton dynamics within the proton, examples of which can be seen in Chapter 2. The presence of a jet in the final state in addition to the prompt photon allows the underlying physics process to be more clearly identified.

1.4.5 Prompt Photons in ep Scattering at ZEUS

The aim of this study is to employ new experimental techniques for the identification and measurement of prompt photons with the ZEUS detector to determine the cross section for $ep \rightarrow e + \gamma_{prompt} + jet + X$ scattering in PHP. Once measured the cross section can be directly compared to several NLO QCD predictions thereby providing constraints for the proton and photon PDFs as well as evaluating the effectiveness of the differing methods used in the NLO calculations. The new experimental techniques for prompt photon identification can also be used to measure the cross section for $ep \rightarrow e + \gamma_{prompt} + X$ production in DIS.

Chapter 2

Experimental Studies of Prompt Photons

The kinematics of prompt photon physics is sensitive to parton dynamics within the proton. An example is the intrinsic momentum of the partons of the proton, $\langle k_T \rangle$, involved in hard scattering. Measurements of $\langle k_T \rangle$ have been made by several collaborations including ZEUS [7]. Figure 2.1 shows the ZEUS result compared to several other experimental results. The WA70, UA1 and CDF experiments at CERN and Fermilab are able to probe high center-of-mass energies, while many fixed target experiments are able to probe the lower center-of-mass energies. The ZEUS result bridges the gap between fixed-target experiments and the other collider experiments. The ZEUS result (filled circles) compares favorably with trend seen by other experimental measurements, that $\langle k_T \rangle$ increases with increasing W .

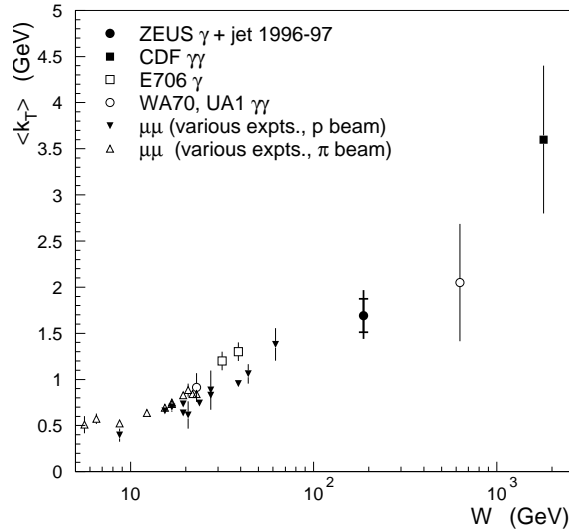


Figure 2.1: The intrinsic momentum of partons within the proton versus the γp center-of-mass energy for several different experiments.

2.1 Prompt photons at the Tevatron

Prompt photons¹ have been studied by both the D0 and CDF collaborations at Fermilab near Chicago. The Tevatron provides $p\bar{p}$ collisions at energies of $\sqrt{s} = 1.96$ TeV, $\sqrt{s} = 1.8$ TeV, and $\sqrt{s} = 630$ GeV. The methodologies of finding photons at CDF and D0 is similar to that used at ZEUS taking into account the differences in detectors and the higher center of mass energy available at the Tevatron.

2.1.1 D0

The D0 collaboration has measured [2] the inclusive cross section for prompt photon production at the center of mass energy of $\sqrt{s} = 1.96$ TeV. The photons

¹At the Tevatron prompt photons are generally referred to as ‘direct’ photons. Referring to the fact that they come directly from the hard scatter. However due to the ‘direct’ photoproduction process the term ‘prompt’ photon will be used throughout this thesis.

measured have a pseudorapidity of $|\eta^\gamma| < 0.9$ and transverse momenta spanning $23 < p_T^\gamma < 300$ GeV. The photon purity, defined as the ratio of the signal to signal plus background, was also measured. The dependence of the photon purity on P_T^γ at D0 is shown in Figure 2.2. A clear decrease in purity can be seen with decreasing P_T^γ . The kinematic region with low- P_T^γ , where the decreasing photon purity prevents further measurement, is the region where the ZEUS detector is able to probe. Figure 2.3 shows the D0 measurement of the P_T^γ dependence on the prompt photon cross section at $\sqrt{s} = 1.96$ TeV. The cross sections as a function of P_T^γ were compared with several next-to-leading order pQCD calculations from JETPHOX [12]. The theoretical calculations from JETPHOX agree within uncertainties with the measured cross section, providing some confidence that the current analysis will be well modeled by NLO pQCD predictions.

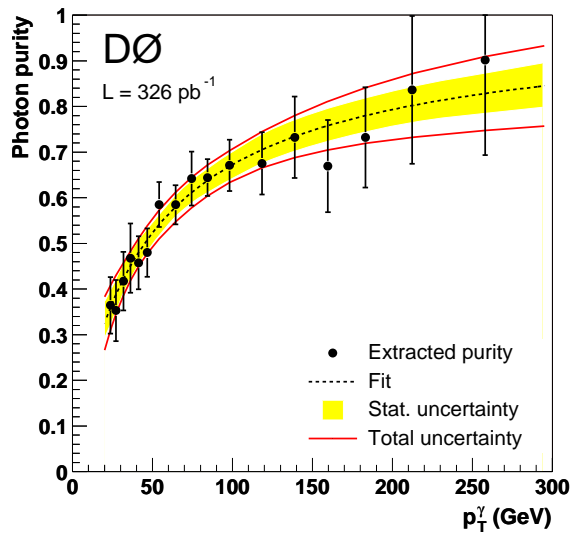


Figure 2.2: Dependence of photon purity on P_T^γ for center of mass energy of $\sqrt{s} = 1.96$ TeV at D0.

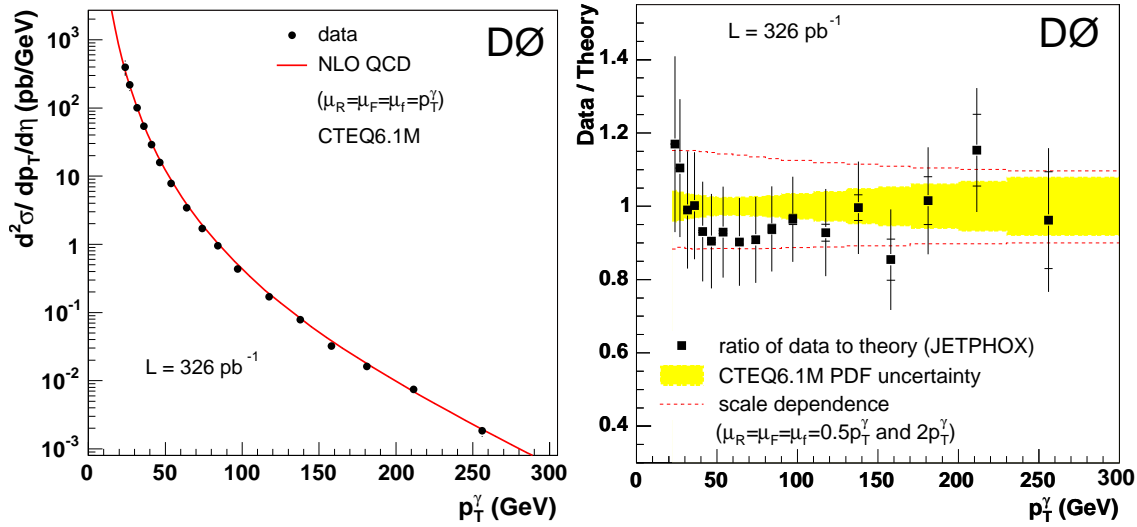


Figure 2.3: D0 measurement at the center of mass energy, $\sqrt{s} = 1.96$ TeV of the P_T^γ dependence of the isolated photon cross section (Left) and the ratio of the measured cross section to the NLO pQCD calculation from JETPHOX (Right).

2.1.2 CDF

The CDF Collaboration has also made a measurement of the prompt photon cross section at $\sqrt{s} = 1.8$ TeV. The CDF detector provided a measurement of photons with $30 < P_T^\gamma < 65$ GeV and $|\eta^\gamma| < 0.9$. The prompt photon cross section measurement from CDF can be seen in Figure 2.4. The data are compared to the NLO QCD predictions [3]. A measurement of prompt photons that converted into e^+e^- pairs before detection, referred to as the ‘‘Conversion probability’’-based method, are also shown in Figure 2.4. For the ‘‘Conversion probability’’-based method for background discrimination the P_T^γ range is extended to $10 < P_T^\gamma < 65$ GeV.

Recent improvements in theoretical calculations improve agreement between data and theory for both D0 and CDF, but there remain discrepancies between data and theory at low- P_T^γ . The low- P_T^γ region is where the high-order QCD radiation

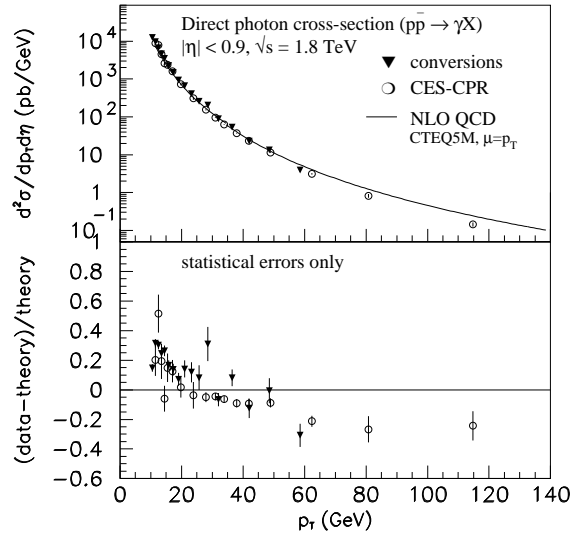


Figure 2.4: The CDF measurement at the center of mass energy of $\sqrt{s} = 1.8$ TeV of the P_T dependence of the isolated prompt photon cross section compared to NLO QCD predictions. Below 30 GeV the “Conversion probability”-based method is used, where above 30 GeV unconverted photons were measured.

terms are expected to contribute the most. Both the D0 and CDF photon samples also have a lower purity at low- P_T^γ compared to the high- P_T^γ samples. The kinematics attainable at ZEUS provide a valuable ability to further study low- P_T^γ regions, where the hard scatter is not well described by lower order perturbative QCD calculations.

2.2 Large Hadron Collider

The knowledge and expertise gained in the study of energetic photons in the final state is expected to play an important role at the Large Hadron Collider (LHC). The ability of prompt photons to study low- x physics and provide constraints on the gluon PDFs will be beneficial to LHC physics. In addition to providing constraints to PDFs the study of prompt photons at ZEUS provides information about hard scattering

processes that involve energetic photons in the final state. Prompt photon processes will form a significant background in the search for the multi-photon decay state of Higgs particles, *i.e.* the $H \rightarrow \gamma\gamma$ decay path. The identification and study of photons in high energy physics will continue for some time to come.

Chapter 3

Experimental Setup

The testing of any theoretical calculation requires experimental measurements made with an experimental apparatus. The measurement depends on the properties of the particles being investigated and how they interact with experimental apparatus.

3.1 Deutsches Elektronen Synchrotronen

The Deutsches Elektronen Synchrotronen (DESY) research center is part of Germany's Helmholtz community. The Helmholtz community is Germany's largest research organization with an annual budget of 183 million Euros. DESY has two campuses: Hamburg (Germany) and Zeuthen (state of Brandenburg, Germany). Over 3000 scientists from 45 countries come to work and study at DESY's Hamburg laboratories each year. DESY has a diverse spectrum of research in the areas of particle physics and photon science. Current research and development activities include work on the European X-ray free-electron laser (XFEL), the FLASH free-electron laser and the International Linear Collider (ILC) through the development of TESLA [18] technology. DESY is also heavily involved in materials studies using photons from synchrotron radiation coordinated through the Hamburg Synchrotron Radiation Lab-

oratory (HASYLAB).

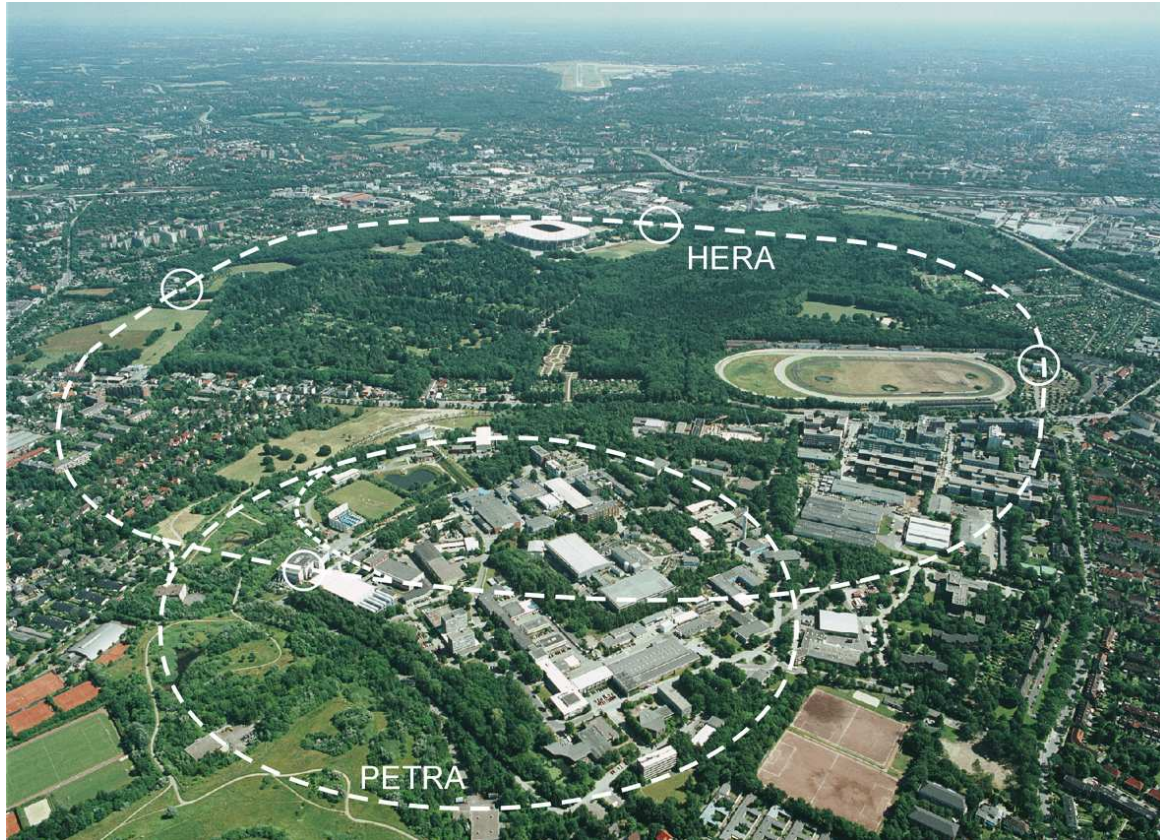


Figure 3.1: An aerial view of the DESY-Hamburg research center. The HERA and PETRA Accelerators are shown as the two large dashed circles, while the four experiments are shown as the four small solid circles.

3.2 HERA Accelerator

The DESY Hadron Elektron Ring Anlage (HERA) was the only lepton-nucleon beam collider, sometimes described as a “super electron microscope.” The HERA collider is 6.336 kilometers in circumference and is located between 10 and 25 meters below ground in the city of Hamburg. It has four 90° bends and four straight sections.

On two of the straight sections the beams cross and that is where the ZEUS and H1 detectors are located. Both H1 and ZEUS studied the interactions between the proton and electron beams. On the other two straight sections are the fixed target experiments, HERA-B and HERMES. The HERA-B experiment used the interaction between the proton beam halo and a fixed wire grid to study CP violation. The HERMES experiment used the interaction between the electron beam and a polarized gas target to study the spin structure of the proton.

For 15 years HERA provided physicists a window through which to observe the collisions of protons with electrons. In 1992 HERA began by colliding 820 GeV protons with 27.52 GeV electrons, with a center-of-mass energy of $\sqrt{s} \approx \sqrt{4E_e E_p} \approx 300$ GeV. In 1998 the proton energy was increased to 920 GeV, a center-of-mass energy of $\sqrt{s} \approx 320$ GeV. In 2007 the proton beam energy was once again changed, this time to 460 GeV and 575 GeV. This provided data at a center-of-mass energies of $\sqrt{s} \approx 225$ GeV and $\sqrt{s} \approx 252$ GeV respectively.

Over its lifetime HERA switched between using electrons and positrons for the 27.52 GeV lepton beam several times. Between 2000 and 2002, HERA underwent an upgrade in luminosity (number of particles per unit area per unit time). Before the upgrade (the "HERA I" running period) the peak luminosity was $\approx 2 \times 10^{31} \text{cm}^{-2} \text{s}^{-1}$. After the upgrade (the "HERA II" running period) the peak luminosity was $\approx 5.1 \times 10^{31} \text{cm}^{-2} \text{s}^{-1}$. In Figure 3.3 the total integrated luminosity delivered to the ZEUS experiment for each year of the HERA I and HERA II running periods is shown. In Figure 3.4 the total combined integrated luminosity delivered to ZEUS by HERA is shown, with a summary presented in Table 3.1.

Running Period	Year	$\approx \sqrt{s}$ (GeV)	Luminosity (pb^{-1})			
			HERA Delivered		ZEUS Physics	
			e^-p	e^+p	e^-p	e^+p
HERA I	1993	300	1.09		0.54	
	1994	300	1.08	5.11	0.28	3.02
	1995	300		12.31		6.62
	1996	300		17.16		10.77
	1997	300		36.35		27.85
	1998	300	8.08		4.60	
	1999	320	17.12	28.54	12.08	19.66
	2000	320		66.41		46.22
HERA II	2002	320		5.20		1.78
	2003	320		6.53		2.87
	2004	320		77.94		43.74
	2005	320	204.80		152.26	
	2006	320	86.10	118.36	61.23	99.54
	2007	320		62.18		46.35
	2007	225		15.69		13.18
	2007	252		9.36		7.77

Table 3.1: The integrated luminosity delivered by HERA to ZEUS and the gated (recorded for physics) luminosity recorded by ZEUS for each year of HERA operation.

3.2.1 Lepton Injection and Acceleration

Electrons for the lepton beam at HERA were obtained from a hot filament. Positrons for the lepton beam at HERA were obtained from e^+e^- pair production from bremsstrahlung radiation from electrons passing through a tungsten sheet. The leptons were then accelerated to 450 MeV in the 70 m LINAC II linear accelerator. Once at 450 MeV the leptons were collected in the PIA, a 29 m circular accumulator. The leptons were then injected into DESY II, where they were accelerated to an energy of 7 GeV. Once at 7 GeV the lepton beam was fed into the PETRA II accelerator where it was accelerated to 14 GeV. Once at 14 GeV the leptons were injected into HERA and accelerated to their final energy of 27.52 GeV. HERA used conventional dipole magnets with a magnetic field strength of 0.165 Tesla to hold the lepton beam in its orbit.

3.2.2 Proton Injection and Acceleration

The protons used by HERA were obtained from negatively charged Hydrogen (H^-) ions. The Hydrogen ions were accelerated in a linear accelerator (LINAC III) to 50 MeV. At the end of the LINAC III the electrons were stripped from the ions by a thin foil, before being fed into the DESY III accelerator. The 7.5 GeV protons were injected into the PETRA ring and accelerated to 39 GeV. The 39 GeV protons were then injected into HERA for their final acceleration to 920 GeV. As previously mentioned, the proton beam's final energy was changed several times during HERA's lifetime. HERA used superconducting dipole magnets with a magnetic field strength of 4.65 Tesla to hold the final 920 GeV proton beam in its orbit.

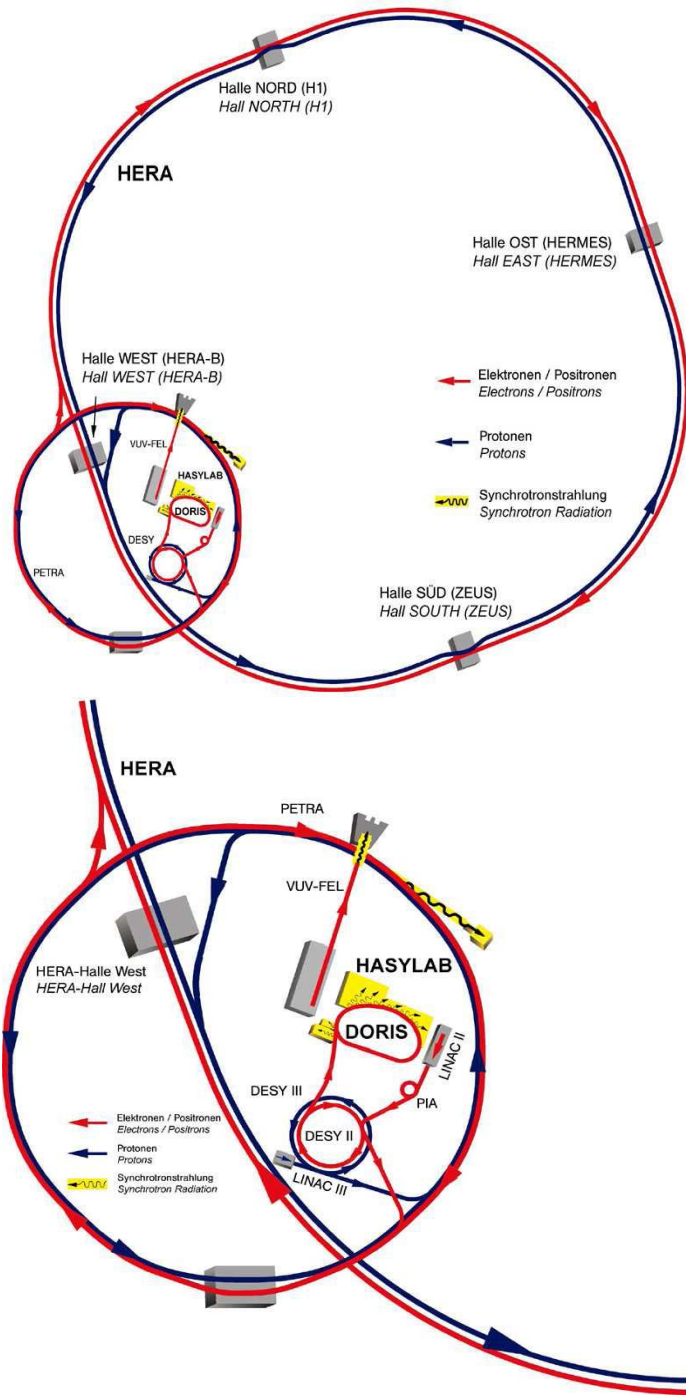


Figure 3.2: A schematic diagram of the accelerator at DESY-Hamburg used for HERA beam injection.

3.2.3 Beam Circulation and Collision

The lepton and proton beams were circulated in opposite directions in separate rings of magnets. The beams were brought together near the experimental interaction points. The beams were divided into bunches with a 96 ns spacing between the bunches. The HERA ring could hold 220 bunches each of leptons and protons. Not every possible bunch was filled during HERA injection. Approximately 15 consecutive possible bunches in both the lepton and proton beams were left empty. This allowed time for the "kicker" magnets responsible for the dumping of the beams to energize. In addition to un-filled bunches for dumping the beams, some bunches were left empty to allow for pilot bunches. Pilot bunches were filled lepton or proton bunches that had unfilled bunches in the other beam as they passed through the ZEUS or H1 interaction region. The pilot bunches allowed for studies of the interaction between the beams with the residual gas in the HERA (3×10^{-11} Torr) vacuum. Near the ZEUS or H1 interaction regions guiding magnets directed the proton beam into the lepton beam's path to cause the ep interactions.

3.3 Particle Interactions

To record the ep interactions provided by HERA for further study, an experimental apparatus is needed. As previously mentioned, there are two such apparatuses, ZEUS and H1, that were used. Careful consideration was made in their design as to how the byproducts of the ep collision interact with them. To better understand this it is useful to define some of the processes by which particles lose energy and interact with matter.

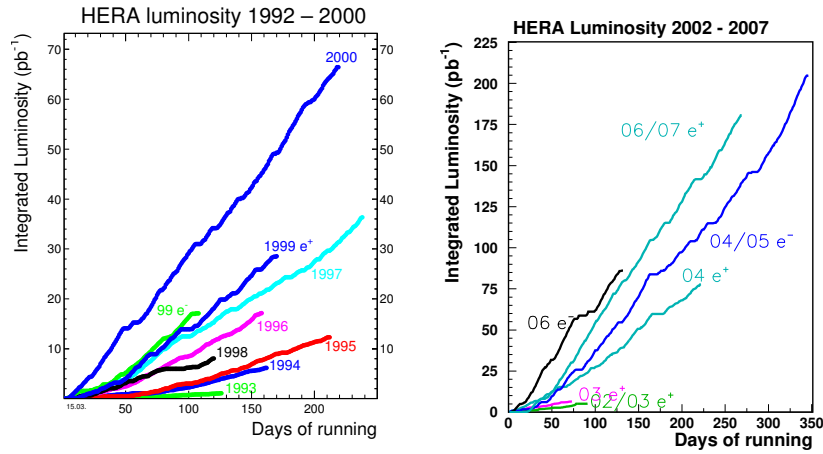


Figure 3.3: The integrated HERA 1 and HERA 2 luminosity for each year of HERA operation.

3.3.1 Definitions

Synchrotron Radiation is the emission of photons by charged particles as they change direction in a magnetic field oriented perpendicular to their path. The amount of energy the particles lose is proportional to $\frac{1}{m^4}$, where m is the rest mass of the particle. Synchrotron radiation is particularly pronounced for particles with lower masses, such as electrons.

Cherenkov Radiation is the light emitted by a charged particle traversing a medium faster than light would traverse the same medium. Nothing can travel faster than light, but in media light appears to move slower due to the frequent interactions between the photons and matter. The **index of refraction** is the ratio of the speed of light in a vacuum to the speed of light in a medium. As the energetic particle traverses the medium, it briefly polarizes the particles in the medium which emit photons as they return to their ground state.

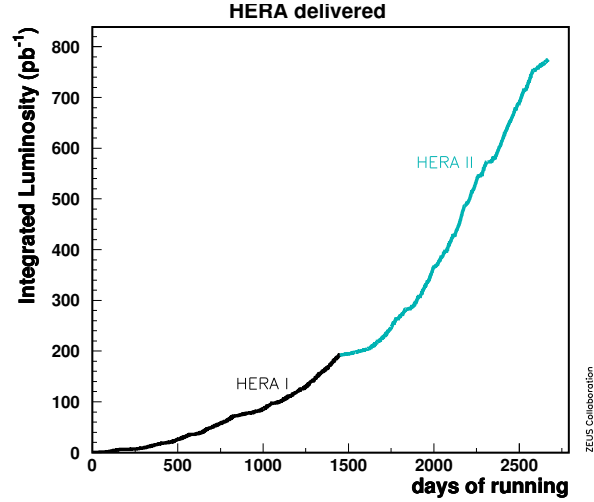


Figure 3.4: The total combined HERA integrated luminosity.

Bremsstrahlung Radiation, German for *braking radiation*, is the radiation emitted by a charged particle as it decelerates through material. The amount of energy the slowing particle loses is proportional to $\frac{1}{m^2}$, where m is the rest mass of the particle. As with synchrotron radiation, the amount of energy lost is more pronounced for particles with lower masses.

Ionization occurs when the atoms in the absorbing material become ionized by the traversing charged particle. Ionization is the dominant form of energy loss by low-energy electrons. The energy loss of electrons by ionization increases logarithmically with the electron's energy in contrast to the energy loss by bremsstrahlung radiation which rises nearly linearly. The electron energy at which the energy loss by ionization equals the loss by bremsstrahlung radiation is known as the **Critical Energy**, E_e (MeV). E_e is typically a few tens of MeV in most materials. For energies greater than E_e bremsstrahlung radiation dominates, below E_e ionization dominates.

Pair Production is the production of an e^+e^- pair by a photon in a nuclear or electron field. The probability for pair production in a nuclear field is higher than the probability for pair production in an electron field.

Radiation Length, X_0 ($\frac{g}{cm^2}$), is a property of the absorbing material that characterizes the amount of matter traversed by a photon or an electron as it deposits energy in the absorbing material. For a photon it is the mean free path for e^+e^- pair production. For a high-energy electron it is the average distance traveled before the electron loses all but $\frac{1}{e}$ of its energy through bremsstrahlung radiation.

Interaction Length, λ ($\frac{g}{cm^2}$), is a property of the absorbing material that characterizes the mean free path of a hadron before an inelastic collision. Similar to radiation length, but many times greater in magnitude, λ can be calculated from the atomic weight and density of the absorbing material. A general rule of thumb is $\lambda \approx 20X_0$.

3.3.2 Electromagnetic Showers

High energy electrons and photons lose energy in material primarily through bremsstrahlung radiation and pair production. When a photon pair-produces in the absorbing material it makes an energetic e^+e^- pair, which will subsequently undergo bremsstrahlung radiation. As an electron traverses the absorber it undergoes bremsstrahlung radiation, which produces an electron-photon pair. The electron-photon pair will subsequently undergo pair production and further bremsstrahlung radiation producing a shower of particles. The process of pair production and bremsstrahlung radiation repeats until the average energy per particle is low enough for ionization and Compton scattering to become the dominant form of energy transfer to the absorber.

Energy will continue to be deposited through ionization and Compton scattering until the shower is fully absorbed.

Molière Radius, R_M ($\frac{g}{cm^2}$), is a property of the absorbing material that characterizes the average lateral spread of electrons at critical energy after traversing one radiation length: $R_M = 0.0265X_0(Z + 1.2)$. Electromagnetic energy deposits with a total energy $\ll 1$ TeV on average deposit 90% of the energy within a cylinder with a radius equal to one Molière radius. The fraction of energy deposited increases to 99% for a cylinder with a radius equal to 3.5 Molière radii.

The depth into an absorber a particle has reached can be represented by t in units of X_0 . The **Shower Maximum**, t_{max} , is when there is the largest number of particles in the shower. After t_{max} the rate at which energy is deposited into the absorber decreases.

3.3.3 Hadronic Showers

Hadronic particles lose energy traversing an absorber via the strong force, predominately by inelastic collisions with atomic nuclei. For inelastic collisions, λ describes the longitudinal energy profile of the energy deposit. A frequent byproduct of these inelastic collisions are π^0 particles which decay into electromagnetic objects.

3.4 ZEUS Detector

The ZEUS collaboration was one of the two collaborations that made precision measurements of energetic ep interactions. The floor of the experiment hall was 30 m underground at the south experiment hall on the HERA ring. The ZEUS detector had a weight of 3600 tonnes and was 12 m \times 10 m \times 19 m. As can be seen in Figure 3.5,

the ZEUS detector [19] is a collection of many individual detector components, each with its own task. They combine to offer an aggregate view of ep interactions. To accurately study ep interactions, precise measurements of particle energies, directions, and properties must be made. The basic design of the ZEUS detector as you move outward from the interaction point is to first measure the momentum of charged particles in tracking detectors, then to measure the energies of the outgoing particles in a series of calorimeters. Some particles are expected to escape the ZEUS detector without losing all of their energy, typically muons. Therefore another tracking detector measures their tracks as they depart the ZEUS detector.

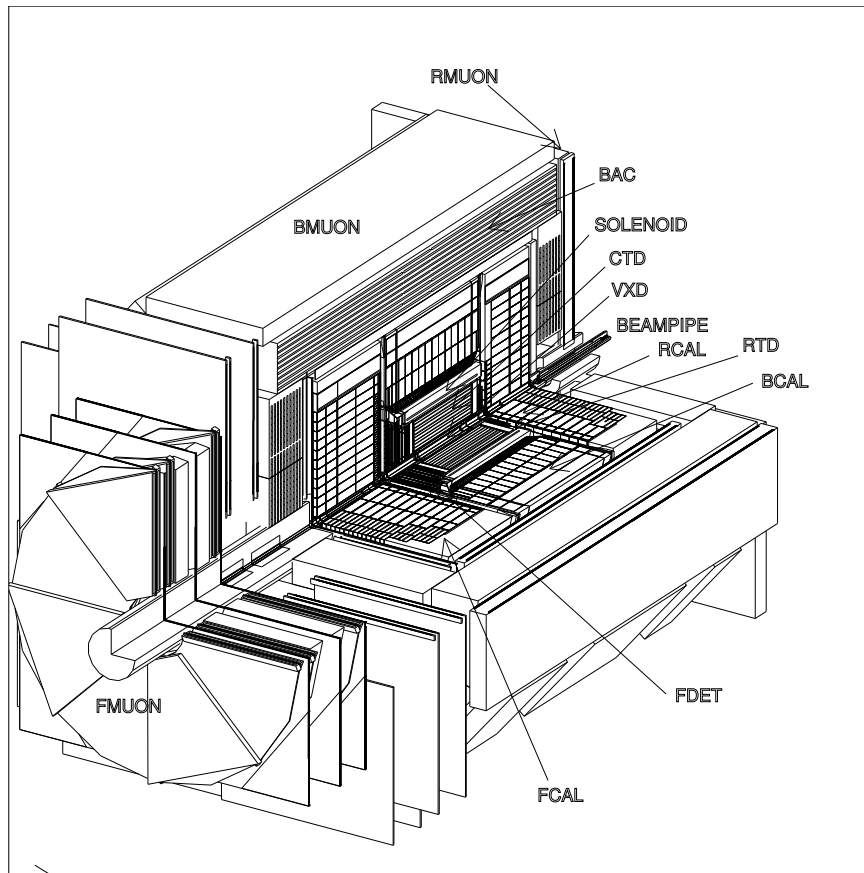


Figure 3.5: A 3D diagram of the ZEUS detector showing its major components.

A series of wire chambers and silicon detectors measured the tracks of charged particles. The innermost was the Micro Vertex Detector (MVD), installed in 2002 to replace the malfunctioning vertex detector (VXD) which was removed in 1995. Next were the central drift chamber (CTD), Forward (FTD) and Rear (RTD) drift chambers and a transition radiation detector (TRD). All of these detectors were encased in a thin superconducting solenoid coil (Solenoid) that provided a 1.43 Tesla magnetic field parallel to the beamline. The charged particle's momentum can be calculated from the curvature of its track.

A series of calorimeters measured the energy of the outgoing particles. The most central of which was the uranium scintillator calorimeter (CAL), which was divided into three sections (RCAL, BCAL, and FCAL). Particles that are not fully absorbed by the CAL passed into the backing calorimeter (BAC). The BAC was comprised of proportional tube chambers and the 7.3 cm thick iron plates of the return yoke. Particles, typically muons, that penetrate the BAC pass into limited streamer tube chambers (RMUON, BMUON and FMUON) that measure their positions. Their momenta could be determined because the iron yoke was magnetized at about 1.6 Tesla by copper coils and the return field of the Solenoid.

In addition to recording ep interactions, the ZEUS detector monitored the luminosity. By measuring the Bethe-Heitler process the ZEUS LUMI system was able to monitor the luminosity. The cross section of the Bethe-Heitler process, depicted in Figure 7.2, is well known and large which enabled a quick and reliable calculation of the luminosity. The main component of the LUMI system was a photon calorimeter located near the beamline at $z = -92.5$ m, that detected the photons emitted in the

Bethe-Heitler process. In addition to creating a photon the Bethe-Heitler process also lowered the energy of the lepton involved. This “Off momentum” lepton would not follow the same path out of the ZEUS detector as the other leptons in the beam. Several small calorimeters, $z = \{-6, -8, -35, -44\}m$, were used as *electron taggers* throughout the life of the ZEUS experiment to sample the position and energies of these off momentum leptons. The *6-meter tagger* took a lead role in the luminosity measurement during the low energy running periods of 2007.

The ZEUS detector also had to differentiate between an ep interaction and interactions of the beams with the residual gas in the beamline. Before the proton beam reached the ZEUS detector, it passed near an iron wall equipped with two layers of scintillation counts (VETOWALL). If a proton reacted with the residual gas in the beamline before reaching the main ZEUS detector it would produce a signal in the VETOWALL, and the event could be excluded.

More details about the ZEUS detector can be found elsewhere [19]. The components most important to this analysis are described in more detail below.

3.4.1 ZEUS Co-ordinate System

A right-handed coordinate system is used by the ZEUS collaboration. The $+z$ direction is defined by the motion of the proton beam. The $+x$ direction is towards the center of the HERA accelerator rings. The $+y$ direction is then upwards. The polar angle, $\theta \in [0, \pi]$, is defined as the angle from the $+z$ axis. The azimuthal angle, $\phi \in [0, 2\pi]$, is the angle from the $+x$ axis when projected onto the xy plane. The $+\phi$ direction is towards the $+y$ axis. This is illustrated in figure 3.8. The pseudorapidity of an object is given by,

Overview of the ZEUS Detector
(cross section)

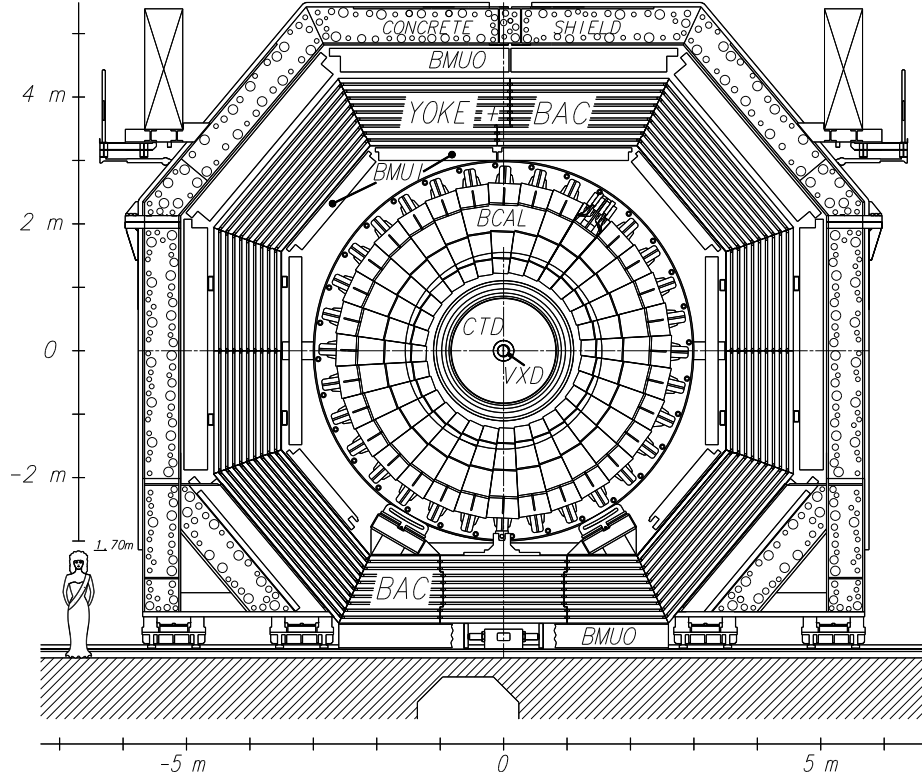


Figure 3.6: A 2D $x - y$ cross sectional view of the ZEUS detector near the interaction region.

$$\eta = -\log \tan \theta / 2 \quad (3.1)$$

3.4.2 Uranium Calorimeter

As previously mentioned the CAL was divided into three sections: the Rear (RCAL), the Barrel (BCAL), and the Forward (FCAL) Calorimeters. The RCAL, BCAL and FCAL cover angular ranges of $129.1^\circ - 176.2^\circ$, $36.7^\circ - 129.1^\circ$ and $2.6^\circ - 36.7^\circ$ respectively. Combined they formed a nearly hermetic coverage of the interaction region, covering over 99.8% of the solid angle.

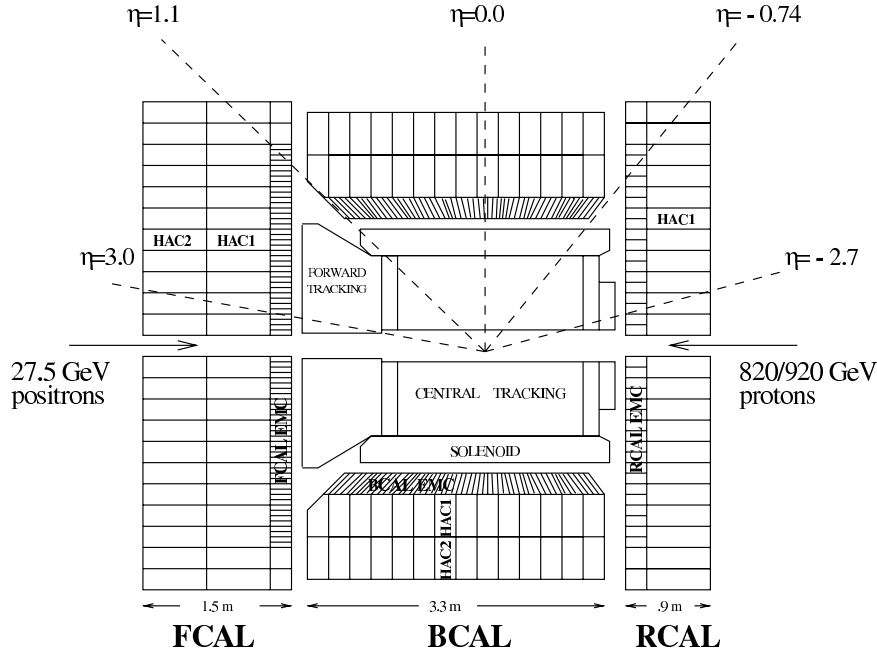


Figure 3.7: A 2D $y - z$ cross sectional view of the CAL. The angular boundaries of the different calorimeter sections are shown.

Each section of the CAL was subdivided into towers with a front surface of 20×20 cm. Each tower was further segmented into one electromagnetic and one (in RCAL) or two (in BCAL and FCAL) hadronic sections. The difference between the proton and electron beam energies necessitated the extra material in the more forward regions. The electromagnetic section of each tower was further subdivided into two (in RCAL) or four (in BCAL and FCAL) cells to provide better angular resolution and avoid saturating cells. The electromagnetic cells of the BCAL were also projective, *i.e.* they point to the interaction point. 32 BCAL towers covered the entire azimuthal range. Between the towers there is a small region where particle detection is not possible. So to prevent particle loss in the regions between the towers they were rotated by 2.5° azimuthally.

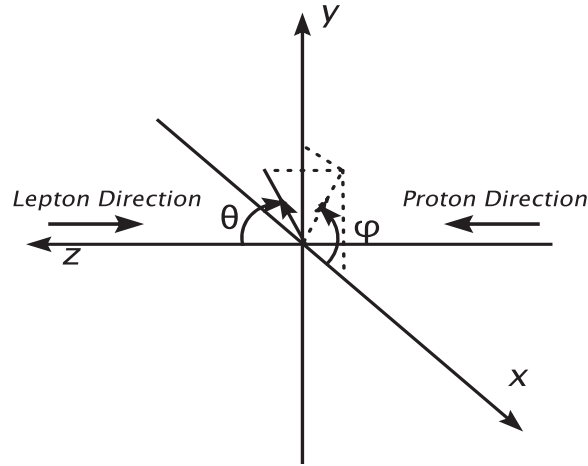


Figure 3.8: The 3D representation of the ZEUS coordinate system.

The ZEUS CAL was a sandwich-type sampling calorimeter. It used alternating layers of depleted Uranium absorber and SCSN-38 plastic scintillator to sample a fraction of each incident particle's energy. The Uranium absorber would absorb the majority of an incident particle's energy. The plastic scintillator would convert a fraction of the deposited energy into light, which was then passed to photomultiplier tubes (PMTs) for measurement via wavelength shifting light guides.

As discussed above electromagnetic and hadronic showers deposit their energy via different processes. In hadronic showers, which deposit energy via nuclear interactions, a non-detectable amount of energy is lost in overcoming the nuclear binding potential. As a result the signal response from an electromagnetic shower to that of a hadronic shower, e/h , is typically between 1.1 to 1.35. A e/h not equal to one is problematic because there is an fluctuating electromagnetic component to any hadronic shower. This can lead to a non-linear signal response to the hadronic shower. Cladding the uranium plates slightly lowered the electromagnetic energy response, without a

measurable change in the hadronic shower response. This provided a 3% reduction in e/h . It also reduced the signal from the uranium radioactivity which provided an improvement in energy resolution. By varying the thickness of the plastic scintillator plates e/h could be fine tuned to achieve $e/h = 1.00 \pm 0.05$. For 3.3 mm thick, $X_0 = 1.000$, uranium plates between two 0.4 mm, $X_0 = 0.023$ each, layers of steel cladding a scintillator thickness of 2.6 mm, $X_0 = 0.006$, was required to achieve unity for e/h . This provides a Molière Radius, R_M , of 2.00 cm.

The light from the scintillator was fed through wavelength shifting light guides into the PMTs for readout. Each calorimeter cell was readout using two PMTs. This provided redundancy to prevent the loss of an entire cell due to one faulty PMT. The dual readout also provided the ability to compare the measurements of the PMTs with each other. The use of PMTs in the digitization of the signal allowed for readout to use pulse timing of less than a nanosecond. The fast readout time avoided pileup from the signal of multiple bunch crossings. It was also important for the suppression of background from beam-gas interactions and cosmic rays. In Figure 3.12 the timing of the energy deposited into the calorimeter for different types of events can be seen.

Under single particle test-beam conditions the energy resolutions of the CAL for single particles were measured to be $\sigma(E)/E = 0.18/\sqrt{E}$ (GeV) for electromagnetic showers and $\sigma(E)/E = 0.35/\sqrt{E}$ (GeV) for hadronic showers [19].

3.4.3 ZEUS Barrel Presampler

To measure the showering before the BCAL the ZEUS Barrel Presampler (BPRES) was installed in 1998 just inside the BCAL. The BPRES consisted of 416 channels, one for each of the BCAL towers. Each channel had 2 SCSN-38 scintillator tiles, each tile

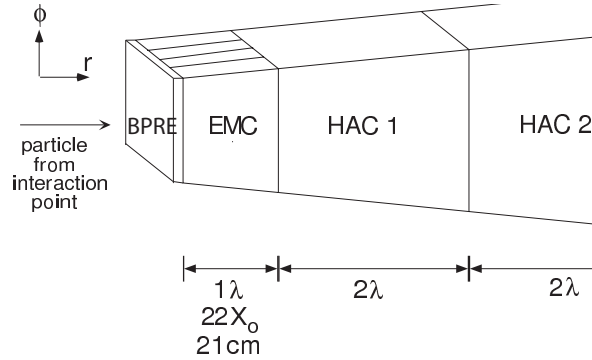


Figure 3.9: A diagram of a BCAL tower. The orientation of the Barrel Presampler, 4 electromagnetic cells, and 2 hadronic cells can be seen.

was 18×20 cm and 5 mm thick. Each tile had 2 embedded fibers that transport the light to PMTs for readout.

The signal from the BPRE was calibrated in minimum ionizing particle units (mips). 1 mip is the average amount of energy deposited in the BPRE by an energetic muon that traversed it and was calibrated with cosmic-ray muon data [20]. The measured energy was proportional to the number of charged particles that passed through it. The number of charged particles that passed through it was also proportional to the energy lost by the incident particles during their interaction with the inactive material in front of the BCAL.

3.4.4 Central Tracking Detector

The ZEUS Central Tracking Detector (CTD) was a cylindrical drift chamber. The CTD was contained within a superconducting solenoid, which provided a 1.4 Tesla magnetic field in the z direction. The strong magnetic field bends the particle trajectories. The track's curvature was proportional to the particle's momentum.

A drift chamber is a grouping of regularly spaced wires that are held at two elec-

tric potentials: signal (+) and potential (-). The chamber is filled with Ar:CO₂:C₂H₆ gas in a (85:13:2) mixture. As a charged particle moves through the gas it ionizes the gas, this produces negatively charged free electrons that drift toward the positively charged signal wire. When the electrons reach the wire they produce a measurable current pulse in the wire. The speed at which the electrons drift towards the wire is known, which enables accurate timing of the track to be possible. The timing of the arrival of the electrons to the wire can be used to determine the original position of the pulse along the wire. An example of this is shown in Figure 3.10.

The CTD was organized into nine concentric cylindrical superlayers. Each superlayer contained 32 to 96 drift cells. Each drift cell was comprised of 8 tungsten wires. The orientation of the wires within the superlayers was varied from one superlayer to another. This provided good accuracy in measuring the polar angle of the tracks.

3.4.5 ZEUS trigger System

The bunches that comprised the HERA beams crossed every 96 ns, yielding a bunch crossing frequency of 10.4 MHz. Not every bunch crossing caused an *ep* interaction. The actual rate of *ep* interactions of interest was around 10 Hz. Beam-gas interactions were the main source of background at a rate of around 100 kHz. To reduce the 10.4 MHz bunch crossing frequency to the manageable 10 Hz physics rate ZEUS utilized a 3-level trigger system. Each level reduces the number of events processed, allowing for an increasing complexity in the trigger system. The flow of data through the trigger system can be seen in Figure 3.13.

The First Level Trigger (FLT) was responsible for reducing the rate to several

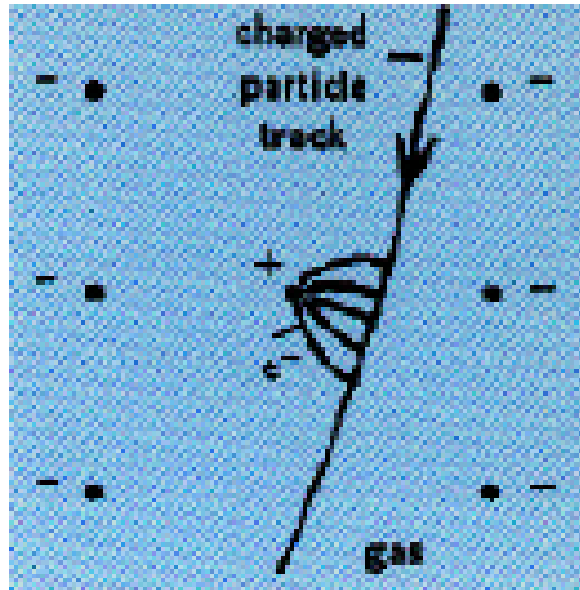


Figure 3.10: An example of a charged particle being detected by the signal wires of a drift chamber.

hundred Hz. In order to provide time for trigger data calculation and propagation each detector readout had a $5 \mu\text{s}$ pipeline to store the complete information about the event. Most components had their own individual FLT's which would provide a quick and basic triggering calculation which was then passed on to the Global First Level Trigger (GFLT) within $1.0 - 2.5 \mu\text{s}$ after the bunch crossing. The GFLT could then make a decision about keeping the event. The $4.4 \mu\text{s}$ GFLT trigger decisions, with the $5 \mu\text{s}$ pipeline, were done without deadtime, during which a subsequent potential event would have to be discarded rather than processed. The deadtime at the FLT was typically $1 - 2\%$, and was due to the detector readouts.

The lower rate provided by the FLT meant that the Second Level Trigger (SLT) could construct more complicated quantities to cut on. The SLT was constructed from a transputer-based network [19]. Transputers are a type of programmable micropro-

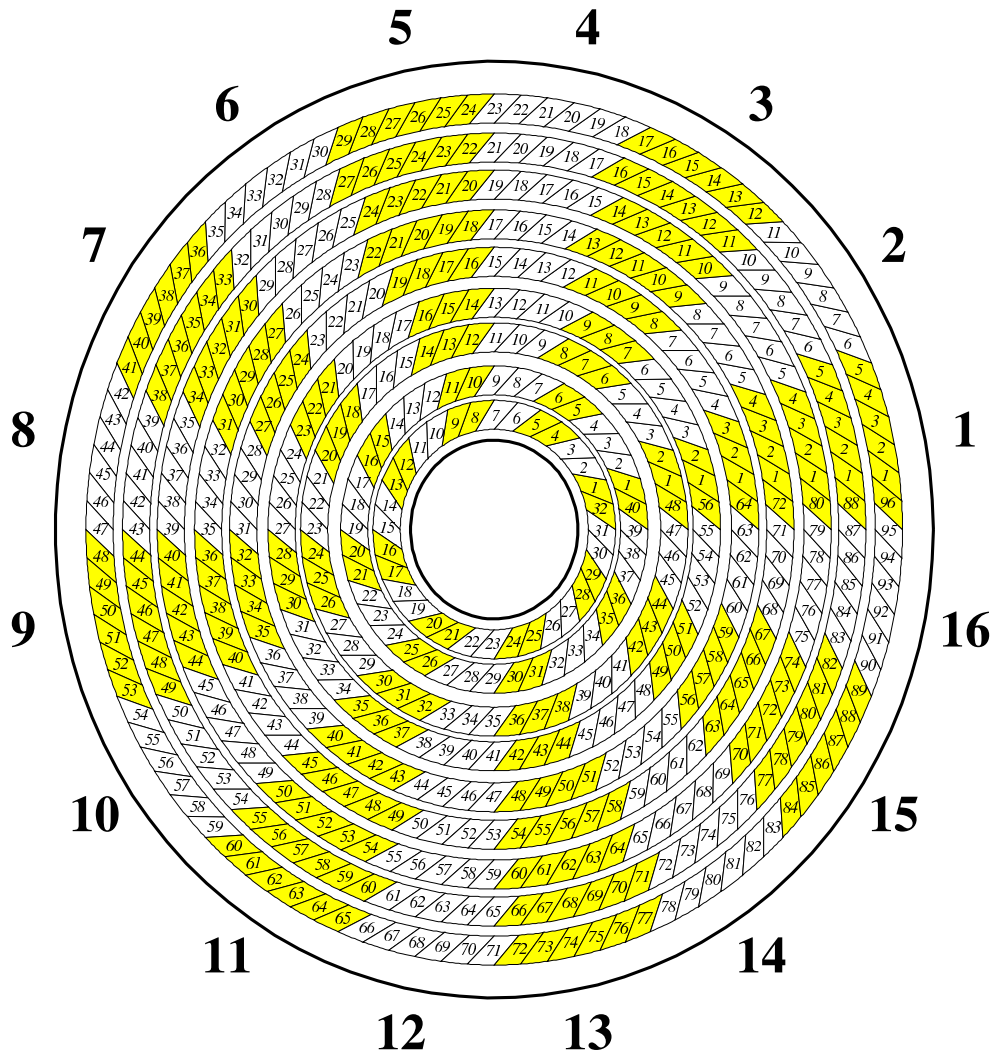


Figure 3.11: An $x - y$ view of the ZEUS CTD. The 9 concentric superlayer rings can be seen.

cessor with interprocessor links. The ability to provide precise timing played a key role in the rejection of the different forms of background events. In Figure 3.12 the timing of the energy deposited into the calorimeter for different types of events can be seen. In ep interactions the byproducts would radiate out and each arrive at the CAL at about equal times. In beam-gas interactions the particles would pass from one side of the CAL to the other, so each CAL component would see energy deposited at different times. Cosmic muons would be seen in the top of the CAL before being detected in the lower part of the CAL. The difference in detection time between the RCAL and FCAL, or top and bottom of the CAL, would indicate that event did not originate from the interaction of the two beams. The SLT longer computation times allowed for quantities such as tracking, basic vertex finding and $E - p_z$ calculations to be used. The output rate of the SLT was typically 30 – 100 Hz.

The output rate from the SLT was low enough to send all of the detector information into the Event Builder (EVB) which would then collect and format the data to pass it along to the Third Level Trigger (TLT). The TLT had about 100 ms to make a trigger decision. This allowed for the events to be passed through a reduced version of the full reconstruction software. The TLT was a processor farm with the reduced version of the full reconstruction software running in parallel on several systems. The output of the TLT was typically 5 – 10 Hz and was written to data storage tapes and disks for later analysis.

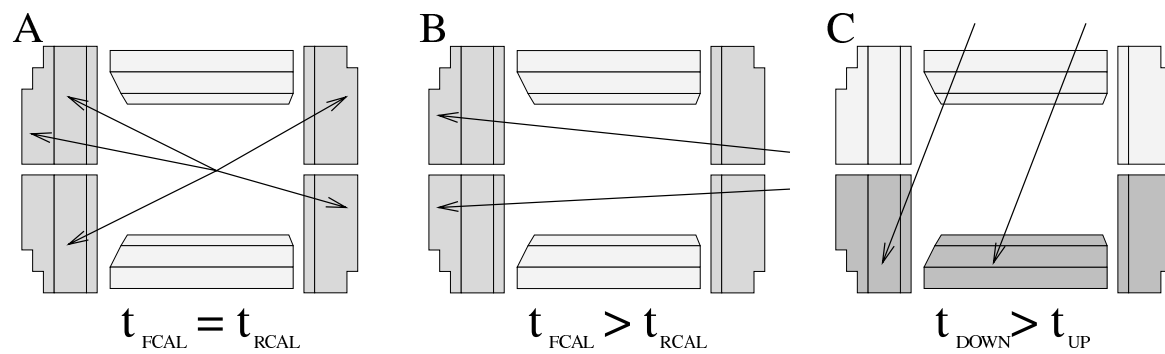


Figure 3.12: The timing of energy deposited into the calorimeter can be used to differentiate between different types of events. Figure A shows an ep interaction, Figure B shows a beam-gas interaction, and Figure C demonstrates a cosmic muon event.

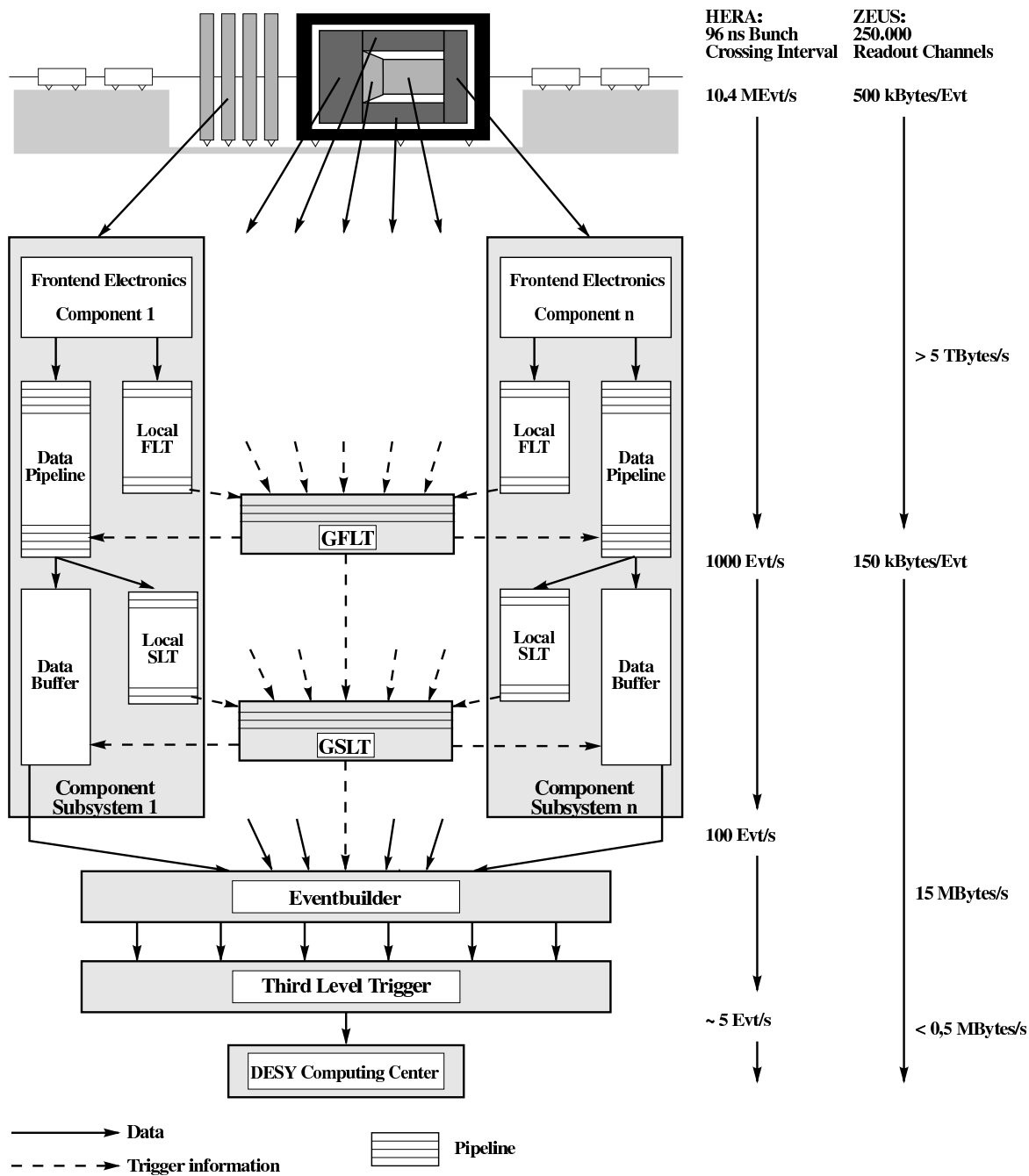


Figure 3.13: A diagram of the ZEUS 3 level trigger system and the DAQ system.

Chapter 4

Monte Carlo Simulation

Part of the scientific method is making a prediction before any measurement is made. Making that prediction comparable to experimental results requires a model of the parton, a calculation for the scattering amplitudes involved in the hard scatter, a model of the hadronization and decay of the particles as they depart the hard scatter and a simulation of how those particles are seen in the ZEUS detector. How the particles, in particular photons, are seen in the detector is a point of particular interest to this analysis. Once the events have been properly modeled the prediction can be used to remove any detector effects from the final result, allowing the final results to be more directly comparable to other experiments and theoretical calculations. All of these steps are handled via the Monte Carlo method for simulating events.

Monte Carlo Simulations use pseudo-random numbers weighted according to the underlying processes being modeled to statistically predict what will happen in the hard scatter. Each time the Monte Carlo event generator is run it provides a well defined list of particles that emerge from the hard scatter. That well defined list of particles is then passed through a simulation of how the particles evolve and decay as they approach the ZEUS detector. When the particles reach the detector they are

passed through a full simulation of how the ZEUS detector is expected to react to, and how the particles would be affected by, their passage into the ZEUS detector. This provides one simulated event that can be directly compared to an experimentally derived event. When this process is repeated a large number of times it is expected that the average simulated event topology will approach the average experimental event topology.

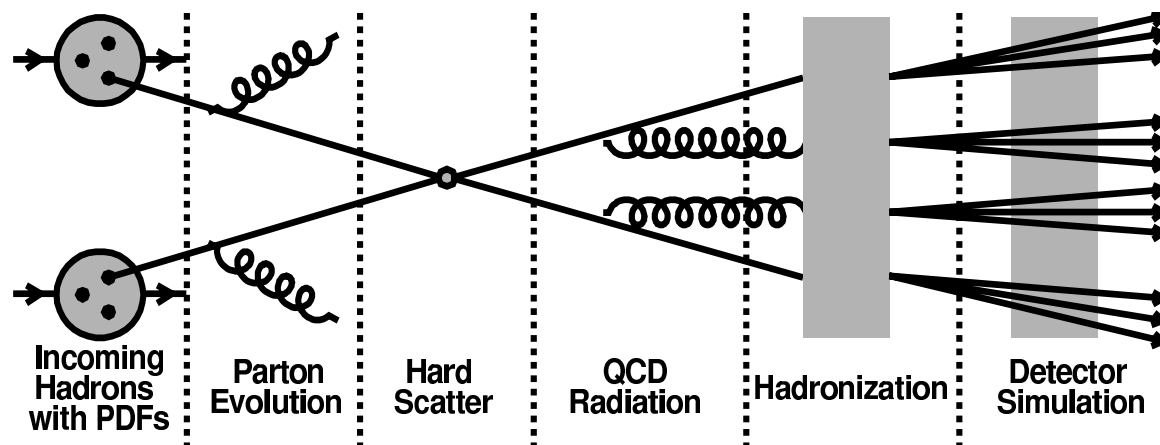


Figure 4.1: An illustration of the stages of a MC simulation of a HEP event.

4.1 Event Generators

The first stage in a MC simulation is the input of the parton density functions (PDF) that describe the incoming hadronic systems. PDFs represent the probability to find a parton at a certain Q^2 within a given range of momentum fractions of the proton, $[x, x + dx]$. PDFs cannot be determined theoretically, commonly used fits to experimental data of PDFs for the proton come from several groups. Groups of interest to this analysis include the Coordinated Theoretical-Experimental Project on QCD (CTEQ) [21, 22], Glück Reya Vogt (GRV) [23, 24, 25], Martin Roberts Stirling

Thorne (MRST) [26, 27, 28] and Frankfurt Freund Strikman (FFS) [63]. Once a PDF is chosen as the input for a MC program pQCD models can be used to extrapolate the Q^2 and x dependence of the PDF using a parton evolution equation. Commonly used parton evolution equations include DGLAP [30, 31, 32] and BFKL [33, 34].

In photoproduction the exchanged photon can fluctuate into a hadronic state and provide a quark or gluon that interacts with a parton from the proton (Section 1.4.1). A photon PDF is used to describe the probability to find a parton within that hadronic state at a certain Q^2 within a given range of momentum fractions of the exchanged photon, $[x_\gamma, x_\gamma + dx_\gamma]$. Photon PDFs are once again determined experimentally and are provided by several groups, *e.g.* GRV [23, 24, 25], Aurenche Fontannaz Guillet (AFG) [35] and Schuler Sjöstrand (SaS) [36].

4.2 Hard Scatter and QCD Radiation

Event generators employed in this analysis use pQCD to calculate the ep hard scatter to order $\mathcal{O}(\alpha^2\alpha_s)$. The probability distribution of the matrix elements and the available phase space creates a limited number of final state particles. The limited order in α_s gives rise to the necessity of other techniques to model higher order effects. The possibility that a particle going into, or out of, the hard scatter could emit a photon (QED radiation) or a gluon (QCD radiation) must be included in the prediction of the interaction. Radiation from the lepton before the hard scatter is known as initial state radiation (ISR). Radiation from the lepton after the hard scatter is known as final state radiation (FSR). The possibility to have an additional photon in the final state makes ISR and FSR of particular importance to a prompt photon analysis.

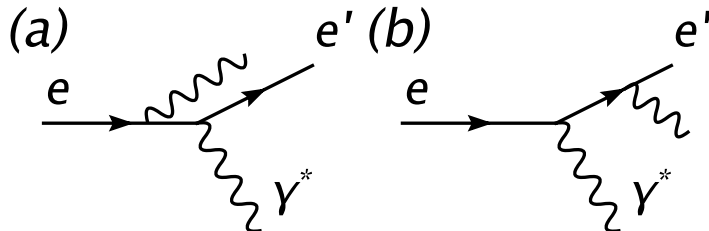


Figure 4.2: Diagrams of initial state radiation (a) and final state radiation (b). The virtual photon (γ^*) that takes part in the DIS interaction is also shown.

4.3 Hadronization

The point at which colored partons emerge from the hard scatter is referred to as the parton level. Although colored partons emerge from the hard scatter, QCD confinement does not allow free colored partons. The partons must undergo hadronization to form colorless stable particles. pQCD is not applicable over large distances with little momentum transfer, so a non-perturbative phenomenological model is required. Two common models used in MC programs are the Lund String Model [45] and the Cluster Model [43]. Once colorless stable particles have been formed the event is said to be at the hadron level. To be consistent with other experimental results, stable particles are defined as particles with a lifetime $t > 0.3ns$. One important property of photons is that they do not undergo hadronization. For a prompt photon the parton level is equivalent to the hadron level, however this not true for the other particles involved in the hard scatter.

4.3.1 Lund String Model

In the Lund String Fragmentation Model [45] the color field between a $q\bar{q}$ pair is represented as a one dimensional string with an energy of the order 1 GeVfm^{-1} . As

the quarks separate the energy stored in the string increases until there is enough to produce another $q\bar{q}$ pair. This process is repeated until there is too little energy left to give the strings to form new $q\bar{q}$ pairs. When that happens the partons are in colorless hadronic states that can then be passed to the detector simulation. One of the possible outcomes of the Lund String Hadronization Model is depicted in Figure 4.3.

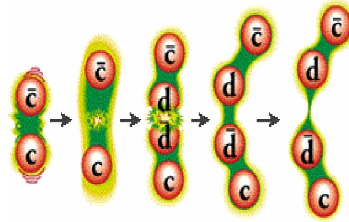


Figure 4.3: One possible example of the Lund String Hadronization Model in action.

4.3.2 Cluster Model

In the Cluster Model [43] gluons are split into $q\bar{q}$ or diquark anti-diquark pairs. Each $q\bar{q}$ or diquark anti-diquark is grouped with a neighbor to form colorless clusters. The clusters are then fragmented into hadrons depending on the available mass. Clusters with more mass are split into two hadrons depending on the available density of states. Clusters with little mass form the lightest hadron available to its quarks.

4.4 Detector Simulation

Once events have been simulated to the hadron level they must be passed through a simulation of how they interact with the ZEUS detector. When this is done MC events can be directly compared to experimental measurements. The first step in a detector simulation is to trace the path of each particle from the hard scatter through

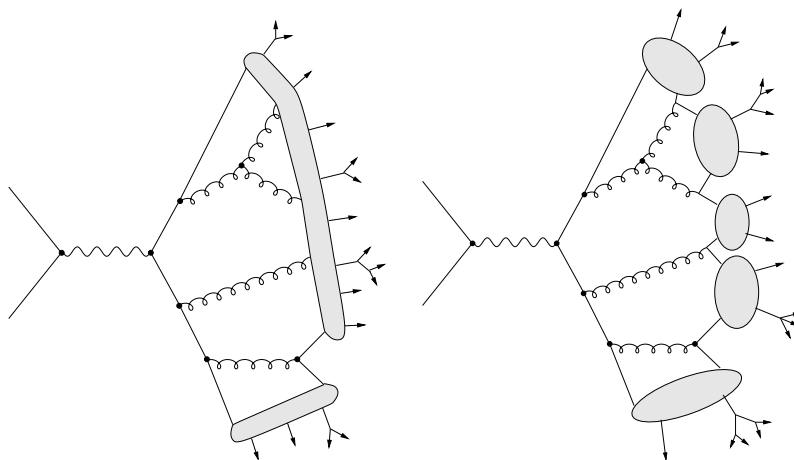


Figure 4.4: Diagrams of the Lund String Model (left) and the Cluster Model (right).

each of the detector's components. The detector simulation is done by the Monte Carlo for ZEUS Analysis, Reconstruction and Trigger (MOZART) program, which is based on the GEANT [37] package. GEANT takes as an input the detector geometry and material. The properties of the detector materials were determined from test beam studies. Some detector properties were refined with further studies of HERA data. The amount of dead material and the BCAL electromagnetic deposit response were refined with studies of Deeply Virtual Compton Scattering photons (Chapter 7) and DIS electrons from HERA data. After simulation of the detector response the event is then passed through a complete simulation of the online

trigger system done with the Zeus Geant Analysis (ZGANA) software library.

At this point the MC has calculated what every event would look like in the ZEUS detector components and trigger system. The MC events are then processed with the ZEUS Physics Reconstruction (ZEPHYR) program, which is the same program that is used to reconstruct experimental events. The same calibration constants are applied

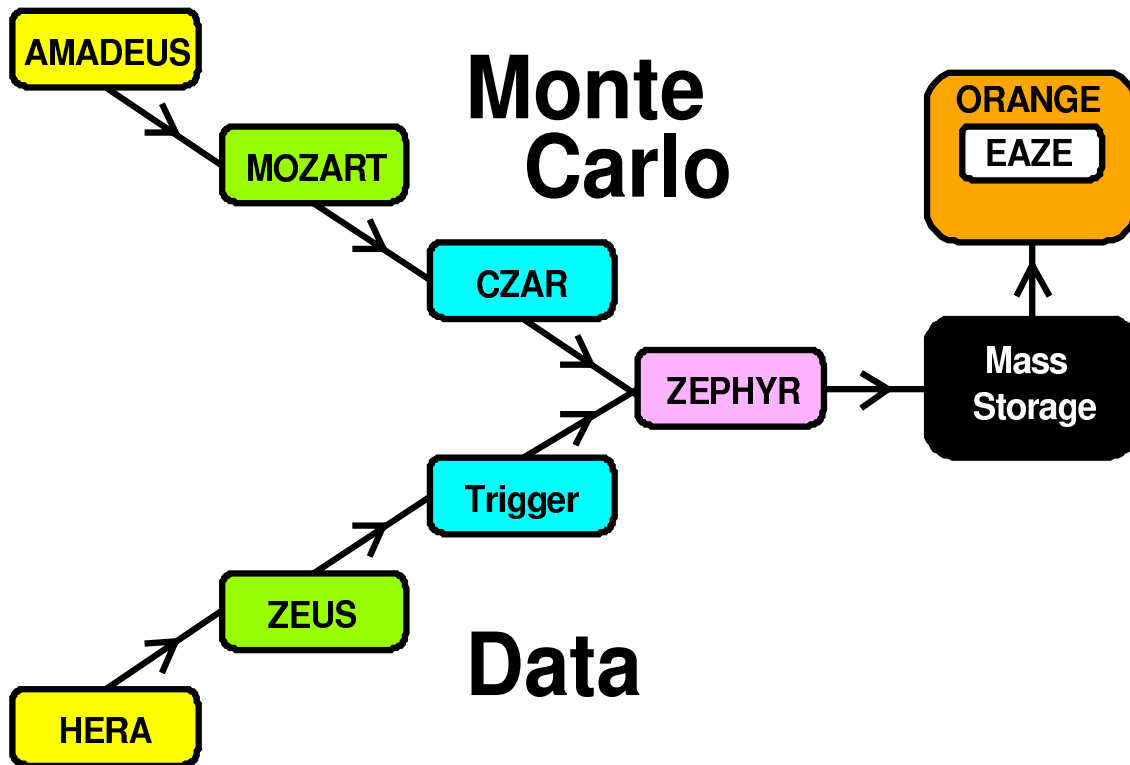


Figure 4.5: An illustration of the steps for processing ZEUS data and MC events.

to the MC as are used on the data. At this point MC events contain the same information that would be contained in an experimental event and this is referred to as the detector level. The information can then be taken and passed onto the analysis program, *i.e.* Easy Analysis of ZEUS Events (EAZE) program, to calculate quantities that are useful in describing the physics of an event. Figure 4.5 shows the steps for the processing of ZEUS data and MC events.

4.5 MC programs in HEP

There are several MC programs in the physicist's toolkit. While they vary in their implementation they all follow the same basic aforementioned approach. In particular

the manner with which they handle fragmentation must be considered. The differences in treatment of QCD radiation will also cause differences between the predictions.

In addition to MCs needed for prompt photon studies, MCs are also needed for Deeply Virtual Compton Scattering (DVCS). Details on those can be found in Chapter 7.3.

4.5.1 PYTHIA Monte Carlo Model

PYTHIA [40, 41, 42] uses the Lund string model (section 4.3.1) for fragmentation. PYTHIA includes terms for QED radiation. PYTHIA version 6.3 was used to generate a photoproduction sample of prompt photon with jet events in both direct and resolved processes and was also used to generate an inclusive dijet photoproduction sample without the prompt photon subprocess. The CTEQ5L [22] PDF was used for the proton and the SAS-2D [36] parameterization was used for the exchange photon PDF. The default parameters were used in the generation of the PHP MC sample. For the resolved process (Chapter 1.4.1) both the $(qg \rightarrow q\gamma)$ and $(q\bar{q} \rightarrow g\gamma)$ subprocesses were calculated. The direct and resolved samples were combined to match the x_γ^{meas} distribution (Chapter 5.7). To properly model the events for the acceptance correction the PHP MC sample was re-weighted in bins of E_T and η . The reweighting was performed in four-dimensional phase space in E_T and η of the photon and of the accompanying jet; thus correlations between these kinematic variables were properly taken into account. The prompt photon with jet sample and the inclusive dijet photoproduction sample were combined according to the method outlined in Chapter 8.1 to describe the data.

PYTHIA version 6.3 was also used to generate a DIS sample of prompt photon

events. The CTEQ5L PDF was used for the proton PDF. There was no re-weighting performed on the PYTHIA DIS MC sample.

4.5.2 HERWIG Monte Carlo Model

HERWIG [43, 44], which stands for Hadron Emission Reactions With Interfering Gluons, includes the effects of coherence and interfering gluons in the parton shower. QED radiation is not included in HERWIG. HERWIG uses the cluster model, section 4.3.2, for fragmentation.

HERWIG version 6.1 was used to generate a DIS sample of prompt photon events. The CTEQ4L [22] PDF was used for the proton PDF. No re-weighting was performed on the HERWIG DIS MC sample.

4.5.3 ARIADNE Monte Carlo Model

ARIADNE [46] version 4.12 was used to generate a neutral current inclusive DIS MC sample. QED radiation is included in ARIADNE. The CTEQ5D [22] PDF was used for the proton PDF. No re-weighting was performed on the inclusive ARIADNE DIS MC sample. The ARIADNE MC sample was combined with the PYTHIA prompt photon in DIS or the HERWIG prompt photon in DIS sample according to the method outlined in Chapter 9 to describe the data.

Chapter 5

Event Reconstruction and Selection

Events that pass the trigger are written to tape and later undergo a detailed reconstruction to combine the information from each of the ZEUS components to describe the event. During reconstruction the data are processed and corrected to ensure that the fundamental information (energies and tracks) is correct and accurate. This chapter describes the methods used to interpret the quantities provided by the ZEUS detector components in reconstructing the event and their use in selecting event samples.

5.1 Track and Vertex Reconstruction

Ideally each ep interaction would always occur at the nominal interaction point of the ZEUS detector. However, in practice this is not the case. In reality the beam positions are shifted in the xy plane. A slight shift in timing of the particle bunches will also cause a shift of the interaction point in the z direction. The finite size of the particle bunches¹ will also contribute to a shift away from the nominal interaction point. So the vertex must be reconstructed on an event-by-event basis from the

¹The lepton (proton) bunch has a transverse size of less than 0.07 (0.07) mm and a longitudinal size of less than 8 (85) mm.

tracking information. To do this the VCTRAK [47] program is used.

The VCTRAK program incorporates the information from all the tracking detectors, with the primary information coming from the CTD, to reconstruct the particle tracks and vertices of each event. To reconstruct the particle tracks VCTRAK begins by identifying seed track segments from the outermost axial superlayers of the CTD. A diagram of the CTD superlayers can be seen in Figure 3.11. Each seed is comprised of three hits in the outermost axial superlayers. Each seed is then iteratively extrapolated towards the inner superlayers beginning with the longest tracks. The trajectory of the track is recalculated as the information from the inner superlayers is added to the track. Tracks that share too many hits with other tracks are excluded. This process is repeated until all tracks that pass through the innermost superlayers are identified. The z position of the tracks is determined by the timing of the axial hits and is later refined by the information from the stereo superlayers.

The next stage of the VCTRAK program is to identify the tracks that do not pass through the innermost axial superlayers but do pass through at least two axial superlayers and one stereo superlayer. For this stage of track reconstruction a five parameter helix model is used to fit the hits to tracks. The five parameters used in the fit are illustrated in Figure 5.1. This fit begins with hits in the innermost superlayers and moves outwards.

Once the tracks are identified a χ^2 minimization procedure is performed to determine the primary and secondary vertices. After a track has been assigned to a vertex the track is recalculated using the vertex as an additional constraint.

To be used in this analysis tracks must pass the following minimum criteria to

ensure that they are well reconstructed:

- The track must have hits in at least 3 superlayers.
- The track must have $p_T > 0.10$ GeV.

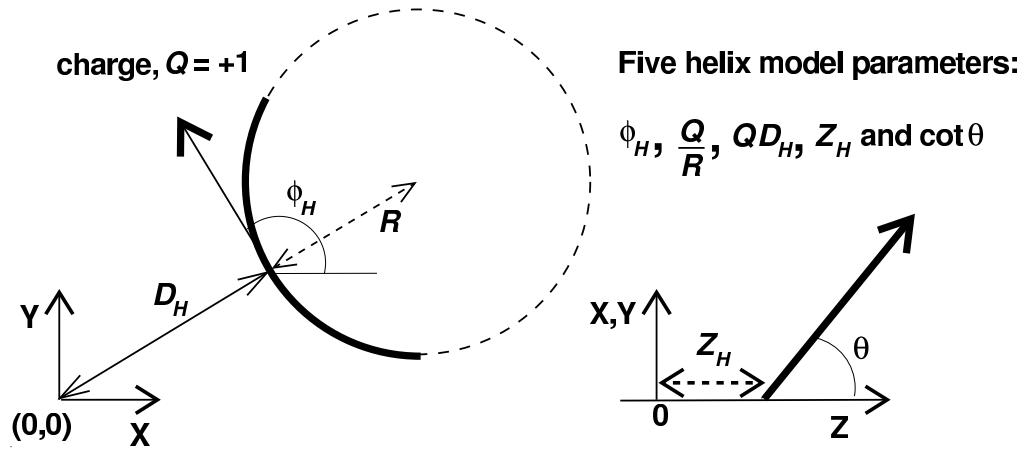


Figure 5.1: An illustration of the parameters used in helix fitting of CTD data to find tracks.

5.2 Calorimeter Reconstruction

The position and magnitude of energy deposits in the CAL are reconstructed from the cell positions, the pulse amplitudes from the two PMTs per cell, and the timing difference between the PMT pulses. Various procedures must be implemented to properly handle noise and energy loss in the detector to ensure the accuracy of the

calorimeter reconstruction. Once reconstructed the energy from groups of cells must be combined into clusters to describe a particle impacting the CAL.

5.2.1 Calorimeter Cell Removal

Radiation from the uranium absorber that comprises the CAL is one source of signal that does not originate from an ep interaction. The radiation is seen as a random, small, and frequent signal in the PMTs. To remove this signal cells are excluded when $E_{emc} < 80$ MeV, $E_{hac} < 140$ MeV, or with $E < 700$ MeV and $I_{cell} > 0.7$, where I_{cell} is the fractional energy difference between the two PMTs of a cell. There are also electronic sources can also cause noise in the calorimeter. Noisy cells can be easily identified because they fire more often and often have regular signals [48].

It is also possible that a spark travels between the housing of a PMT and the PMT itself. In this case one of the two PMTs on a cell will read a large signal while the other measures nothing. So the imbalance between the two PMTs can be used to identify PMT sparks. In this case cells with $|I_{cell}| > 0.9$ are removed.

5.2.2 Island Formation

Each cell has a finite size and there is a high probability that an energetic particle will traverse several cells before being completely absorbed. So to account for this cell granularity in the reconstruction of particles the energy deposited into the cells is clustered with neighboring cells. This clustering is performed separately over each EMC and HAC section of the CAL. A cell is clustered with its most energetic neighbor within the same EMC or HAC section. If the neighboring cell is already clustered with a different cell then the first cell is clustered with its neighbor and with

its neighbor's neighbor. This process is depicted in Figure 5.2.

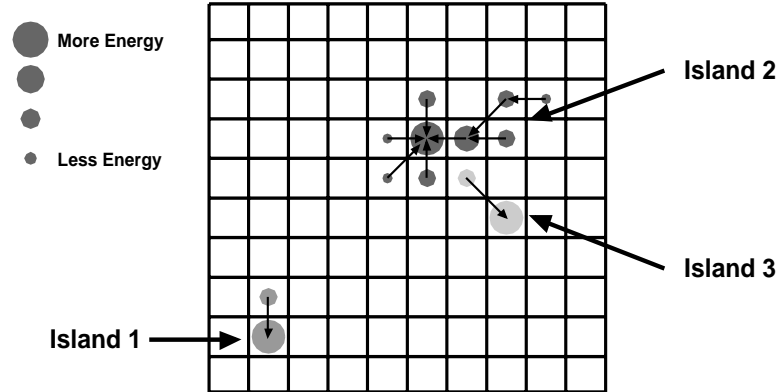


Figure 5.2: An illustration of the clustering of energy deposits to form CAL islands.

5.3 Energy Flow Objects (EFO)

To reconstruct the final state both the CAL and CTD information should be used. This will provide a better description of the final state particles. For instance the CTD has a better ability to accurately reconstruct low energy particles and particles that lose energy in the solenoid coil between the CTD and CAL. The combined reconstruction of particles with information from the CAL and CTD is known as the ZEUS Unidentified Flow Objects (ZUFOS) [49] within the ZEUS collaboration. Within ZEUS publications they are known as Energy Flow Objects (EFOs).

The formation of EFOs begins with CAL islands and CTD tracks. CAL islands are combined based on a probability function formed from the angular separation of

each CAL island. Each track is then extrapolated to the point where it would impact the CAL. If that impact point is within 20 cm of a CAL island then that track and island are clustered together into that CAL island's EFO. If the track does not get associated with an energy deposit then it forms its own EFO.

Once the tracks and islands are clustered into EFOs the decision must be made on how to reconstruct the object. The decision is simple for the following three cases:

- Charged tracks without an associated CAL island are reconstructed with the tracking information assuming the particle is a pion.
- CAL islands without an associated charged track are reconstructed with the CAL information.
- CAL islands with more than 3 associated tracks are reconstructed using the CAL information.

For the other cases (*e.g.* CAL islands with one associated track) studies have been carried out to determine which information best reconstructs the original particle and are detailed elsewhere [49]. A combination of tracking and CAL information might also be used, *e.g.* the CAL for the energy but the tracking for the angular position. It should also be noted that when the position is determined from the CAL islands the logarithmic center of gravity of the shower is used.

5.4 Jet Reconstruction

Up to this point a minimum amount of clustering has occurred in an attempt to group energy deposits and tracks together to describe the flow of energetic particles

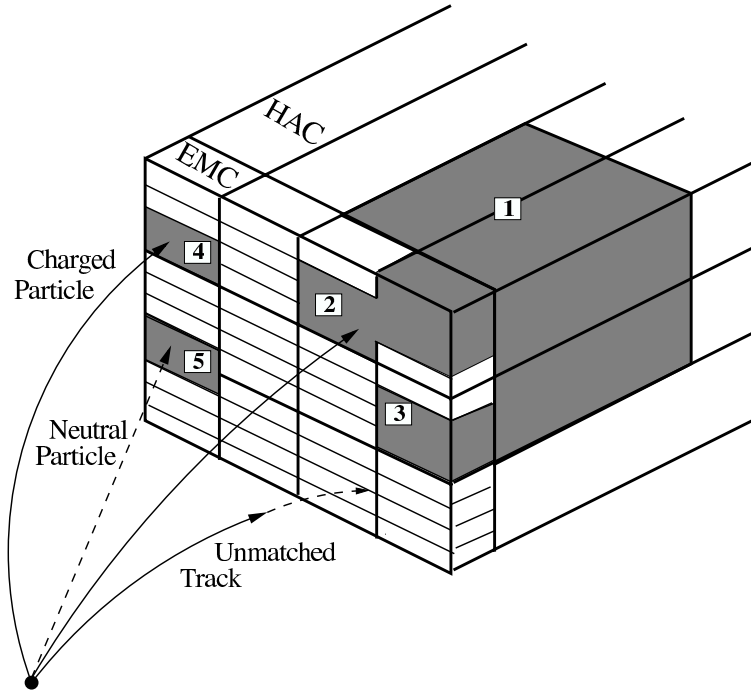


Figure 5.3: An illustration of the formation of EFOs from CAL islands and tracks.

through the detector. A further clustering will be undertaken in order to describe the flow of partons out of the hard scatter.

As was described earlier, in Chapter 4.3, when a parton is scattered out of the ep interaction it forms a shower of hadronic particles through the process known as hadronization. The energy associated with QCD radiation is on the order of 1 GeV, so the particles from the emitted parton will form a roughly collimated object known as a jet. Once the particles in the detector are grouped together to form a jet their information can be used to reconstruct the 4-momentum of the jet. With the 4-momentum of the jet you can calculate other kinematic descriptors of the jet, *e.g.* its transverse energy, E_T^{jet} , or its pseudorapidity, η^{jet} . For finding jets the algorithm applied needs to be stable when including soft or collinear particles, which is also

known as being infrared safe. Soft or collinear particles are low energy particles that are emitted by a particle and travel in a nearly identical path to the original particle.

5.4.1 Cone Algorithm

The EUCELL [50] cone algorithm defines jets by the Snowmass Convention [51]. In this formulation objects that exceed a minimum E_T are treated as seeds. Within the ZEUS implementation the minimum E_T is set to 1 GeV. Each seed is then treated as the center of a cone with a radius R_{cone} in $\eta - \phi$ space. Objects within that cone are added together and a new center point for the jet is recalculated as follows:

$$\begin{aligned}
 E_T^{jet} &= \sum_i E_{T,i} \\
 \eta^{jet} &= \frac{1}{E_T^{jet}} \sum_i E_{T,i} \eta_i \\
 \phi^{jet} &= \frac{1}{E_T^{jet}} \sum_i E_{T,i} \phi_i
 \end{aligned} \tag{5.1}$$

This process is repeated iteratively for each jet until the distance from the center of the previous cone to the current cone is less than a specified value, or until a maximum number of iterations is reached. For the ZEUS implementation the maximum number of iterations is set to 15.

With the cone algorithm some objects might not get included in any jet, which makes the cone algorithm appealing for hadron-hadron colliders, where a large number of particles should not get associated with any jet. The primary drawback of the cone algorithm is the lack of a convention for the treatment of overlapping jets. Therefore arbitrarily different implementations of the cone algorithm will find different jets for the same input and value of R_{cone} . Within the ZEUS implementation energy shared

by overlapping jets is associated with the highest E_T^{jet} . Another drawback is that the soft radiation between two jets can cause them to incorrectly merge into one jet. However an appealing aspect of the cone algorithm is that it is conceptually simple and computationally fast.

5.4.2 k_T Cluster Algorithm (KTCLUS)

Another way of clustering energy deposits and tracks to form jets is the k_T cluster algorithm, which was originally used in e^+e^- colliders [52]. Unlike the cone algorithm KTCLUS [53] begins by calling every input object a seed. In this analysis the input objects were the aforementioned EFOs. KTCLUS then iteratively combines objects to form larger objects until specific conditions have been met.

The KTCLUS algorithm begins by calculating the distance of every object from the proton beam line in momentum space (see Figure 5.4),

$$d_i = E_{T,i}^2 \tag{5.2}$$

and the distance between two objects as

$$d_{ij} = \min(E_{T,i}^2, E_{T,j}^2)[(\eta_i - \eta_j)^2 + (\phi_i - \phi_j)^2] \tag{5.3}$$

where i and j run over all input objects. If the minimum value is a d_{ij} value then objects i and j are combined into a new E_T weighted object k with

$$\begin{aligned}
E_{T,k}^2 &= E_{T,i}^2 + E_{T,j}^2 \\
\eta_k &= \frac{E_{T,i}\eta_i + E_{T,j}\eta_j}{E_{T,i} + E_{T,j}} \\
\phi_k &= \frac{E_{T,i}\phi_i + E_{T,j}\phi_j}{E_{T,i} + E_{T,j}}
\end{aligned}
\tag{5.4}$$

If the minimum value is a d_i value then the associated object is classified as a jet and is no longer merged. Once an object is classified as a jet it is removed from the list of objects. This process is repeated until all the objects are classified as jets.

Since the k_T algorithm begins with the smallest objects and combines them into larger objects it is infrared and collinear safe. There is also no ambiguity arising from overlapping jets.

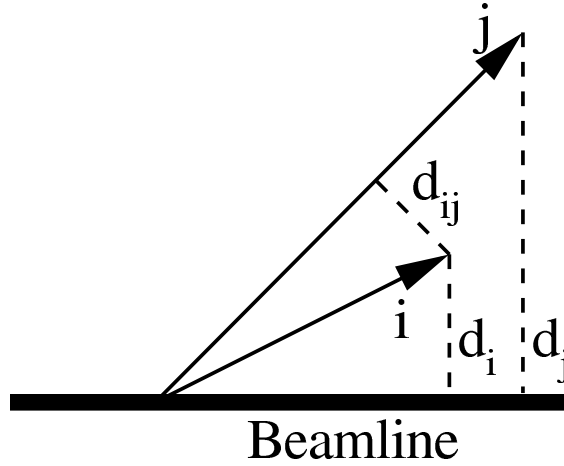


Figure 5.4: A diagram of the variables used in the KTCLUS Algorithm.

5.5 Electron Reconstruction

In addition to hadronic objects impacting the calorimeter there will also be particles that interact electromagnetically. Electromagnetic showers tend to be compact

and in the electromagnetic portion of the calorimeter. For reconstructing scattered electrons in the CAL the smallest discernible particle deposit is the CAL island (see Chapter 5.2.2). When an island is associated with a track it provides strong indication of a scattered electron. However the angular coverage of the CTD, $22^\circ < \theta < 157^\circ$, is smaller than the angular coverage of the CAL, $2.6^\circ < \theta < 178^\circ$. Hence there will be cases where the scattered electron is outside the CTD acceptance but inside the CAL acceptance. For this reason the initial description used to identify electrons is the energy distribution of the CAL island. Several other particles also deposit their energy via electromagnetic showers, *e.g.* π^0 . Fortunately they have a different shower profile. Any electron finding routine must have a high efficiency and a high purity.

5.5.1 SINISTRA

The workhorse used at ZEUS for finding scattered electrons is the SINISTRA [55] neural network program. The position, shape of the shower, and energy are all fed into a neural network that was trained on a large sample of neutral current DIS Monte Carlo. It outputs a probability that a particular island is a scattered electron. A probability greater than 90% is considered to be an electron candidate. If multiple candidates are found then the one with the highest probability that passes any other kinematic requirements is taken. If scattered lepton has an energy greater than 10 GeV the SINISTRA routine achieves both purities and efficiencies above 80%. The performance of SINISTRA was verified by a comparison to other electron finders [56].

Because of the more limited acceptance of the CTD the default choice is to calculate the electron's energy and position from the CAL information. If the electron is in a region of good acceptance of the CTD then an additional track requirement is

included. If there is a track and the electron is in a region of high CTD acceptance then the electron's scattering angle is calculated from the CTD track.

Hadronic jets may also form electromagnetic objects, so an additional isolation requirement is placed on the electron candidate. If there is greater than 5 GeV of energy in a cone of radius 0.8 around the CAL island in question, then it is rejected.

5.5.2 ELEC5

The ELEC5 [57] electron finder is similar to the SINISTRA electron finder but with much less stringent requirements. ELEC5 does not use tracking information in its requirements. It has a lower energy requirement. It also allows much wider clusters compared to SINISTRA. The importance of the ELEC5 electron finder to this analysis motivates presenting its steps in greater detail. The routine can be divided into the following four basic steps,

- **Seed Selection:** The 10 highest energy EMC cells with an energy above 1.0 GeV are considered as seeds for electron finding. If two seeds are within 12° of each other then only the higher energy seed is considered.
- **Cone Assignment:** For each seed cell the following cones are defined,

EMC inner region = EMC energy within a cone of radius 0.25 (rad)

EMC outer region = EMC energy in an annulus between cones of
radii 0.25 and 0.4 (rad)

HAC1 inner region = HAC1 energy within a cone of radius 0.3 (rad)

HAC2 inner region = HAC2 energy within a cone of radius 0.3 (rad)

- **Calculation of quality factor:** To distinguish between a compact electromagnetic shower and a broad hadronic shower the following four quantities were chosen:

Energy weighted radius of EMC energy within a cone of radius 0.25 (rad)

Ratio of EMC outer region to EMC inner region

Ratio of HAC1 inner region to EMC inner region + HAC1 inner region

Ratio of HAC2 inner region to EMC inner region + HAC2 inner region

The above four quantities are then used as inputs into probability functions to determine individual probabilities for each of them. The overall quality factor is the product of the four individual probabilities.

- **Selection of electromagnetic cluster:** Final candidates were selected based on the following four conditions:

$$\text{Number of Cells} \leq 35$$

$$\log_{10}(\text{Quality factor}) > -8$$

$$E_e = E_{EMC} + E_{HAC1} + E_{HAC2} > 2 \text{ GeV}$$

$$(E_{HAC1} + E_{HAC2})/E_e < 0.1 \text{ When PMT imbalance of seed cell} < 0.2$$

5.6 DIS Kinematic Reconstruction

After the particles, jets, and electrons have been reconstructed the kinematics of the ep scatter can be reconstructed. There are eight possible variables that describe a DIS event: the 4-momentum of the scattered electron and the 4-momentum of the

hadronic system. The conservation of energy and momentum provides 4 constraints. The fixed electron mass and center-of-mass energy, s , provided by HERA provide two more constraints. This leaves two independent variables that are needed to describe the DIS hard scatter. In order to provide a physically relevant description of the event there are three Lorentz-invariant variables are often used: the virtuality of the exchange boson (Q^2), the fraction of the proton momentum carried by the struck parton (x_{BJ}), and the inelasticity (y). There are only two degrees of freedom between the three variables which are related by,

$$Q^2 = xys \tag{5.5}$$

For reconstructing Q^2 , x_{BJ} , and y there are four quantities used: the energy (E'_e) and polar angle (θ_e) of the scattered electron, and the energy (E_h) and polar angle (γ_h) of the hadronic system. Since only two variables are needed the combination can be chosen that provides the best reconstruction for the kinematic range considered. There are three common combinations used by the ZEUS collaboration. The scattering angle of the hadronic system can be found from,

$$\cos \gamma_h = \frac{(\sum P_x)^2 + (\sum P_y)^2 - (\sum E - P_z)^2}{(\sum P_x)^2 + (\sum P_y)^2 + (\sum E - P_z)^2} \tag{5.6}$$

where the sum runs over all the final state particles excluding the electron.

5.6.1 Electron Method

The electron method, as the name might suggest, takes only the information from the incoming and scattered electron to reconstruct Q^2 and y :

$$\begin{aligned}
 Q_{el}^2 &= 2E_e E_e' (1 - \cos \theta_e) \\
 y_{el} &= 1 - \frac{E_e'}{2E_e} (1 + \cos \theta_e) \\
 x_{el} &= \frac{Q_{el}^2}{s y_{el}}
 \end{aligned} \tag{5.7}$$

The electron method produces a good reconstruction of Q^2 and x over the entire kinematic range, but underestimates them at higher values of Q^2 and x .

5.6.2 Double-Angle Method

The double-angle method, as the name might suggest, takes only the polar angles of the scattered electron and hadronic system to describe the system.

$$\begin{aligned}
 Q_{DA}^2 &= 4E_e^2 \frac{\sin \gamma_h (1 + \cos \theta_e)}{\sin \gamma_h + \sin \theta_e - \sin (\theta_e + \gamma_h)} \\
 y_{DA} &= \frac{\sin \theta_e (1 - \cos \gamma_h)}{\sin \gamma_h + \sin \theta_e - \sin (\theta_e + \gamma_h)} \\
 x_{DA} &= \frac{E_e}{E_p} \times \frac{\sin \gamma_h + \sin \theta_e + \sin (\theta_e + \gamma_h)}{\sin \gamma_h + \sin \theta_e - \sin (\theta_e + \gamma_h)}
 \end{aligned} \tag{5.8}$$

The double-angle method provides an improvement in the description of Q^2 and x at higher values compared to the electron method, but worse resolution at lower values of Q^2 and x [54].

5.6.3 Jacquet-Blondel Method

A third reconstruction technique, the Jacquet-Blondel method, takes only information from the hadronic system to describe the scatter.

$$\begin{aligned} Q_{JB}^2 &= \frac{(\sum_i p_{x,i})^2 + (\sum_i p_{y,i})^2}{1 - y_{JB}} \\ y_{JB} &= \frac{\sum_i E_i(1 - \cos \theta_i)}{2E_e} \end{aligned} \quad (5.9)$$

where the sum runs over all the final state particles excluding the electron. The Jacquet-Blondel method does not depend on the reconstruction of the scattered lepton and is therefore desirable for background rejection in cases where a particle was misidentified as the scattered lepton.

5.7 Photoproduction Kinematic Reconstruction

The kinematics of photoproduction events are characterized by the fraction of the exchanged photon involved in the collision (x_γ) and $Q^2 \approx 0$. In photoproduction the scattered electron escapes down the beam pipe and cannot be measured. For this reason the Jacquet-Blondel method, with the addition of x_γ , is used to reconstruct the event kinematics. In this analysis we are concerned with prompt photons with an associated jet so the kinematic equations simplify to,

$$\begin{aligned} y_{JB} &= \frac{\sum_i E_i(1 - \cos \theta_i)}{2E_e} \\ x_p &= \frac{\sum_{i=jet} E_i(1 - \cos \theta_i)}{2E_p} \\ x_\gamma &= \frac{\sum_{i=\gamma,jet} E_i(1 - \cos \theta_i)}{2E_e y_{JB}} \end{aligned} \quad (5.10)$$

The incoming hadronic system has an $\sum(E - P_z)$ of zero since all of its momentum is directed in the $+z$ direction. By using the conservation of energy and momentum

we can see that the $\sum(E - P_z)$ of the hadronic system after the interaction is from the transfer of energy and momentum from the lepton to the hadronic system. The $(E - P_z)$ of the incoming lepton is $(2E_e)$ because all of its momentum is directed in the $-z$ direction. To calculate the fraction of the incoming lepton's momentum involved in the collision we can just divide the $E - P_z$ transferred to the hadronic system by the lepton's initial $E - P_z = 2E_e$. It should be remembered that in photoproduction there is no observed scattered lepton, therefore the sum will run over all observed objects.

In photoproduction there is a chance that only a fraction of the exchange photon's momentum will be involved in the collision (Section 1.4.1). As a result not all of the momentum transferred from the incoming lepton, $E_e y_{JB}$, will be involved in the hard scatter. In other words, there can be energy flow that was not directly involved in the hard scatter. To leading order the prompt photon and the jet represent the system emerging from the hard scatter. So dividing $\sum_{i=\gamma, jet}(E - P_z)$ by the momentum transferred from the incoming lepton the fraction of the exchange photon involved in the hard scatter can be reconstructed.

5.8 Event Selection

There are several features that distinguish a prompt photon event from background. An isolated photon should leave a narrow energy deposit in the electromagnetic section of the BCAL. Photons from a jet are not very well isolated. There will also be a tendency for the hadronic system to form a balancing jet opposite the photon. This will provide tracks in the CTD that will allow the vertex to be well reconstructed. For DIS events there will also be a scattered electron, that will be absent for PHP

events.

5.8.1 Offline Selection

After an event has passed the online trigger selection (Section 3.4.5) it is passed through the ZEUS reconstruction software. Once commonly used quantities that characterize events are calculated the events are categorized according to the trigger filters they pass and their fully reconstructed quantities.

Events were pre-selected according the third level trigger selection, TLT bit HPP-16, which selects events with an electromagnetic energy deposit with $E_T > 3.5$ GeV and $|\eta| < 2.6$. It also requires at least one good track and a well-reconstructed vertex with $|Z_{vertex}| < 60$ cm.

5.8.2 PHP Kinematic Requirements

The prompt photon with jets in photoproduction data sample was taken during the 1999-2000 electron and positron HERA running periods, corresponding to an integrated luminosity of $77.1 \pm 1.6 \text{ pb}^{-1}$. In order to produce a clean sample of PHP events, the following cuts were used:

- No SINISTRA electron Candidate in the RCAL
- No SINISTRA electron Candidate with an associated track
- $0.2 < Y_{jb} < 0.8$
- $|Z_{vertex}| < 50$ cm
- Missing transverse momentum, $P_{T,miss} < 10$ GeV

The requirements on the SINISTRA electron candidate and $Y_{jb} < 0.8$ are to reject DIS events. The $0.2 < Y_{jb}$ and $|Z_{vertex}|$ requirements reject beam-gas background and ensure that the event is well reconstructed. To reject charged current events, where a W^\pm boson produces an undetected high energy neutrino, the missing transverse energy reconstructed from EFOs was required to be less than 10 GeV.

5.8.3 Jet Selection

After the prompt photon trigger level and PHP requirements, events were also selected with at least one KTCLUS jet with $6.0 < E_T^{jet} < 17.0$ GeV and $-1.6 < \eta^{jet} < 2.4$. To ensure the hadronic nature of the jet it was also required to deposit some energy in the hadronic section of the calorimeter, $\frac{E_{emc}^{jet}}{E_{tot}^{jet}} < 0.9$. If more than one jet is found that satisfies the requirements then the one with the highest E_T^{jet} was used. A byproduct of the presence of a jet is the assurance that there will be tracks in the event and that the vertex will be well reconstructed. A typical prompt photon with an associated jet in PHP event can be seen in Figure 5.5. There are three important features that should be noted. The first is the well isolated and compact high- E_T^γ photon in the bottom of the BCAL. The second is the lack of activity in the RCAL which is indicative of photoproduction. The third is the hadronic jet in the FCAL.

Figure 5.6 shows the comparison between data and the predictions from PYTHIA for the prompt photon with associated jet in PHP sample. The Y_{jb} distribution reconstructed from the calorimeter information is reasonably well described. The level of agreement is similar to that seen in previous ZEUS photoproduction analyses [59]. The missing P_T distribution, though it contains a systematic shift near the peak is well described in the region of the cut at 10 GeV. The Z_{vertex} distribution is also well

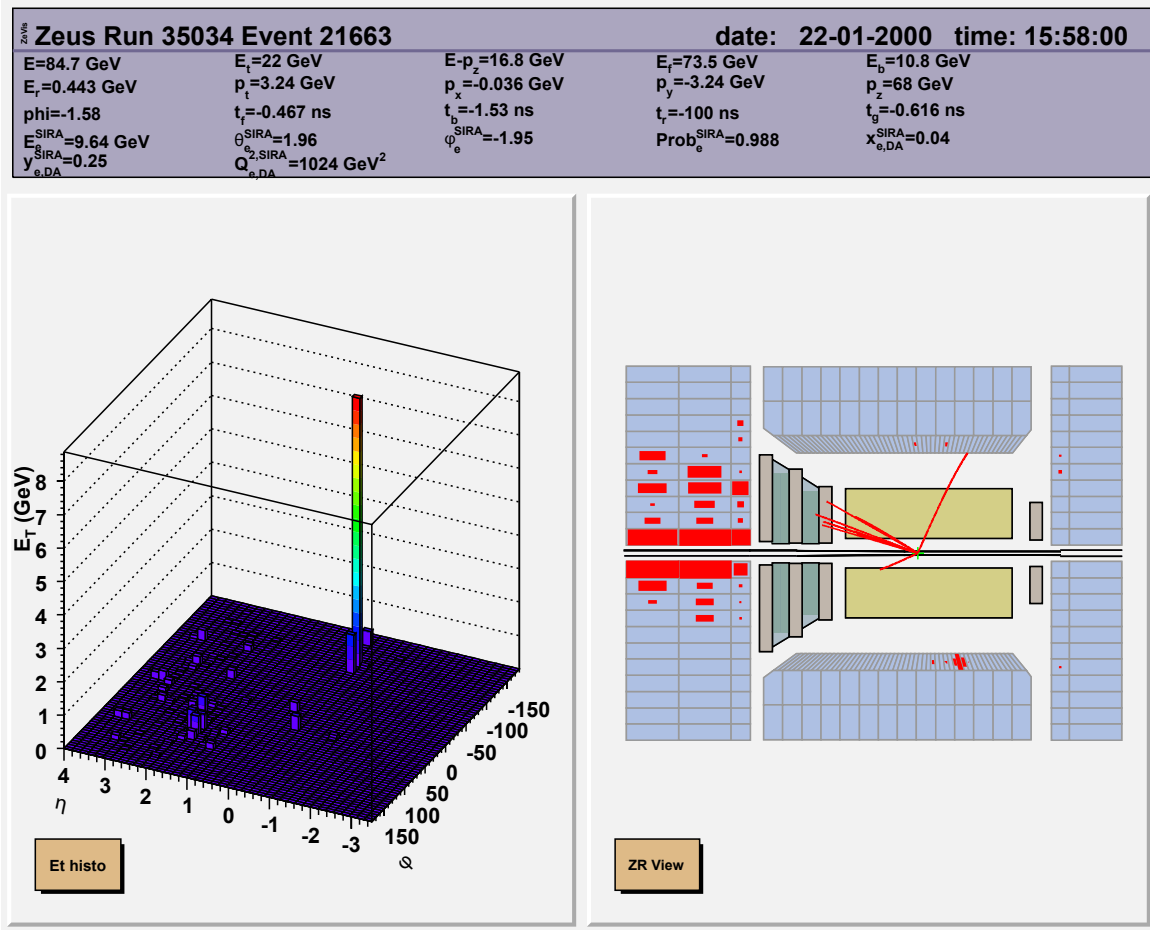


Figure 5.5: A typical prompt photon with an associated jet event in PHP

described. All of the distributions are sufficiently well described in the region of their respective cuts to be used to obtain the prompt photon with associated jet in PHP sample.

5.8.4 DIS Kinematic Requirements

The prompt photon Deep Inelastic Scattering data sample was taken during the 2004-2005 electron HERA running period, corresponding to an integrated luminosity of 109 pb^{-1} . In order to produce a clean sample of DIS events, the following cuts were

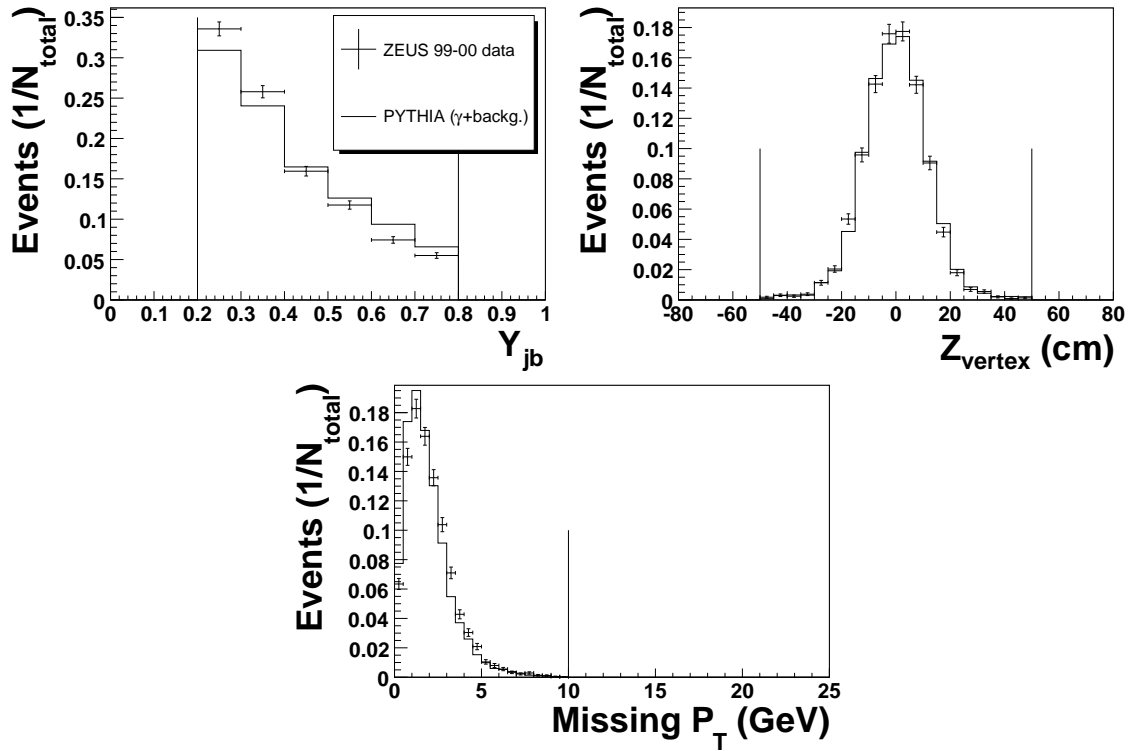


Figure 5.6: Distributions for the kinematic variables Y_{jb} , Z_{vertex} , and $P_{T,miss}$ from the PHP prompt photon with jets data sample (crosses) compared to PYTHIA 6.2 (histogram) after full event selection. The vertical lines mark the placement of cuts described in Section 5.8.2.

used:

- A good SINISTRA electron candidate (*i.e.* higher than 90% probability that it is an electron) in the RCAL.
- The good SINISTRA electron candidate must have $E_{el} > 10$ GeV
- The good SINISTRA electron candidate should not be in the inner ring of FCAL or RCAL towers near the beam pipe

- $|Z_{vertex}| < 40$ cm
- At least 2 vertex tracks
- $35 < E - P_z < 65$ GeV
- A BCAL photon candidate, (photon finding is detailed in Chapter 6)
- $Q_{el}^2 > 35$ GeV

The SINISTRA electron finder is used to locate the scattered electron. Requiring the SINISTRA electron candidate to be in the RCAL ensures that it will be well separated from the photon candidate which is required to be in the BCAL. The minimum energy and requirement that it be not near the beam pipe ensures that the scattered electron will be well reconstructed. A well contained DIS event will have a total $E - P_z$ of 55 GeV, twice the initial electron energy. In photoproduction the electron escapes down the beam pipe and the total $E - P_z$ in the calorimeter is what was transferred from the lepton to the hadronic system, leading to a low value for $E - P_z$. The $35 < E - P_z$ and $|Z_{vertex}|$ requirements will reject beam-gas background and photoproduction events as well as ensuring that the event is well reconstructed. When events with large initial-state QED radiation occur there is less momentum available from the lepton to be involved in the hard scatter, which provides less $E - P_z$ for the event. The $35 < E - P_z$ cut will also remove events with large initial-state QED radiation. Cosmic-ray background events do not have an upper limit on the energy they can deposit in the calorimeter. When cosmic-ray events are reconstructed with a nominal vertex they can appear to have high values of $E - P_z$. The $E - P_z < 65$ cut will remove energetic cosmic-ray background events. If there are more than 2 vertex

tracks in the event it assures both that the vertex is well reconstructed and will remove Deeply Virtual Compton Scattering events, which would only have up to one track.

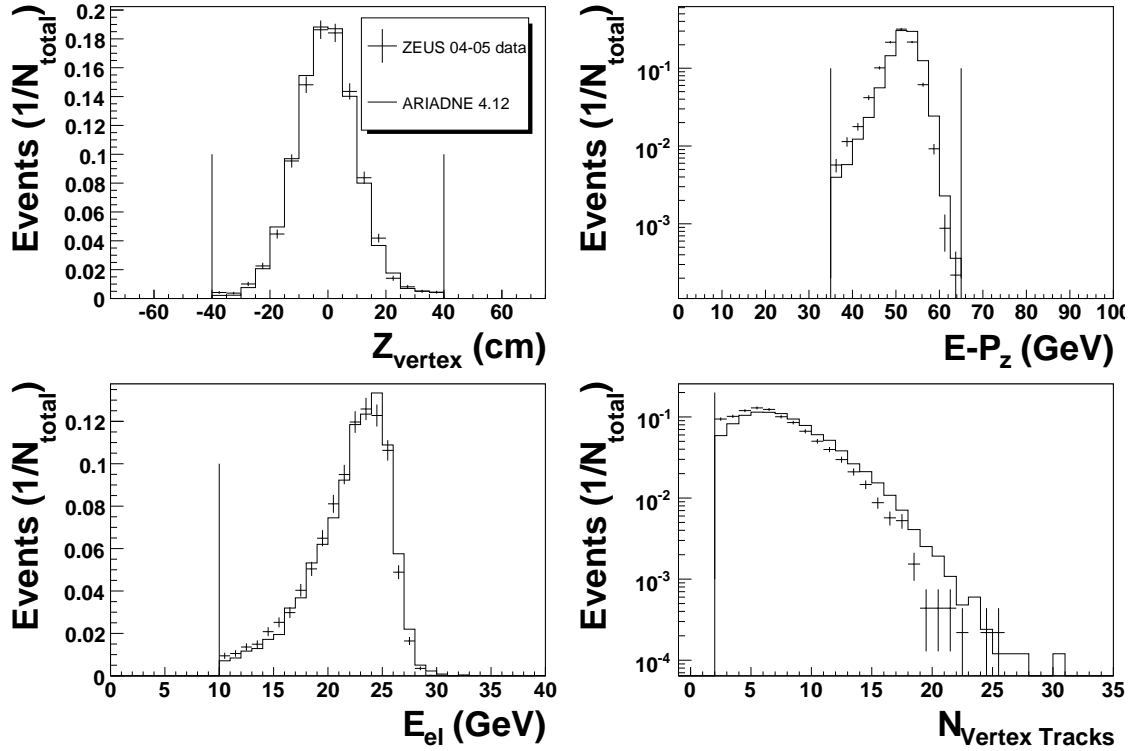


Figure 5.7: Distributions for the kinematic variables $E - P_z$, Z_{vertex} , E_{el} , and Number of Vertex Tracks from the inclusive DIS prompt photon data sample (crosses) compared to the predictions from ARIADNE 4.12 (histogram) after full event selection. The vertical lines mark the placement of cuts described in Section 5.8.4.

Figure 5.7 shows the comparison between data and the predictions from ARIADNE for the inclusive prompt photon in DIS event sample. While the $E - P_z$ distribution contains a slight shift from the peak value at twice the initial electron energy its behavior is stable near the cut at 35 GeV. As expected this probably originates from the slight shift in the energy of the scattered electron, which is also well behaved near

the cut $E_{el} > 10$ GeV. The number of vertex tracks is not very well simulated but is similar in quality to previous ZEUS prompt photon studies [5]. The Q_{el}^2 distribution, shown in Figure 5.8, is well described by the theoretical prediction from ARIADNE.

A typical prompt photon in DIS event can be seen in Figure 5.9. There are three important features that should be noted and compared to the PHP event shown in Figure 5.5. The first is the well isolated and compact high- E_T^γ photon in the bottom of the BCAL. The second is the scattered electron in the RCAL. In PHP the scattered electron escapes down the beam pipe. The third is the hadronic activity in the FCAL. For the PHP sample a hadronic jet was required, whereas for the DIS sample no specific jet requirements are used.

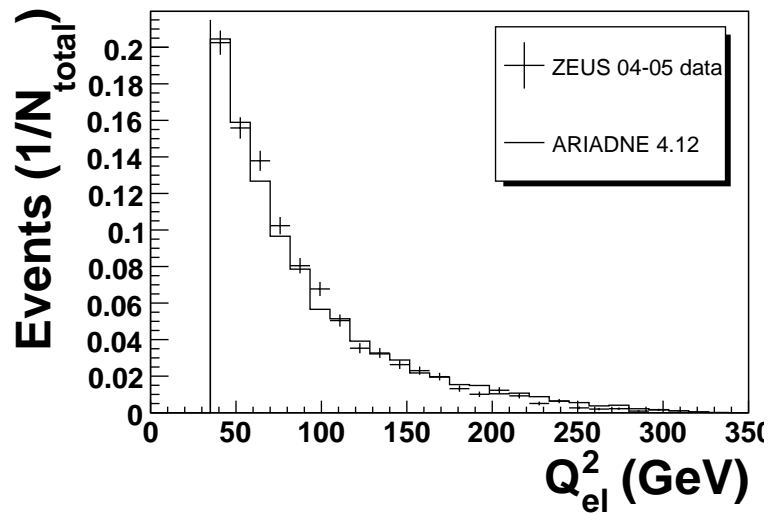


Figure 5.8: The Q^2 distribution for the inclusive DIS prompt photon data sample (crosses) compared to the predictions from ARIADNE 4.12 (histogram) after full event selection.

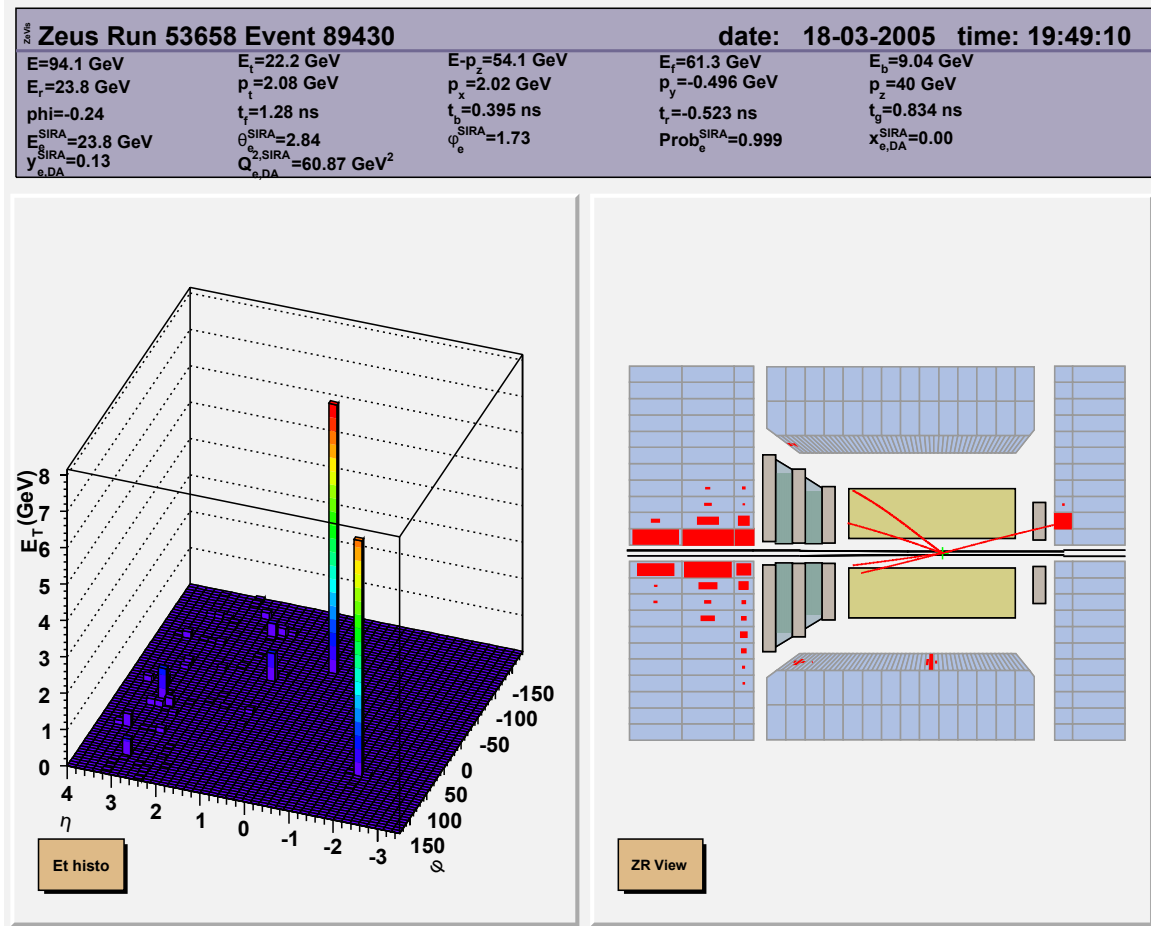


Figure 5.9: A typical prompt photon in DIS event.

Chapter 6

Photon Selection and Reconstruction

Having established a clean Photoproduction and Deep Inelastic Scattering sample in Chapter 5 the next step is to identify and evaluate the likelihood that a particular photon candidate is a photon. Prompt photons appear as compact, trackless electromagnetic energy deposits in the calorimeter. Unfortunately, neutral mesons such as π^0 and η particles leave similar deposits. However, when neutral mesons decay into multiple photons, *e.g.* $\pi^0 \rightarrow \gamma\gamma$, they tend to have wider energy deposits than a single photon. The opening angle, α , between two photons, with energies E_1 and $E_{\pi^0} - E_1$, that originate from the decay of a π^0 particle can be calculated as follows:

$$\alpha = 2\sin^{-1} \left(\frac{m_{\pi^0}}{\sqrt{E_1(E_{\pi^0} - E_1)}} \right) \quad (6.1)$$

The opening angle between the two photons is smallest when they have the same energy. To estimate the distance between the two photons when they reach the calorimeter assume the two photons travel the shortest distance from the interaction point to the barrel calorimeter, which is 125.6 cm. Then the distance between the two photons when they reach the calorimeter is given by:

$$D \approx 2 * 125.6 * \tan \left(\sin^{-1} \frac{m_{\pi^0}}{2E_1} \right) \text{ cm}, \quad (6.2)$$

For a π^0 with an energy of 5(10) GeV this will give a separation of 6.8(3.4) cm. This is comparable to the width of the barrel calorimeter's cells in the z direction of 5.45 cm. This separation will be larger or smaller on an event-by-event basis due to the uncertainty of the position of the π^0 particle when it decays and the possible asymmetry in the energies of the emerging photons. Similar estimates for the separation of photons from the decay of η particles give even wider separations.

The width of an energy deposit in the calorimeter is not the only information that we can gather to evaluate the likelihood that a particular energy deposit is a photon. As a photon travels from the interaction point to the calorimeter it can convert into an e^+e^- pair in the inactive material in front of the barrel calorimeter. The more photons you start with, the greater the probability that at least one will convert.

Two photon finders are used at ZEUS. The first is ELEC5, described in Section 6.2, is a modified version of the ELECRPOL [58] electron finder. The second utilizes the jet finder KTCLUS to find photons, as described in Section 6.3. Both photon finders utilize information about the transverse shape of the energy deposit and the conversion probability to evaluate a particular photon candidate. The use of two photon finders, one based off of an electron finder and one based off of a jet finder, provided two valuable perspectives for investigating the shape of a photon's electromagnetic shower as well as its isolation.

6.1 General Photon Requirements

Independent of the choice of photon finder, there are several universal requirements. In order to distinguish the photon from the scattered lepton, the photon candidate is required to be in the barrel calorimeter. This restricts the search to a region of good acceptance for the central tracking detector. It also removes any possibility of double counting an energy deposit as both the photon and the scattered lepton. To further remove any scattered leptons we require the photon candidate not have a track within 0.2 in Δr given by:

$$\Delta r = \sqrt{(\eta^\gamma + \eta^{track})^2 + (\phi^\gamma + \phi^{track})^2} \quad (6.3)$$

In order to discriminate between photons and neutral mesons the transverse energy of the photon, E_T^γ , is required to be within $5.0 \leq E_T^\gamma \leq 20.0 \text{ GeV}$. The requirement that the photon be in the barrel calorimeter restricts the pseudorapidity to a range of $-0.7 \leq \eta^\gamma \leq 0.9$.

6.2 ELEC5

The ELEC5 photon finder is a modified electron finder similar to the Sinistra electron finder described in Section 5.5.1 that is used to find the scattered lepton. There are several important differences. One is that the ELEC5 photon finder does not require that the energy deposit have a track associated with it. ELEC5 also allows the energy deposit to be wider and have a lower energy compared to Sinistra.

A further isolation requirement is placed on the ELEC5 photon candidate. A unit cone, radius of 1.0 in $\eta - \phi$ space, is placed around the photon candidate. The

sum is then taken of all the energy for the cells within that cone. It is required the photon candidate contain at least 90% of the energy in the unit cone.

6.3 KTCLUS

To use the KTCLUS jet finder to find photons it is run in inclusive mode over energy-flow objects (EFOs), that are based on a combination of track and calorimeter information. A jet is a photon-candidate when it satisfies several requirements in addition to the general photon requirements. The first is that at least 90% of the photon-candidate's energy must be in the EMC section of the barrel calorimeter. Secondly, the photon-candidate must consist entirely of EFOs without associated tracks. KTCLUS's innate ability to work with tracking information leads to a more natural track association criteria. This gives KTCLUS additional power when it comes to background rejection. Compare the distance between the photon candidate and the closest track for the prompt photon MC in Fig. 6.1 to the background MC in Fig.6.2. In the region $\Delta r > 1.1$ the two methods are in fairly good agreement for both the prompt photon MC and the fully inclusive background MC. For the prompt photon MC the two methods are less than a factor of 2 apart even for $\Delta r < 1.1$. For $\Delta r < 1.1$ the number of events in the background MC where KTCLUS finds a photon and ELEC5 does not is fairly small. However for $\Delta r < 1.1$ the number of events in the background MC where ELEC5 finds a photon and KTCLUS does not is fairly large. The large decrease in background events with a small decrease in prompt photon events means that KTCLUS will provide a higher purity for $\Delta r < 1.1$. This also means that ELEC5 will provide a higher efficiency for $\Delta r < 1.1$.

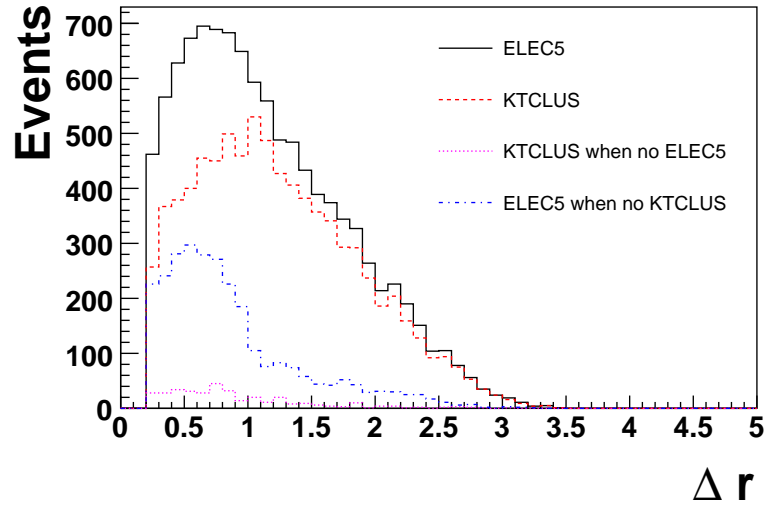


Figure 6.1: The distance, Δr (radians), between a photon candidate and the closest track for the prompt photon in DIS MC. “ELEC5 when no KTCLUS” corresponds to the subset of “ELEC5” events where ELEC5 finds a photon and KTCLUS does not. “KTCLUS when no ELEC5” corresponds to the subset of “KTCLUS” events where KTCLUS finds a photon and ELEC5 does not.

6.4 Photon Energy Corrections

The energy of a photon measured by the ZEUS calorimeter is not the actual energy of the photons. This is predominately due to energy loss in inactive material in front of the calorimeter. The energy of the photon candidate is corrected using a combination of a dead material map, the barrel preshower signal and a non-uniformity correction. The corrected energy is the product of the uncorrected energy and the correction factors given by, $E_{corrected} = \prod_i C_i E_{uncorrected}$ where C_i are the correction factors. The correction factors applied to the data are shown in Fig. 6.3. In general the correction factors are small and close to one.

The resulting energy correction can be examined by comparing generated Monte

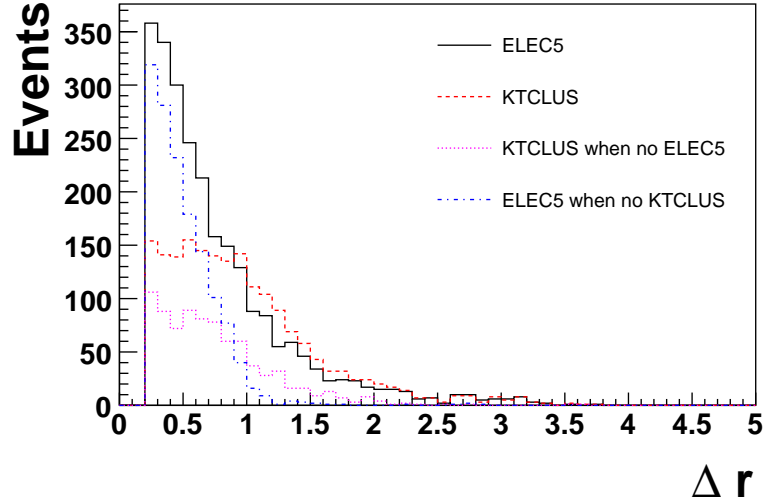


Figure 6.2: The distance, Δr (radians), between a photon candidate and the closest track for the fully inclusive background MC. “ELEC5 when no KTCLUS” corresponds to the subset of “ELEC5” events where ELEC5 finds a photon and KTCLUS does not. “KTCLUS when no ELEC5” corresponds to the subset of “KTCLUS” events where KTCLUS finds a photon and ELEC5 does not.

Carlo energies to the reconstructed energies after a full detector simulation. The transverse energy resolution is defined as the difference between the true transverse energy and the reconstructed transverse energy over the true transverse energy,

$$\text{Resolution} = \frac{E_{T,true}^{\gamma} - E_{T,reconstructed}^{\gamma}}{E_{T,true}^{\gamma}} \quad (6.4)$$

6.5 f_{max}

To evaluate the likelihood that a particular photon candidate is a photon, several variables are used. The first, f_{max} , is the ratio of the photon candidate’s energy in the most energetic cell to the total energy of the photon candidate as defined in Equation

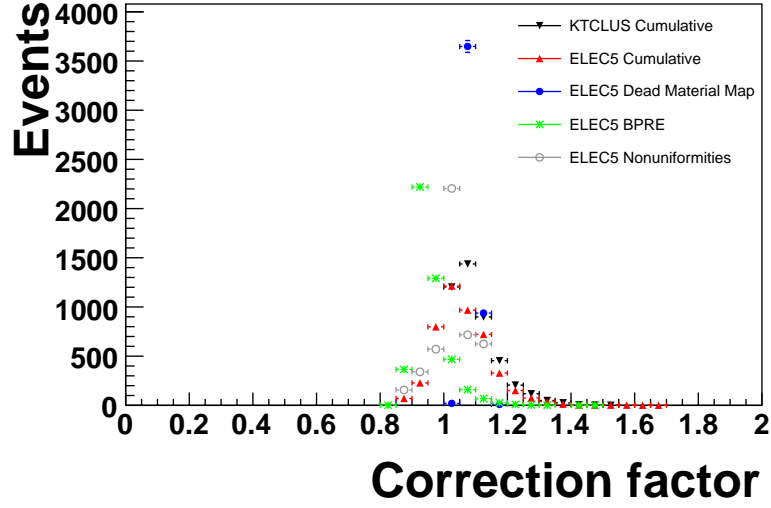


Figure 6.3: Correction factors for KTCLUS and ELEC5 from 2004/2005 e^- running period calculated using the dead material map, non-uniformities and BPRE.

6.5. A single photon is expected to have an f_{max} near 1. However if a photon enters the calorimeter near the edge of a cell, it may deposit more of its energy into an adjoining cell and its f_{max} may drop as low as 0.5. In contrast to single photons the wider energy deposit from a neutral meson will tend to have lower values of f_{max} .

$$f_{max} = \frac{\text{Energy in most energetic cell}}{\text{Total energy in cluster}} \quad (6.5)$$

6.6 $\langle \delta z \rangle$

The second variable that utilizes the transverse shape of the photon candidate is $\langle \delta z \rangle$. $\langle \delta z \rangle$ is the energy-weighted spread of the cluster in the \hat{z} direction and is given by,

$$\langle \delta z \rangle = \frac{\sum (E_{cell} |z_{cell} - \bar{z}|)}{\sum E_{cell}} \quad (6.6)$$

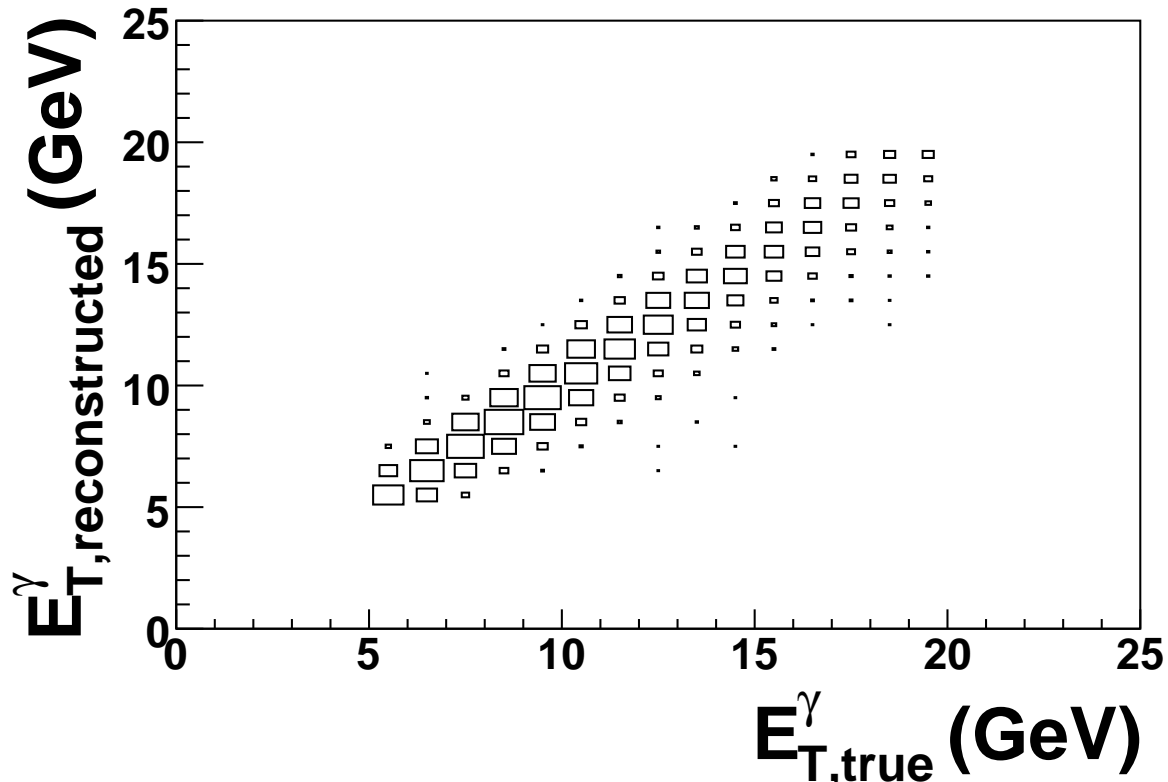


Figure 6.4: Correlation between the detector and hadron levels for E_T^γ when the photon is reconstructed using the ELEC5 photon finder.

A single photon is expected to have a low value of $\langle\delta z\rangle$. As a photon enters the calorimeter near the edge of a cell it is expected to deposit more of its energy into the adjoining cell, and its $\langle\delta z\rangle$ is expected to rise. In contrast to single photons the wider energy deposit from a neutral meson will tend to have higher values of $\langle\delta z\rangle$.

6.7 Barrel Preshower Detector (BPRES)

As was previously mentioned, in addition to information about the transverse shape of the photon candidate we also have some information about its showering before it reaches the barrel calorimeter. The barrel preshower detector counts the

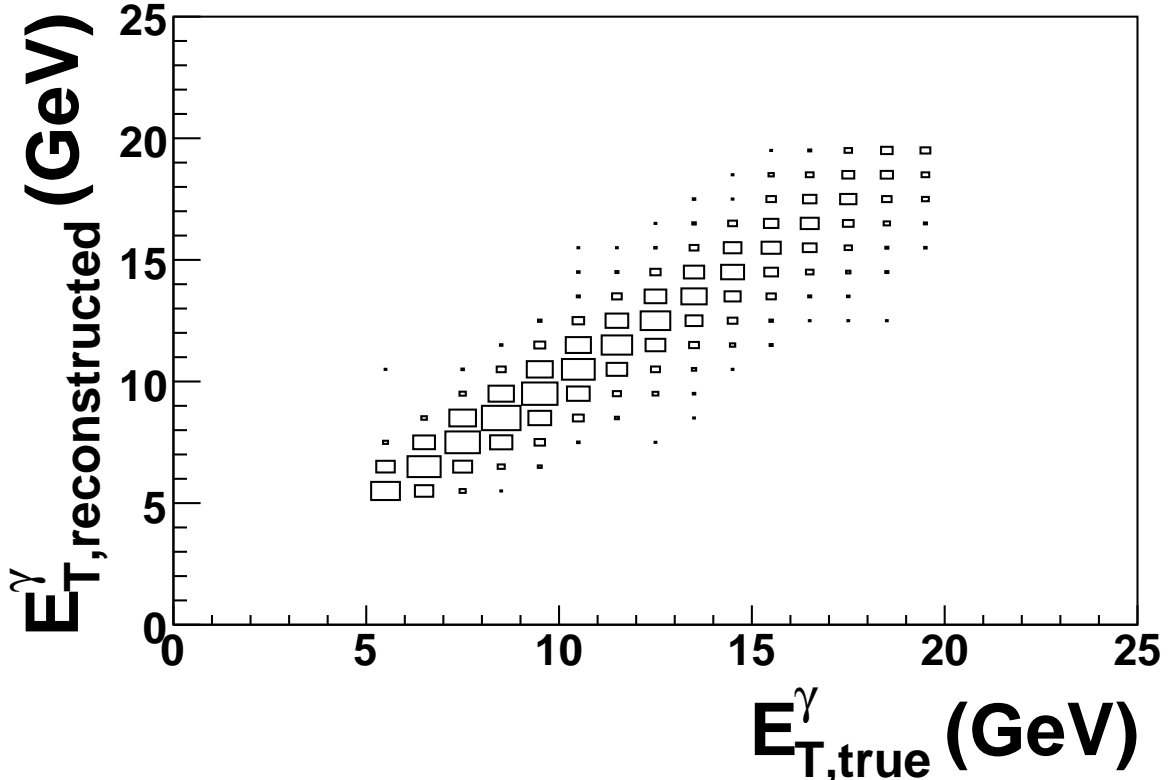


Figure 6.5: Correlation between the detector and hadron levels for E_T^γ when the photon is reconstructed using the KTCLUS photon finder.

number of charged particles that pass through it. Multiple photons originating from the decay of a neutral meson will have a higher probability of converting into at least one e^+e^- pair and will therefore tend to deposit more energy in the barrel preshower detector. This method is sometimes referred to as the conversion-probability method because of its sensitivity to the probability for a photon to convert.

π^0 particles have a lifetime of $8.4 \pm 0.6 \times 10^{-17} s$. [11] therefore they decay long before reaching the detector. It was found that single photons convert into an e^+e^- pair $\sim 60\%$ of the time [10]. A π^0 particle should decay into at least one e^+e^- pair about $(1 - (1 - 0.6)^2) = 84\%$ of the time. So a π^0 particle will deposit no energy in the

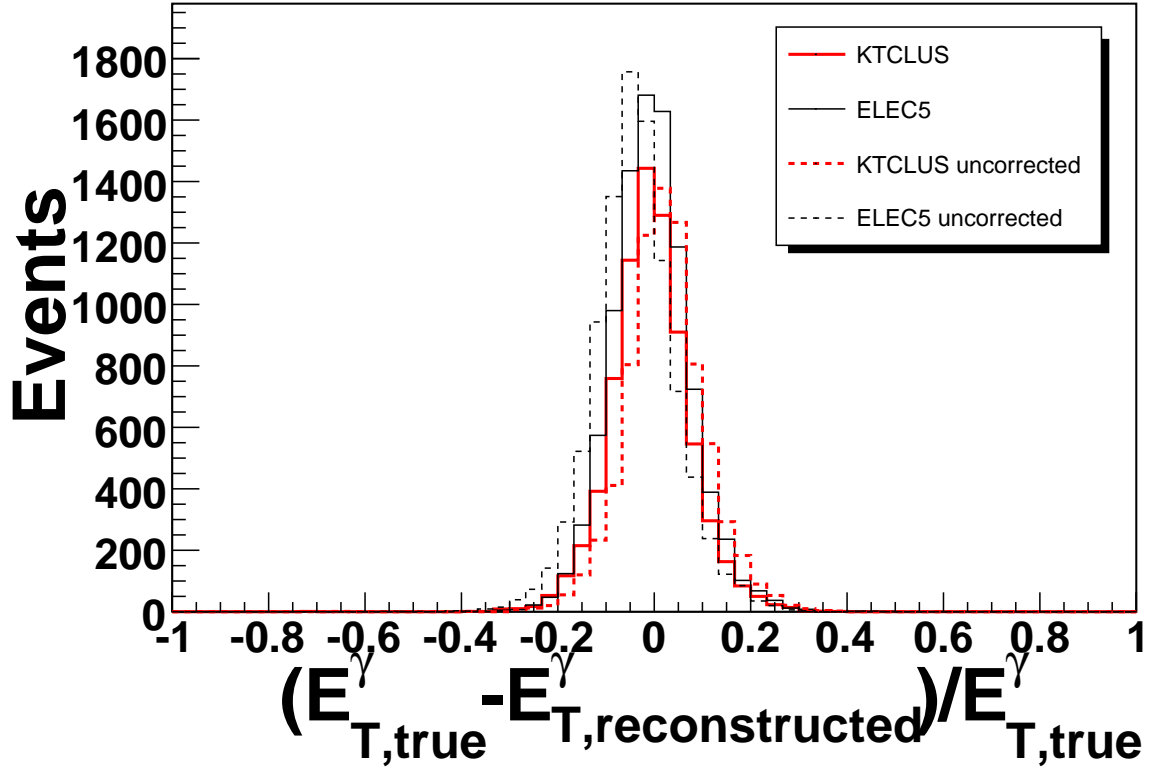


Figure 6.6: E_T^γ resolution before and after energy corrections.

BPRE 16% of the time compared to only 40% of the time for photons. In addition the probability of a π^0 particle to form two e^+e^- pairs is $(0.6)^2 = 36\%$ higher compared a single photon.

6.8 Methods of photon identification using Shower Shapes and BPRE

f_{max} , $\langle \delta z \rangle$ and BPRE all have their relative strengths and weaknesses. No method, or combination of methods, can tell definitively if any given specific photon candidate is a photon. For example if a π^0 decays into two photons and neither of them undergoes preshowering then they will not deposit any energy into the BPRE,

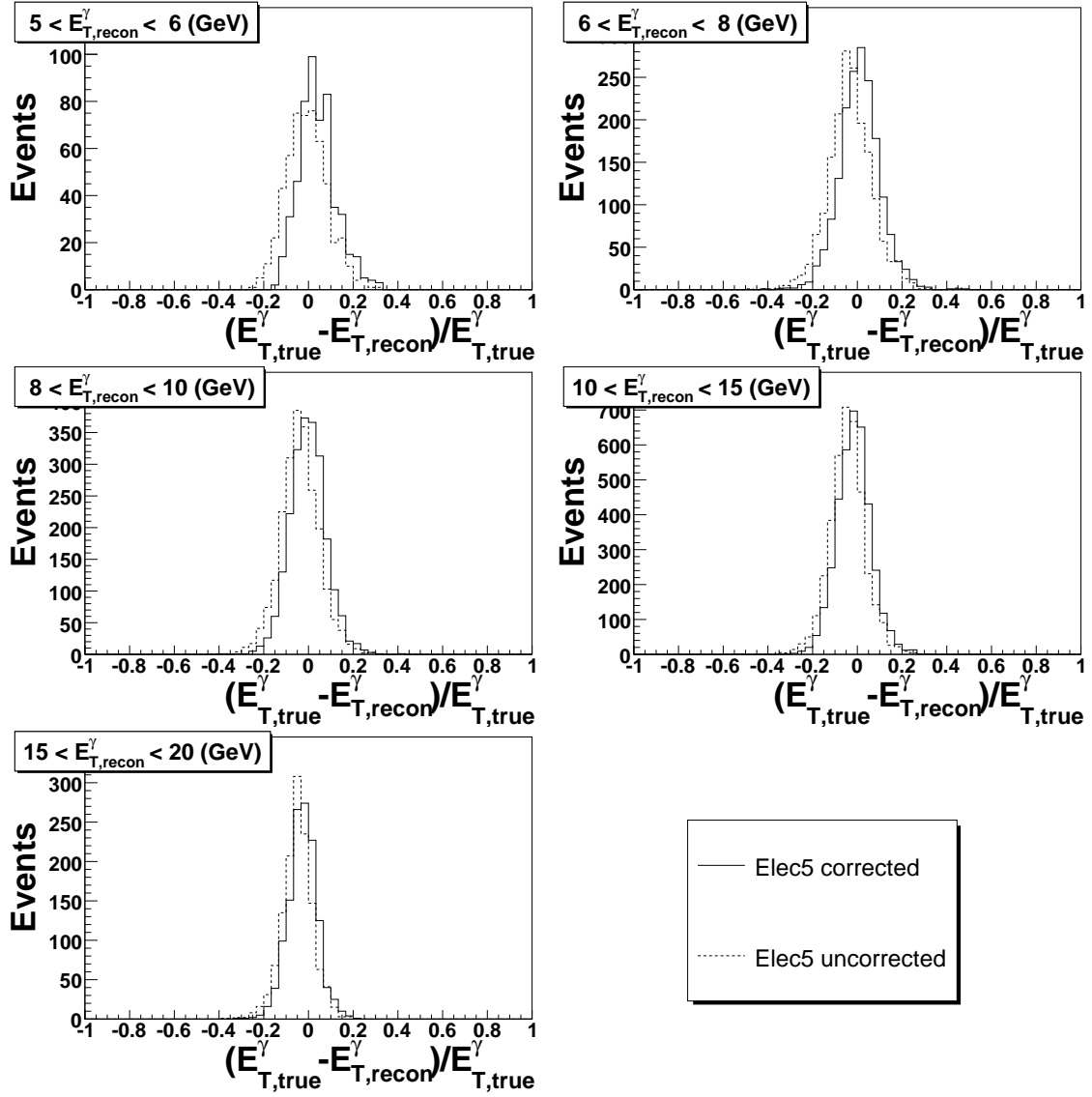


Figure 6.7: E_T^γ resolution in several ranges of $E_{T,reconstructed}^\gamma$ before and after energy corrections when the photon is reconstructed using the ELEC5 photon finder.

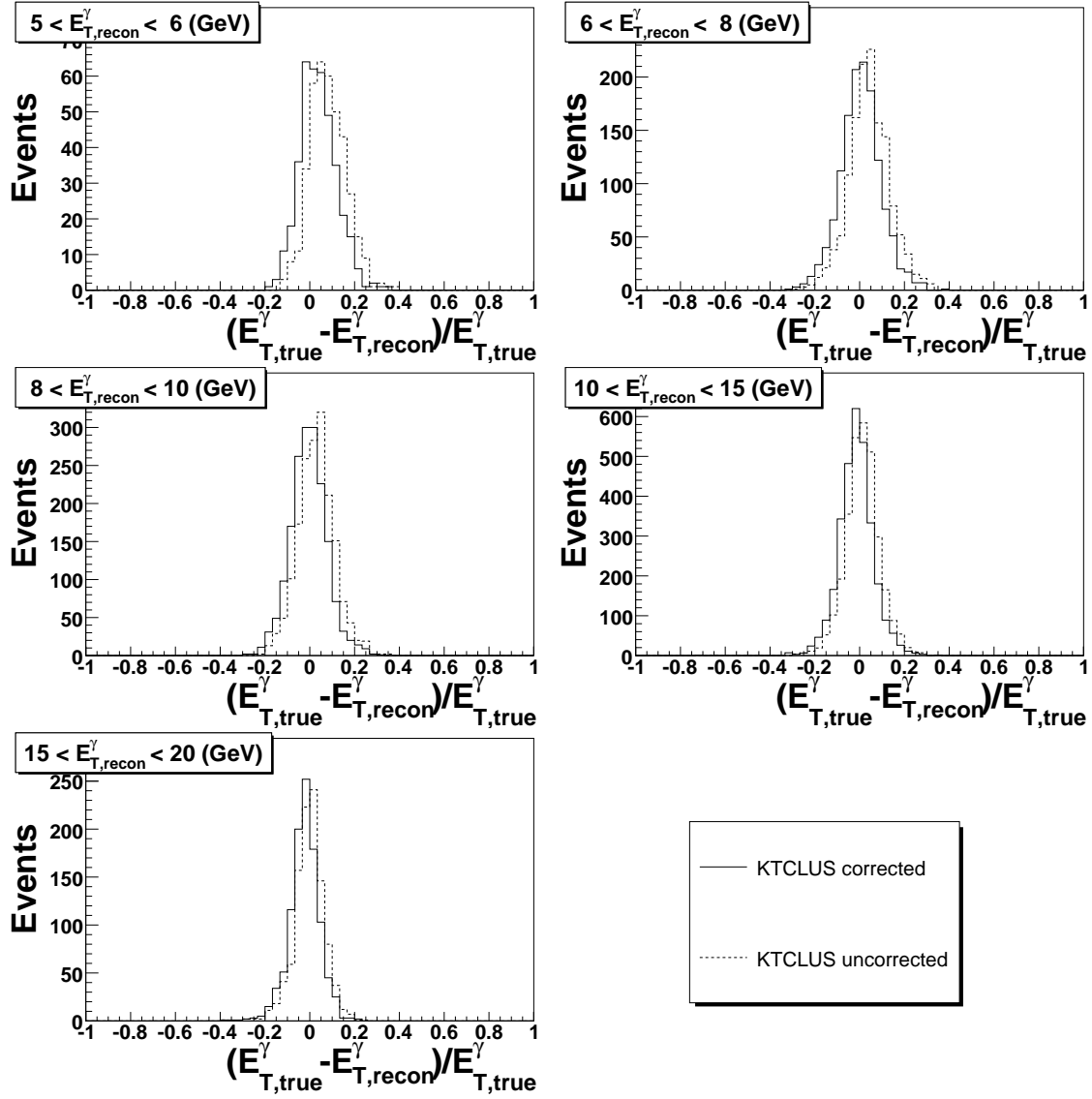


Figure 6.8: E_T^γ resolution in several ranges of $E_{T,reconstructed}^\gamma$ before and after energy corrections when the photon is reconstructed using the KTCLUS photon finder.

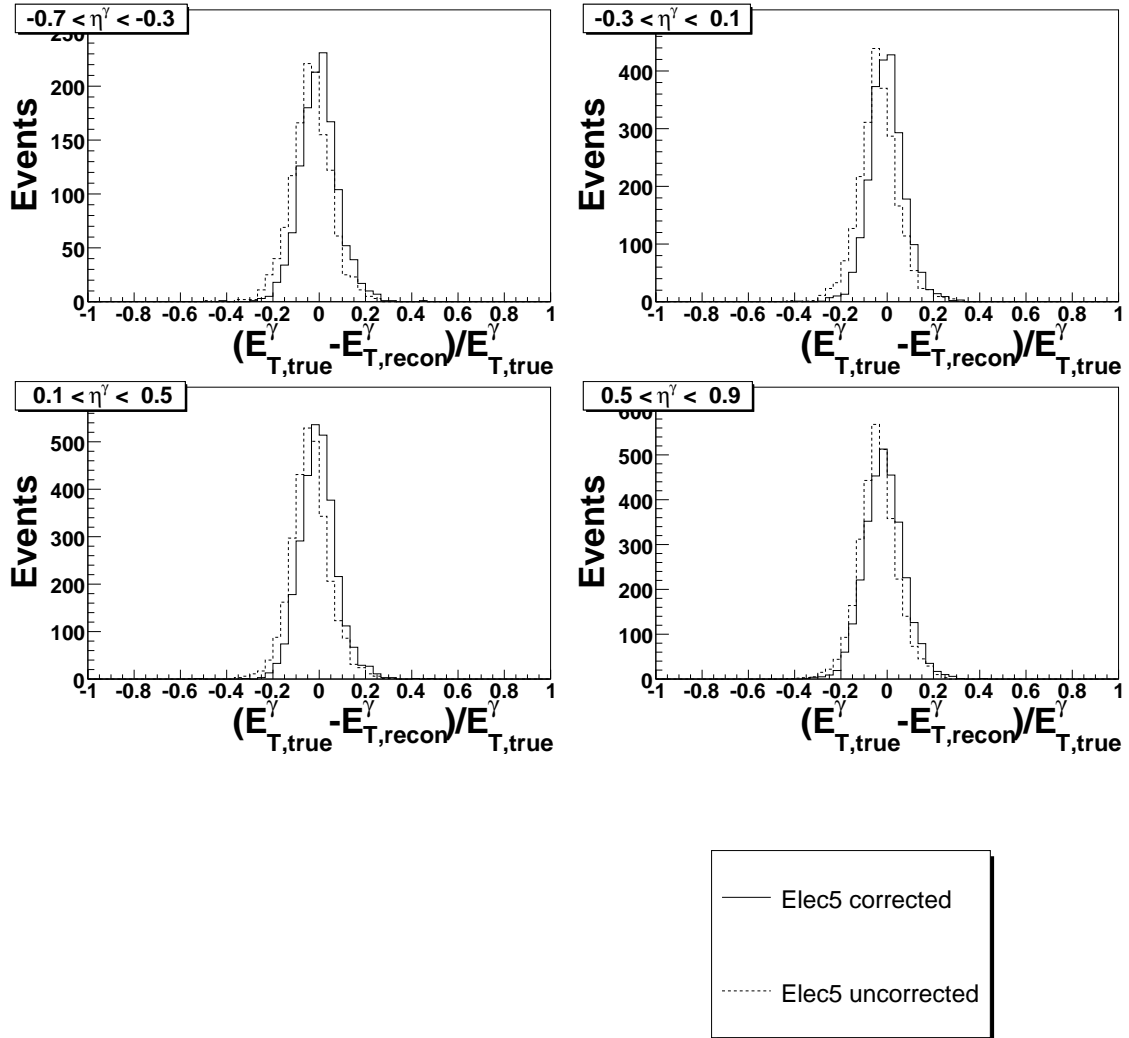


Figure 6.9: E_T^γ resolution in several ranges of η^γ before and after energy corrections when the photon is reconstructed using the ELEC5 photon finder.

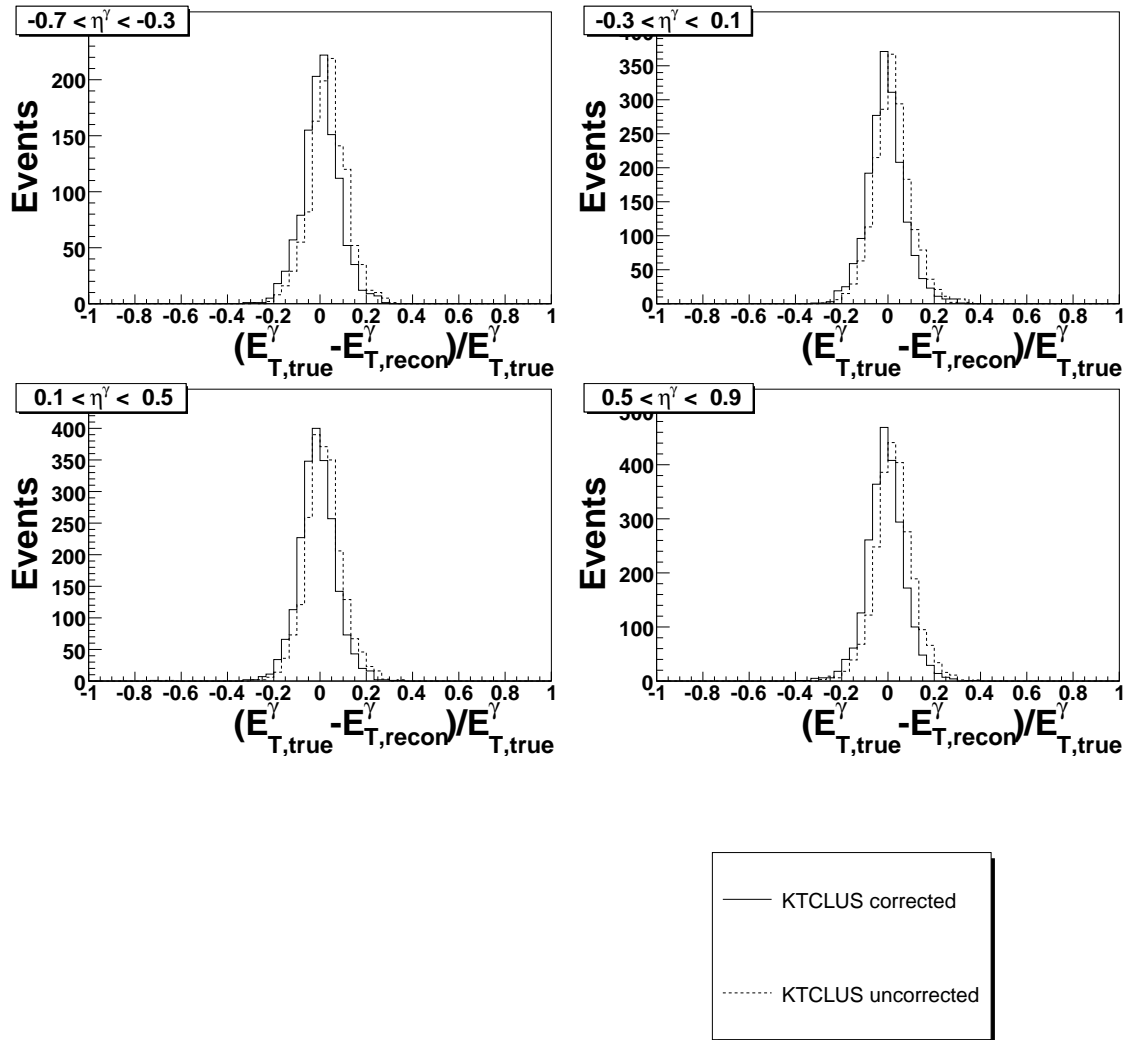


Figure 6.10: E_T^{γ} resolution in several ranges of η^{γ} before and after energy corrections when the photon is reconstructed using the KTCLUS photon finder.

making the π^0 look more like a photon. In Figure 6.11 a small cross section of the BCAL is shown. Several of the EMC cells are labeled A-F. If a photon candidate deposited 9 GeV in cell A and 1 GeV in cell B, it would have an $f_{max} = 0.9$ and a $\langle\delta z\rangle \approx 0.18$ cells wide. However if a photon candidate deposited 9 GeV in cell A and 1 GeV in cell D, it would have an $f_{max} = 0.9$ and a $\langle\delta z\rangle \approx 0.5$ cells wide. In both cases the f_{max} values would be the same. However the $\langle\delta z\rangle$ values are very different. For the latter case which shower shape describes it better? On one hand most of its energy is very well concentrated. On the other hand it is more spread out compared to the first case.

The Deeply Virtual Compton Scattering (DVCS) study shown in Chapter 7 establishes that each method used individually will provide a reliable method of evaluating a photon candidate. However a combination of methods could be used to fully capitalize on each method's individual strengths. One way to accomplish this is the construction of a neural network based on the photon candidate's shower shapes and BPRE energy deposit. The neural network would need to be trained on several large single particle MC samples. The relative contribution from each type of neutral meson can be taken from the PYTHIA and HERWIG MC generators. Once trained, the neural network should operate with a high efficiency and purity. The validity of the neural network could be confirmed via study of DVCS photons.

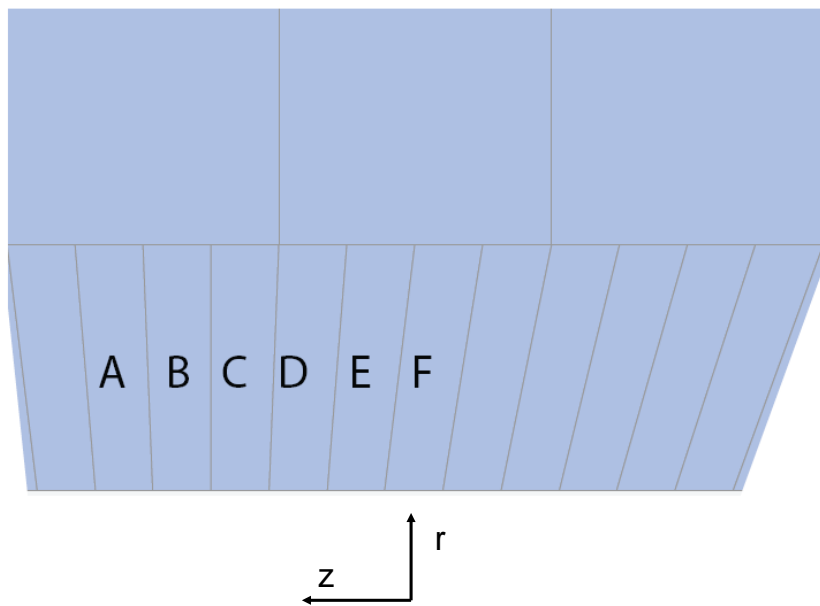


Figure 6.11: Diagram of the BCAL showing the \hat{Z} and \hat{R} axes. The front of the EMC cells are 5 cm in the z direction

Chapter 7

Deeply Virtual Compton Scattering

Studies

The ability to differentiate between photons and background due to neutral mesons is of vital importance to any prompt photon analysis. This has traditionally been done via the analysis of shower shapes, f_{max} and $\langle\delta z\rangle$. Another complementary way of doing this is the aforementioned conversion probability method. Before any analysis using shower shapes or the conversion probability method is performed it must be verified by comparison with data that the different variables are correctly described in the MC simulations. This can be done with photons originating from Deeply Virtual Compton Scattering (DVCS) [61] events.

7.1 Introduction to DVCS

Deeply Virtual Compton Scattering is a diffractive process, i.e. there is a large rapidity gap between the proton remnant and the photon where there is no activity. This leads to a well isolated final state photon. If we restrict the study to events where the rapidity gap is vary large then the proton remnant entirely escapes down

the beampipe. The lack of hadronic activity inhibits the production of neutral mesons and ensures a highly pure sample of high- E_T photons.

DVCS has an identical final state to the Bethe-Heitler (BH) process, see Figures 7.2b and 7.2c. Being a purely electromagnetic process the BH process will only introduce photons, therefore there is no need to remove it from the event sample.

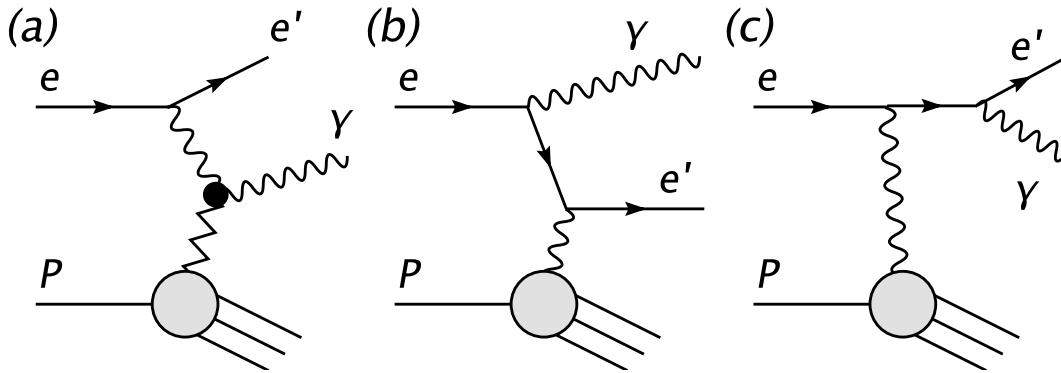


Figure 7.1: Diagram of the DVCS (a) and BH processes (b),(c).

7.2 Event Selection

There are several important differences between the event selection of a prompt photon sample and a DVCS sample. The foremost being that, for the DVCS sample events with two isolated electromagnetic clusters and at most one track were pre-selected. If there was a track in the event it was required that it be associated with the scattered lepton. As with prompt photons in DIS the scattered lepton was required to be in the RCAL, which restricted the scattered lepton to a pseudorapidity of $-1.0 < \eta_{e'} < -2.6$. The minimum energy of the scattered lepton for the DVCS sample was raised from $E_{e'} > 10$ GeV to $E_{e'} > 15$ GeV. The Q^2 limit was also lowered from $Q^2 > 35$ GeV² to $Q^2 > 10$ GeV². The same box cut was used for the scattered lepton

as was used for the prompt photon selection. If an event vertex could be reconstructed it was required to be $|Z_{vertex}| < 40cm$.

To ensure that photons were selected with similar kinematics to the prompt photons in DIS sample the same requirements were placed of the photon candidate as defined in chapter 6.1. As with prompt photons in DIS the photon candidate was reconstructed with either the ELEC5 or KTCLUS photon finder.

With DVCS being a diffractive process, it should be required that there be no other activity in the calorimeter. Therefore events were selected where the total calorimeter energy not associated with the scattered lepton or within a cone in $\eta \times \phi$ of 1.0 radian centered on the photon candidate was less than 0.5 GeV. Since the scattered lepton is restricted to the RCAL and the photon candidate to the BCAL it was also required that the total energy in the FCAL be less than 1.0 GeV. Both leptons and photons are expected to deposit most, if not all, of their energy in the electromagnetic sections of the calorimeter so it was required that the energy in the BCAL hadronic or RCAL hadronic sections be less than 1.0 GeV each.

7.3 DVCS Simulation

The MC simulation of the DVCS process was carried out with the GenDVCS [62] event generator, which is based on the Frankfurt, Freund and Strikman (FFS) [63] model. The FFS model calculates the DVCS scattering amplitude to leading $\alpha_s \ln Q^2$ and is exclusively intended for modeling the small x region. The kinematic region of this is such that DGLAP is valid and the square of the momentum transferred the proton is small. This is consistent with the experimental requirement that there be no calorimeter energy not associated with the scattered lepton or photon.

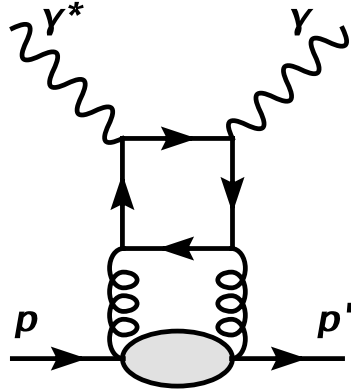


Figure 7.2: Leading contribution to DVCS in the FFS model.

The BH processes were simulated using the GRAPE-Compton [64] generator. The GRAPE-Compton simulation is based on the automatic system GRACE [65] for calculating Feynman diagrams.

When the DVCS cross section is integrated over the e and p scattering planes the interference between the DVCS and BH amplitudes is very small [66, 67]. Thus the DVCS and BH event sample can be treated as a simple sum of the two processes, and may be simulated as the simple sum of the GenDVCS and GRAPE-Compton simulations in a 163:150 combination [61].

7.4 Comparisons

The f_{max} , $\langle \delta z \rangle$ and BPRE distributions of the DVCS photons in data are fairly well described by DVCS MC, see Figures 7.3 and 7.4. As seen in Figure 7.3 and 7.4 there are expected to be very few if any photons with $\langle \delta z \rangle > 0.65$, so it is additionally required that the photon candidate have $\langle \delta z \rangle < 0.65$.

Figure 7.5 is a comparison between DVCS data and DVCS MC for the differences between photons found with both ELEC5 and KTCLUS. For example while both

ELEC5 and KTCLUS associate about the same amount of energy with the photon, KTCLUS tends to associate more BCAL cells with the photon. The addition of more low-energy cells into the reconstruction of the photon causes a larger difference in the description of $\langle \delta z \rangle$ compared to f_{max} .

The opening angle for a neutral meson is expected to be dependent on its energy, as seen in Equation 6.1. For this reason it must be verified that the f_{max} , $\langle \delta z \rangle$ and BPRE distributions are equally well described in different regions of E_T^γ . The comparison between DVCS data and DVCS MC for f_{max} of photons found with ELEC5 (KTCLUS) in different regions of E_T^γ can be seen in Figure 7.8 (7.12), with the DVCS MC normalized the the DVCS data in each plot. There is agreement between the DVCS data and the DVCS MC within the statistics used for each E_T^γ range. A comparison between f_{max} integrated over the entire E_T^γ range shown in Figures 7.6 and 7.7 and the smaller E_T^γ ranges in Figures 7.8 and 7.12 highlights the possible statistical limitations of looking at f_{max} separately for the smaller E_T^γ ranges. The same conclusion can be reached for $\langle \delta z \rangle$ when comparing $\langle \delta z \rangle$ integrated over the entire E_T^γ range shown in Figures 7.6 and 7.7 and the smaller E_T^γ ranges in Figures 7.9 and 7.13. One possible solution to this was used in the previous ZEUS publication [10] where a linear variation between the different ranges of E_T^γ was used. The general shapes of the f_{max} distributions do not change significantly for the different ranges of E_T^γ in Figures 7.9 and 7.13.

The different η regions of the ZEUS detector are expected to have slightly different amounts of dead material in front of the BCAL. This will cause the shower shapes to differ slightly for different η regions of the BCAL. The comparison between DVCS

data and DVCS MC for f_{max} of photons found with ELEC5 (KTCLUS) in different regions of η^γ can be seen in Figure 7.10 (7.14), with the DVCS MC normalized to the DVCS data in each plot. A shift in the position of the peak in Figures 7.10 and 7.14 supports the assumption of extra dead material for the different η ranges. The same can be seen in Figures 7.11 and 7.15, which shows the comparison between DVCS data and DVCS MC for $\langle\delta z\rangle$ in the different η ranges.

The agreement between HERA II DVCS data and GenDVCS MC for the shower shapes, f_{max} and $\langle\delta z\rangle$, is high enough to support their use for photon evaluation in the prompt photon data set. The overall conversion probability determined from the BPRE distribution in the HERA II DVCS data is well reproduced by the GenDVCS MC. The tail of the BPRE distribution is not well reproduced by the GenDVCS MC. There is a systematic shift in the GenDVCS MC towards higher energy deposits. This is expected to cause the use of the BPRE distribution for photon evaluation in the HERA II data set to overestimate the amount of neutral mesons that will be needed to model the data. While the f_{max} , $\langle\delta z\rangle$ and BPRE distributions were tested in the evaluation of HERA II prompt photons only f_{max} and $\langle\delta z\rangle$ provided results that were usable for the reconstruction cross sections.

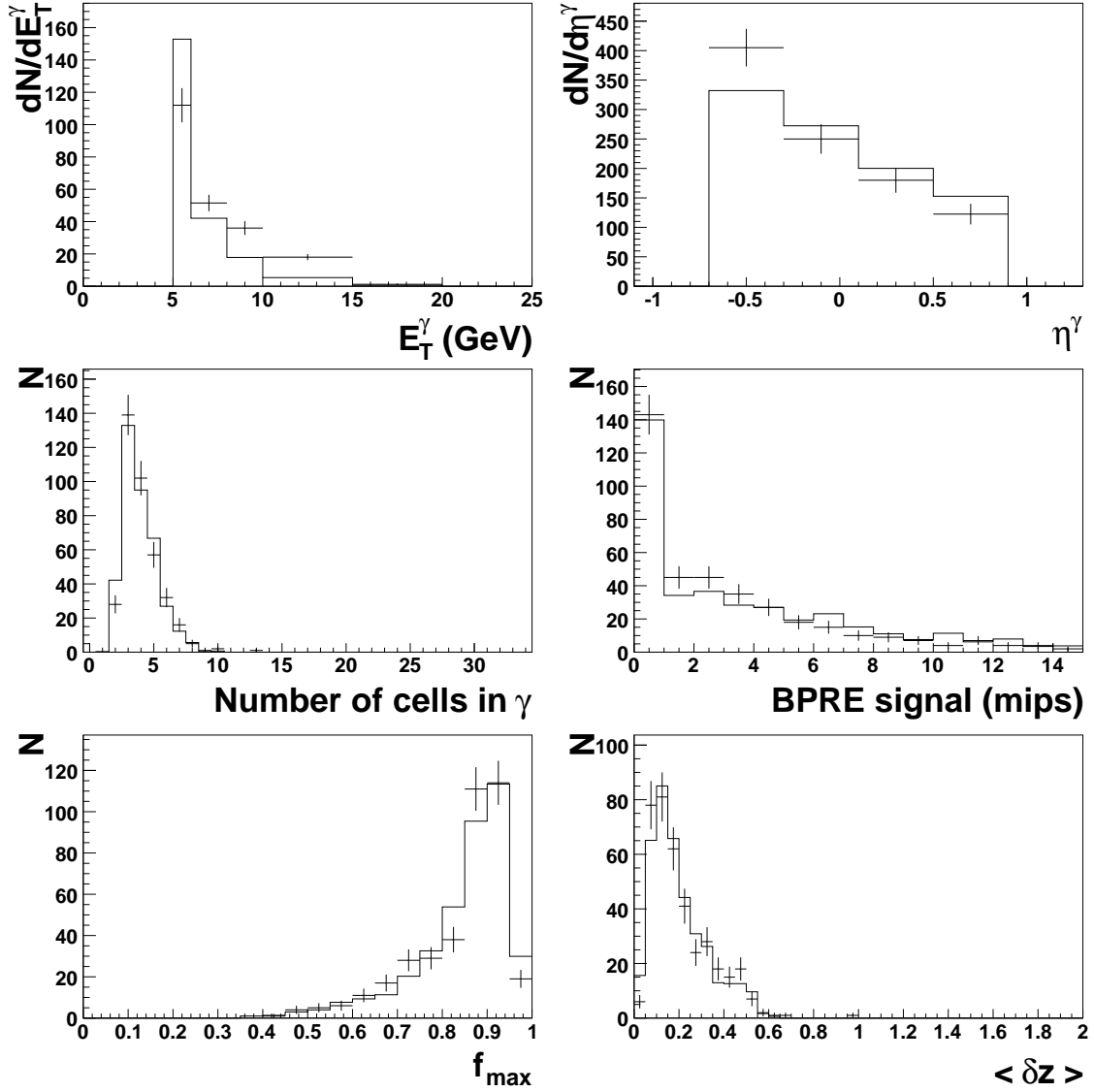


Figure 7.3: DVCS data (crosses) compared to DVCS MC (histogram) for E_T^γ , η^γ , Number of cells in γ , BPRE signal, f_{max} , and $\langle \delta z \rangle$ when the photon was found with ELEC5.

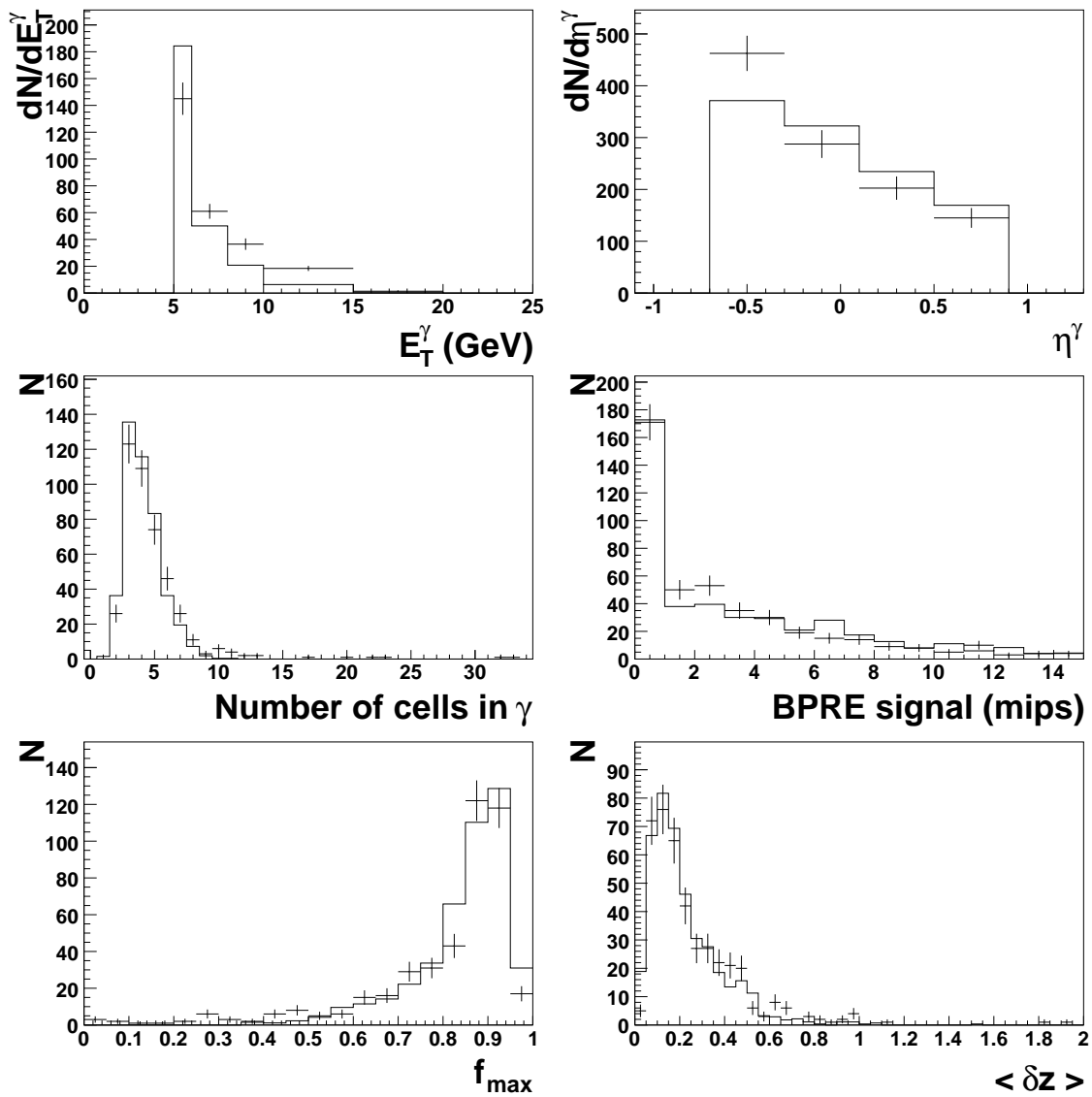


Figure 7.4: DVCS Data (crosses) compared to DVCS MC (histogram) for E_T^γ , η^γ , Number of cells in γ , BPRE signal, f_{max} , and $\langle \delta z \rangle$ when the photon was found with KTCLUS.

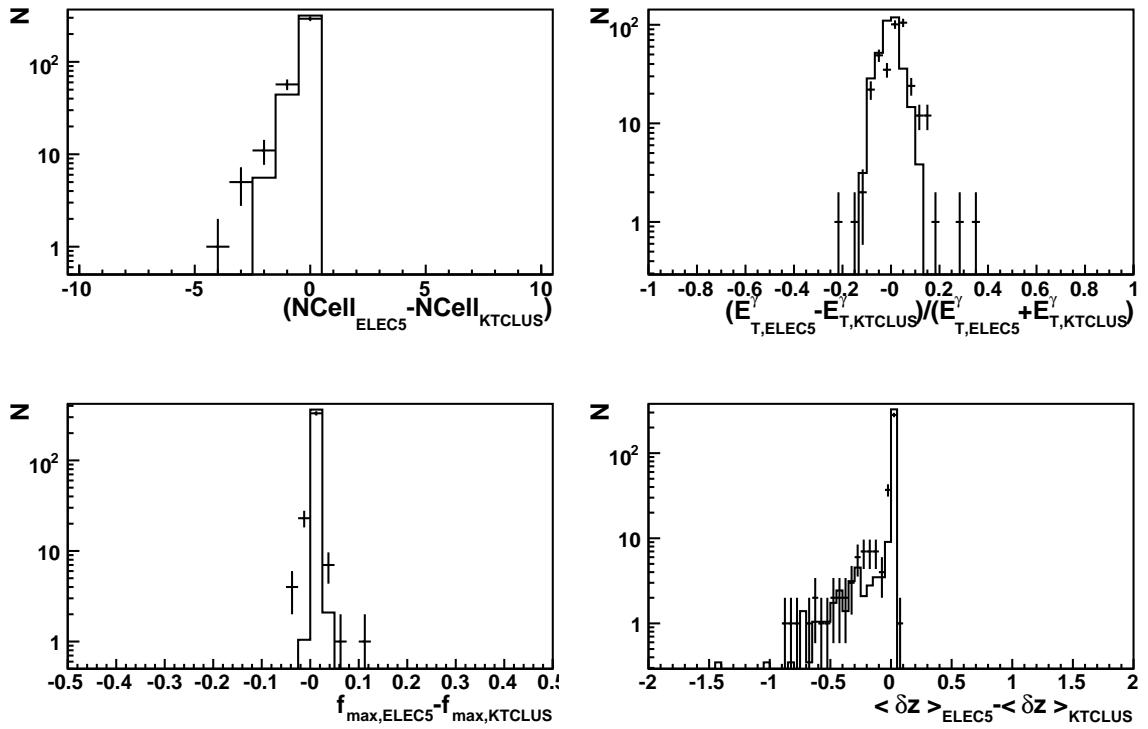


Figure 7.5: DVCS Data (crosses) compared to DVCS MC (histogram) for the comparison of the two photon finders. The differences in the number of cells, E_T^γ , f_{max} , and $\langle \delta z \rangle$ between the two photon finders is shown.

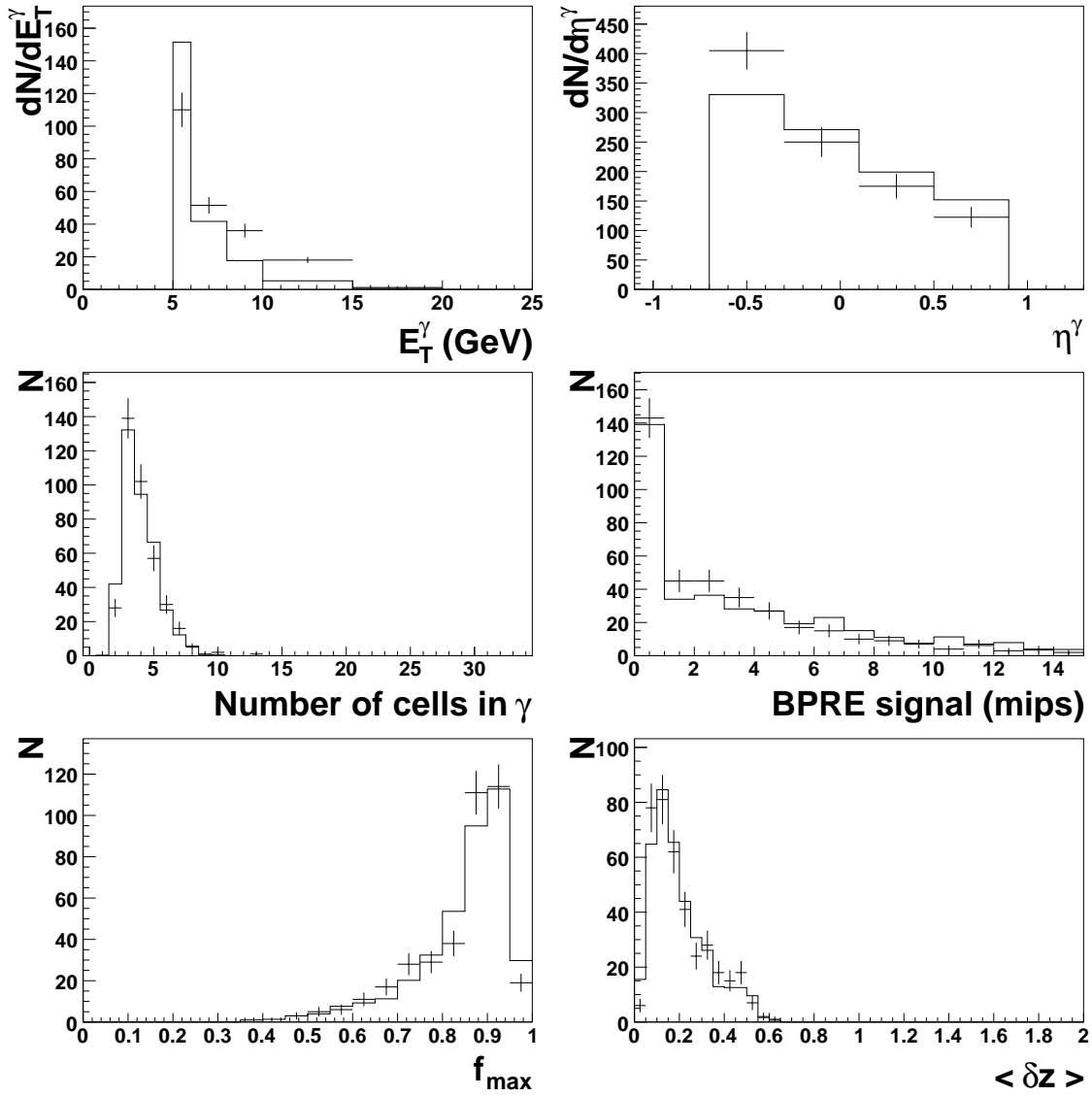


Figure 7.6: DVCS Data (crosses) compared to DVCS MC (histogram) for E_T^γ , η^γ , Number of cells in γ , BPRE signal, f_{max} , and $\langle \delta z \rangle$ when the photon was found with ELEC5 with $\langle \delta z \rangle < 0.65$.

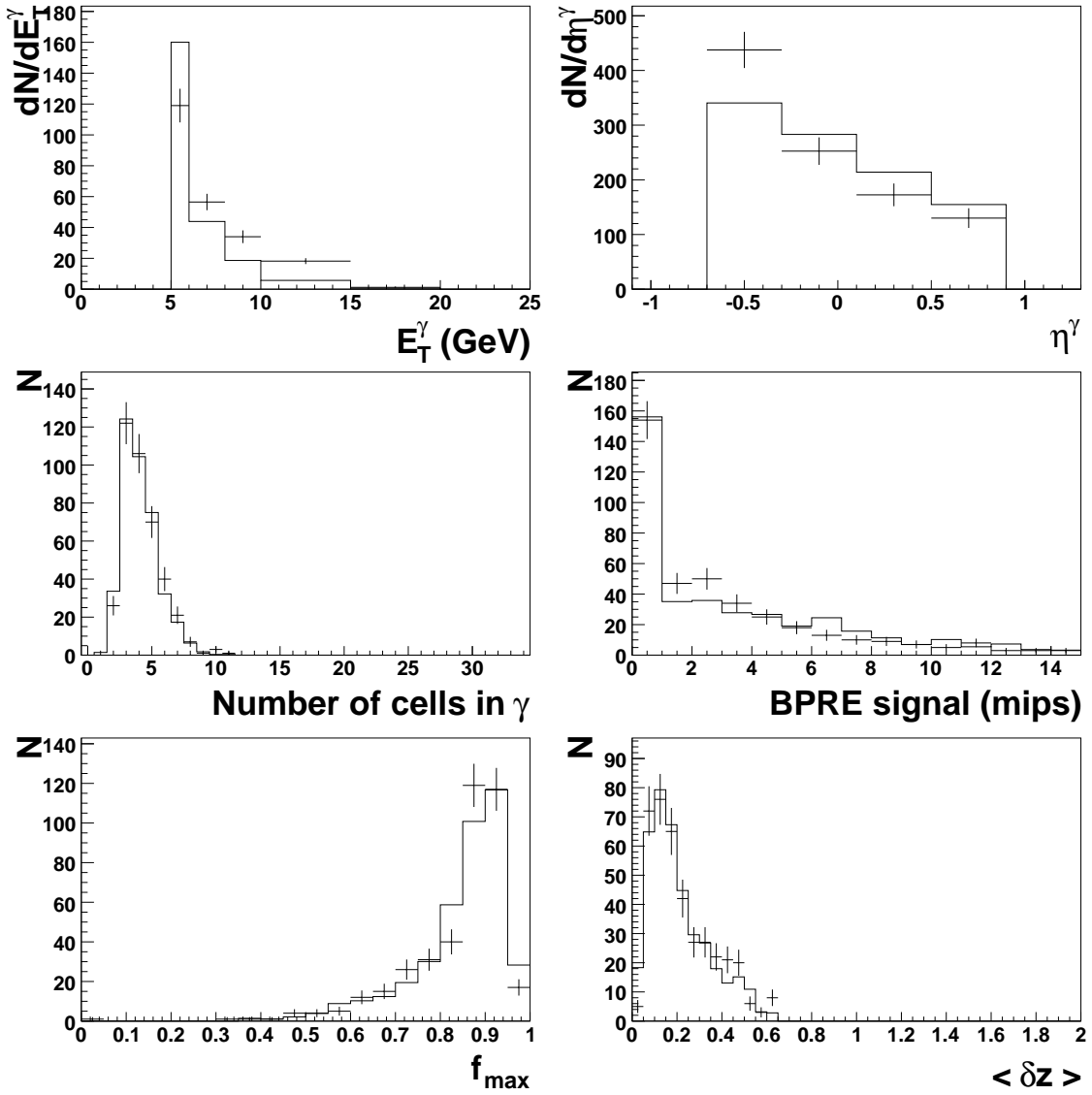


Figure 7.7: DVCS Data (crosses) compared to DVCS MC (histogram) for E_T^γ , η^γ , Number of cells in γ , BPRE signal, f_{max} , and $\langle \delta z \rangle$ when the photon was found with KTCLUS with $\langle \delta z \rangle < 0.65$.

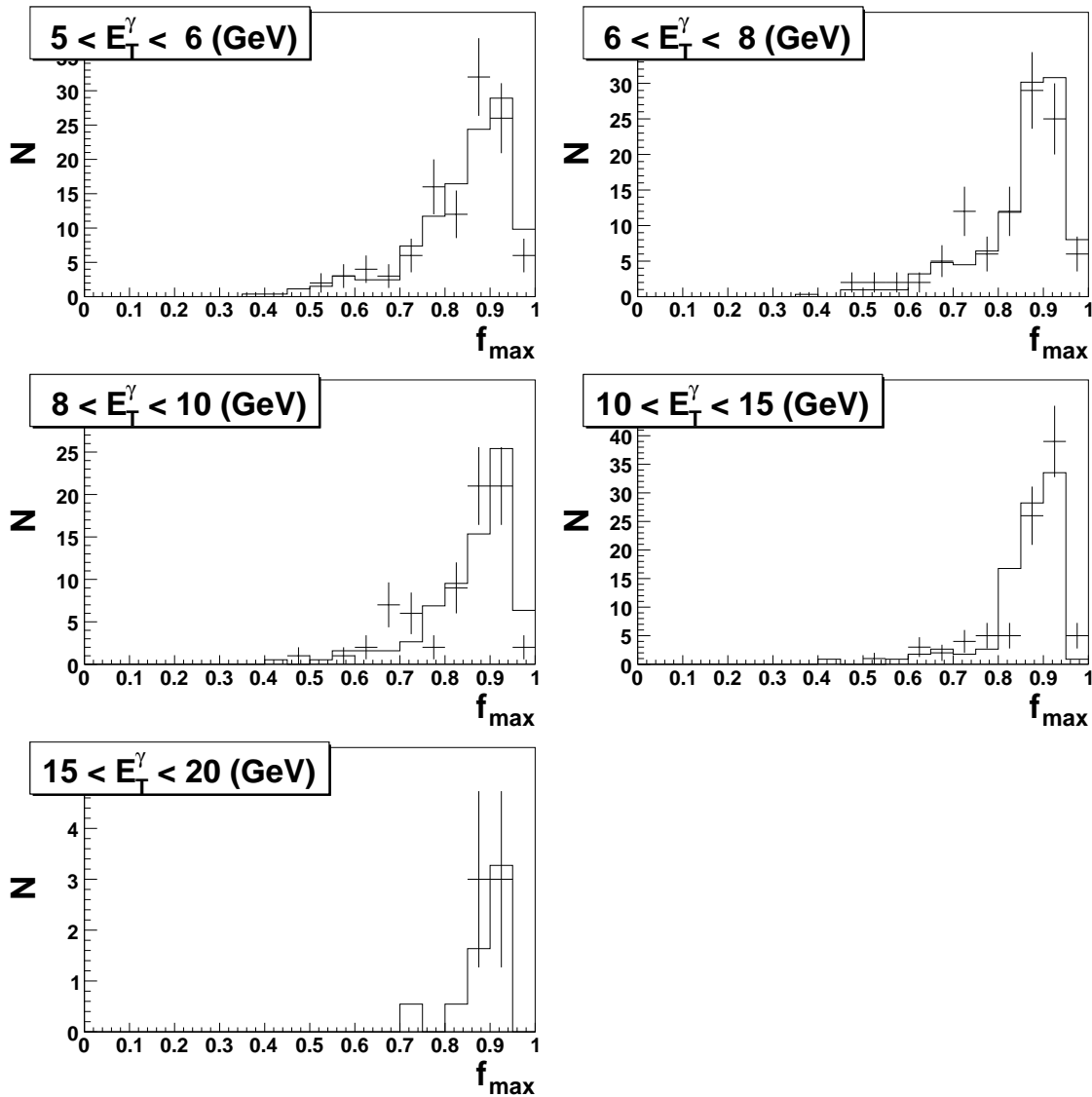


Figure 7.8: DVCS Data (crosses) compared to DVCS MC (histogram) for f_{max} in different regions of E_T^γ when the photon was found with ELEC5 with $\langle \delta z \rangle < 0.65$.

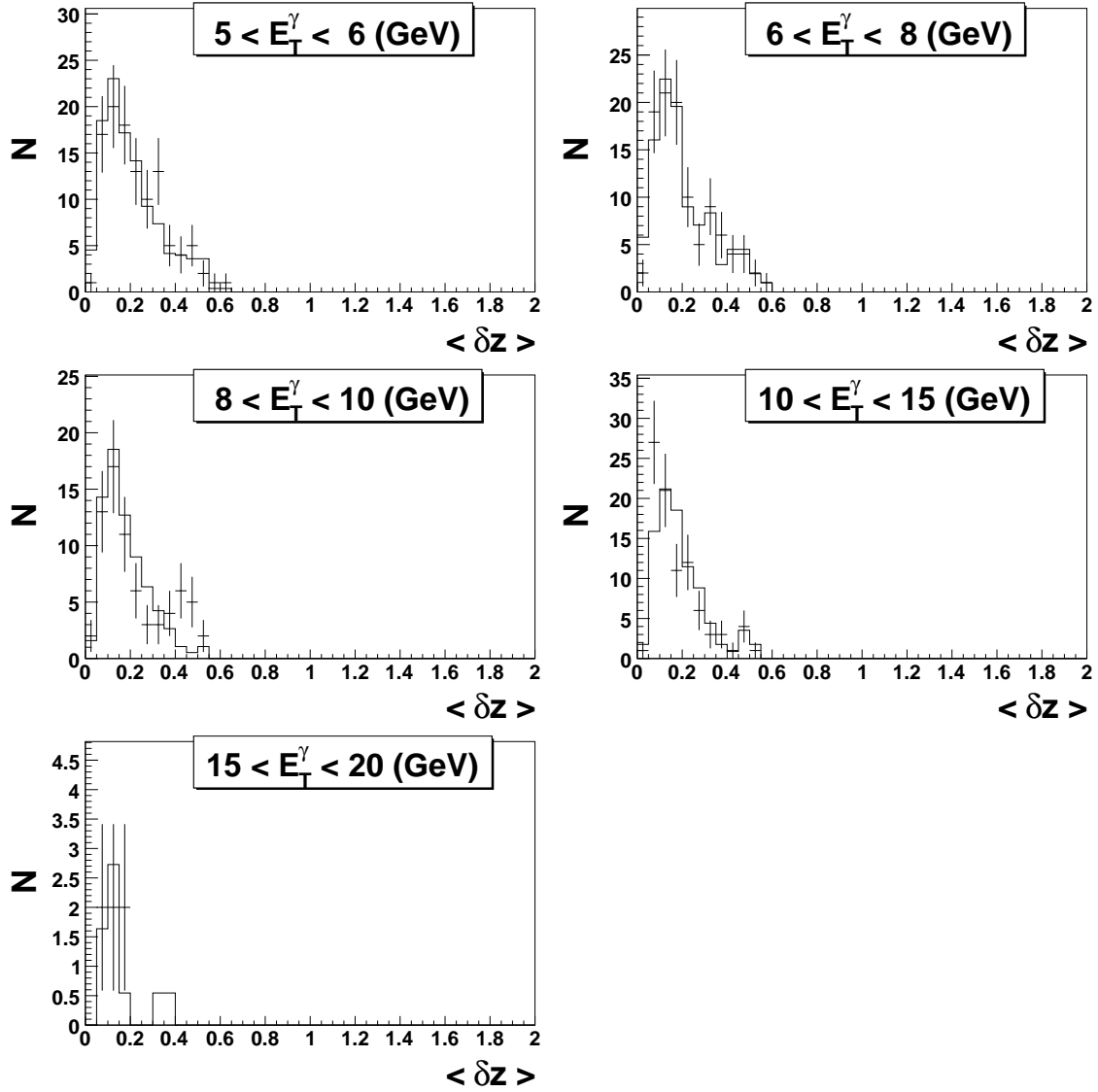


Figure 7.9: DVCS Data (crosses) compared to DVCS MC (histogram) for $\langle \delta z \rangle$ in different regions of E_T^γ when the photon was found with ELEC5 with $\langle \delta z \rangle < 0.65$.

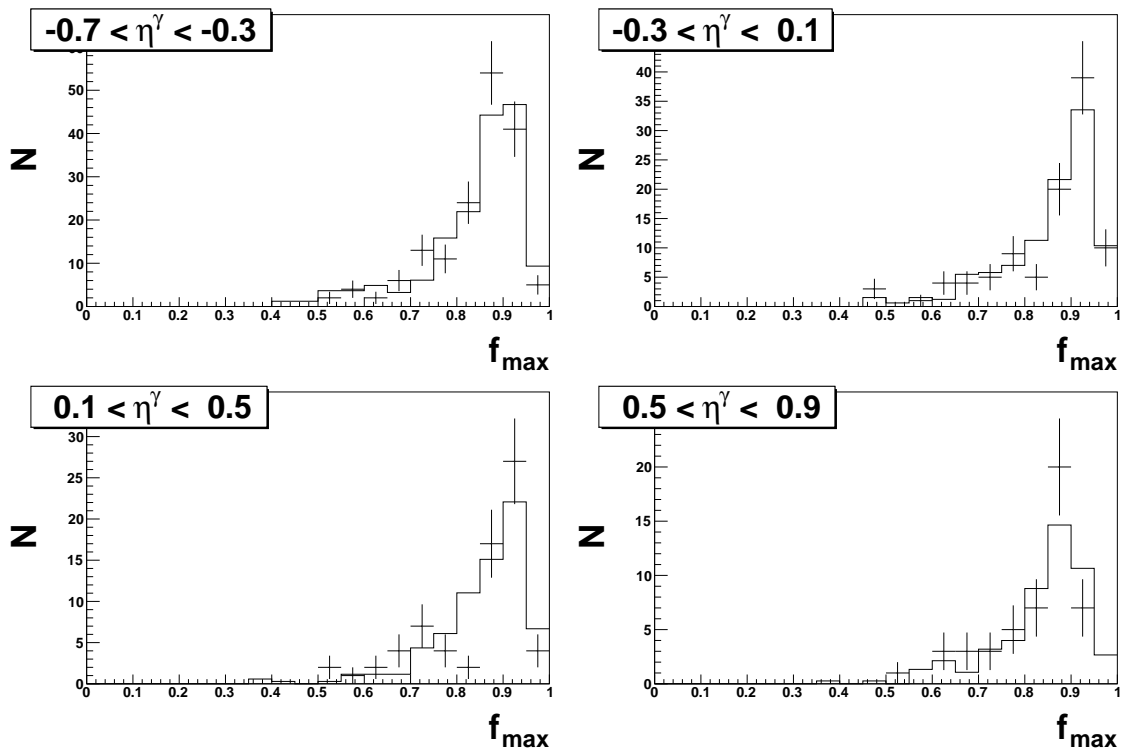


Figure 7.10: DVCS Data (crosses) compared to DVCS MC (histogram) for f_{max} in different regions of η^γ when the photon was found with ELEC5 with $\langle \delta z \rangle < 0.65$.

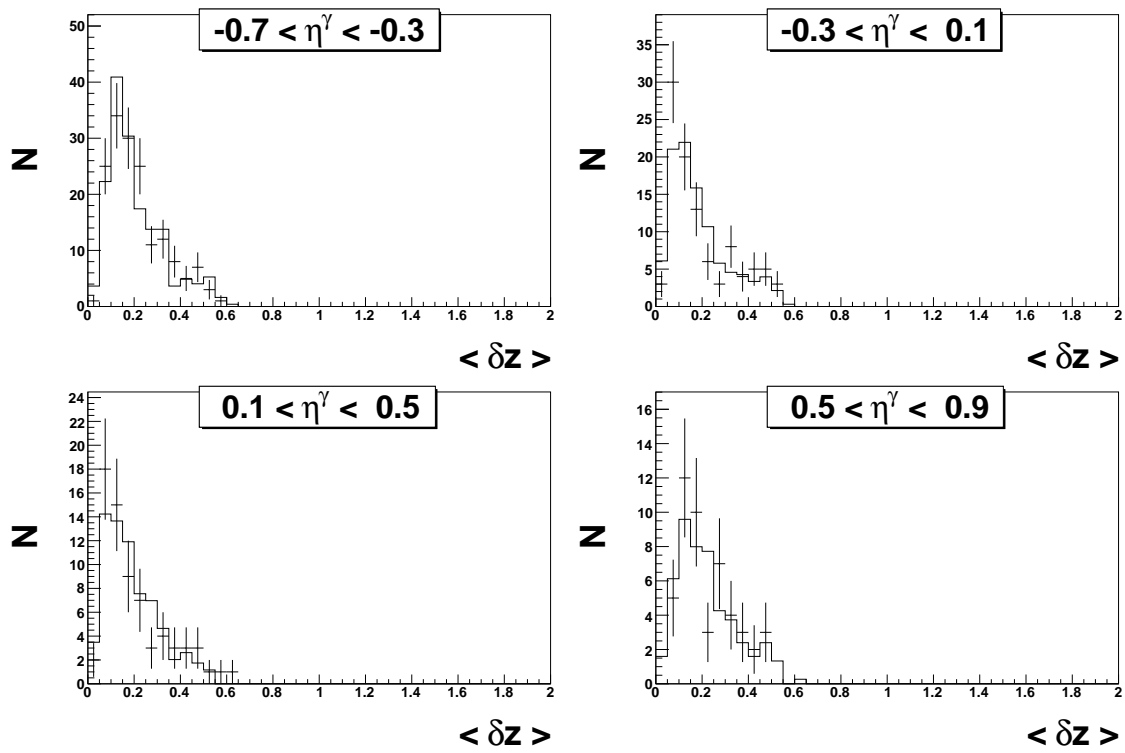


Figure 7.11: DVCS Data (crosses) compared to DVCS MC (histogram) for $\langle \delta z \rangle$ in different regions of η^γ when the photon was found with ELEC5 with $\langle \delta z \rangle < 0.65$.

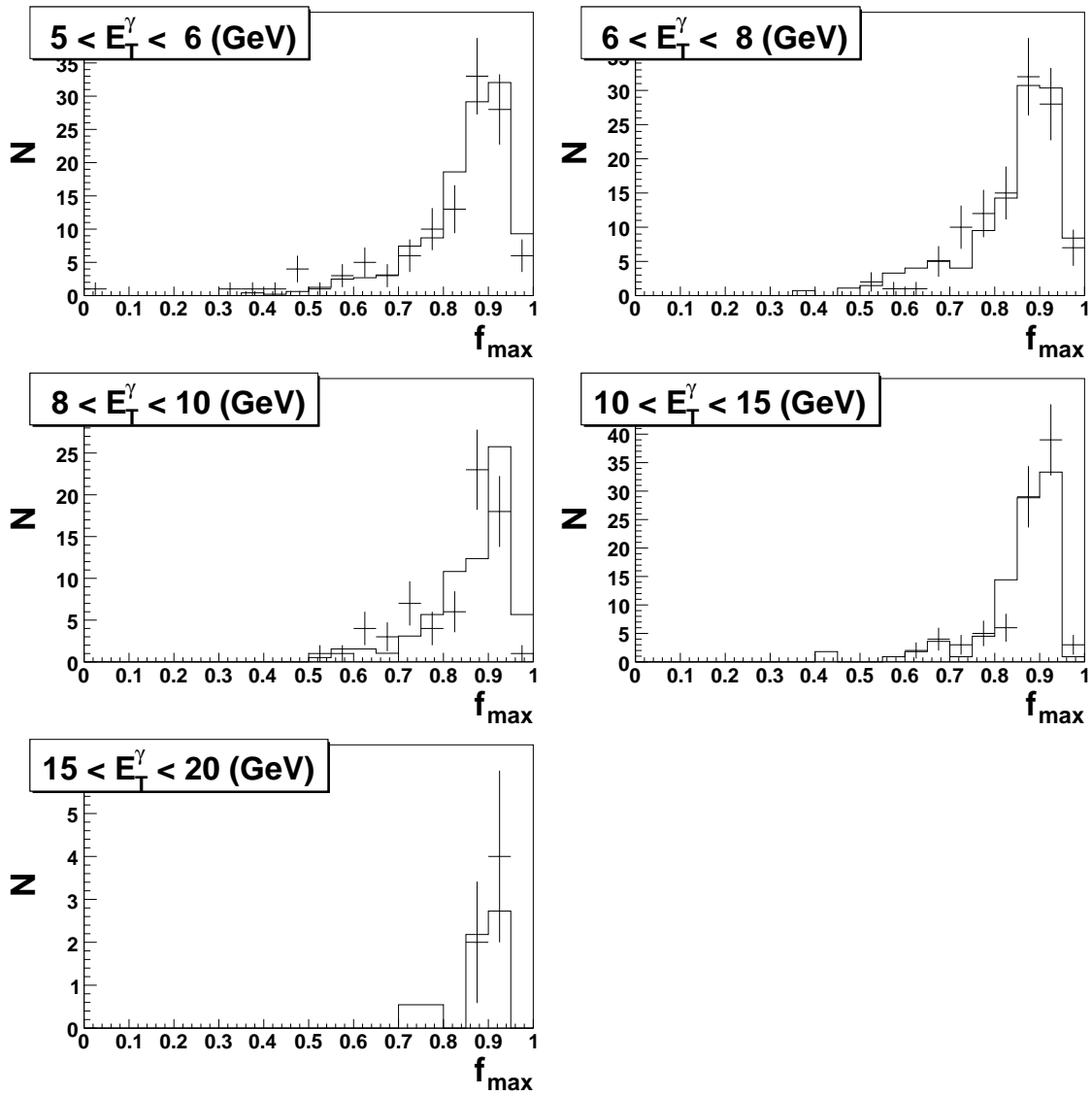


Figure 7.12: DVCS Data (crosses) compared to DVCS MC (histogram) for f_{max} in different regions of E_T^γ when the photon was found with KTCLUS with $\langle \delta z \rangle < 0.65$.

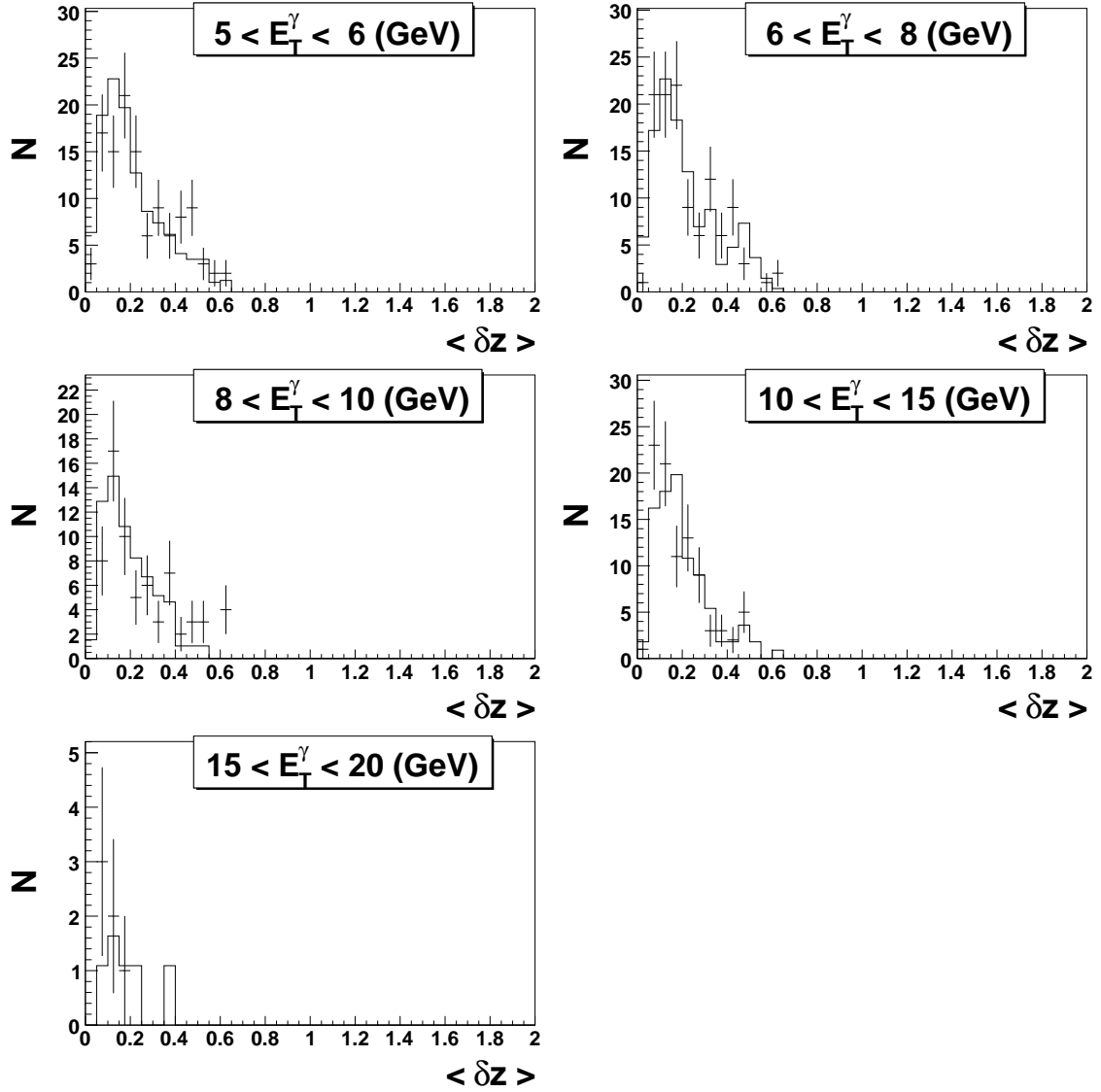


Figure 7.13: DVCS Data (crosses) compared to DVCS MC (histogram) for $\langle \delta z \rangle$ in different regions of E_T^γ when the photon was found with KTCLUS with $\langle \delta z \rangle < 0.65$.

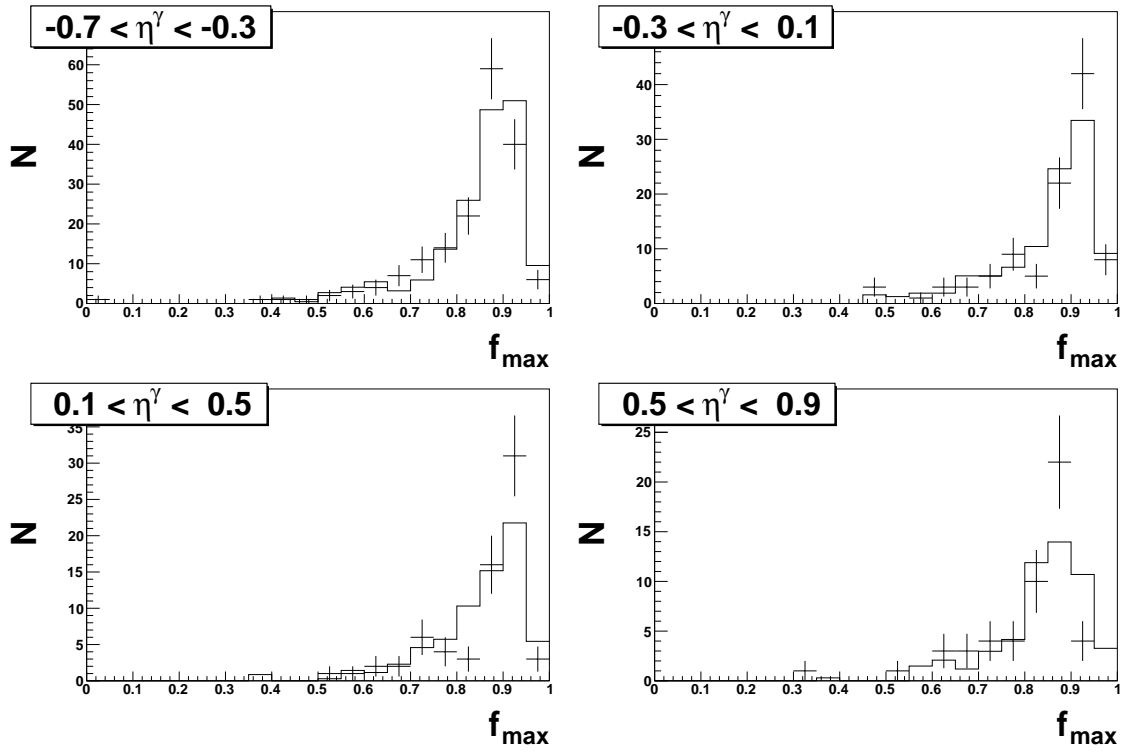


Figure 7.14: DVCS Data (crosses) compared to DVCS MC (histogram) for f_{max} in different regions of η^γ when the photon was found with KTCLUS with $\langle \delta z \rangle < 0.65$.

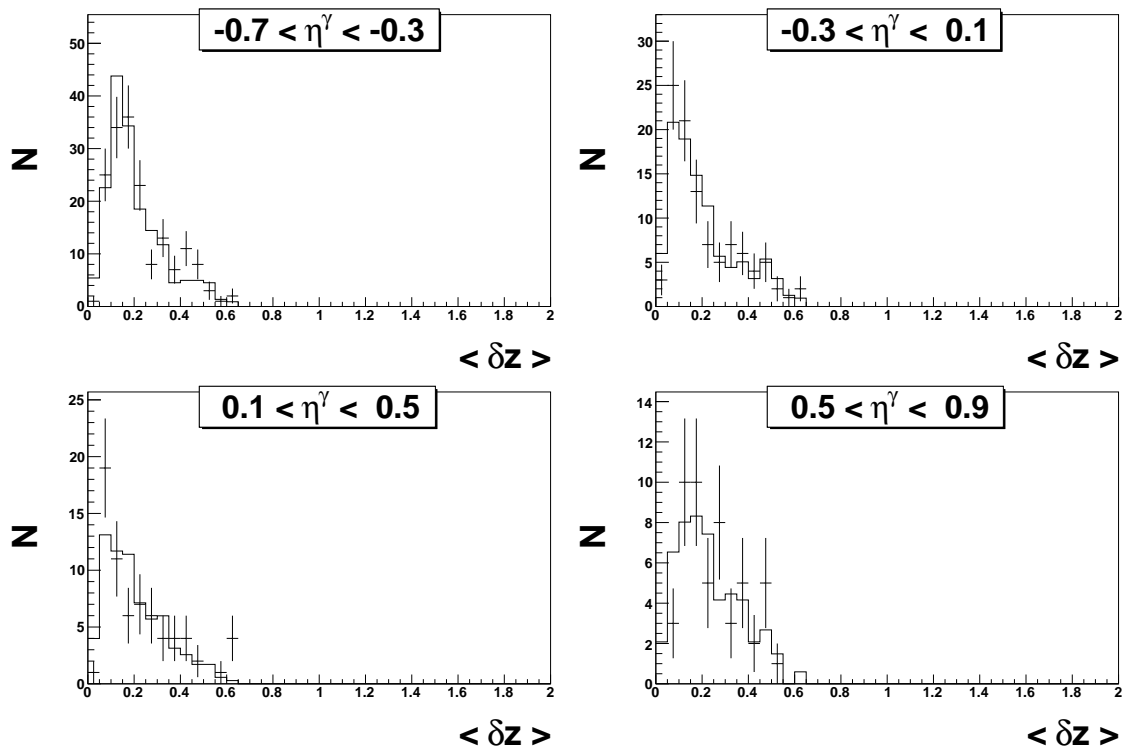


Figure 7.15: DVCS Data (crosses) compared to DVCS MC (histogram) for $\langle \delta z \rangle$ in different regions of η^γ when the photon was found with KTCLUS with $\langle \delta z \rangle < 0.65$.

Chapter 8

Prompt photons plus jet in photoproduction

The differential cross sections for prompt photons with associated jets in photoproduction are measured using the sample obtained in Chapter 5.8.2 with an integrated luminosity of 77 pb^{-1} . For these cross sections the photon was found using the KTCLUS method outlined in Chapter 6.3, with a distance to the closest track of $\Delta r > 1.0$. The associated jet was identified using KTCLUS as outlined in Chapter 5.8.3. The differential cross section for a given observable Y is determined as:

$$\frac{d\sigma}{dY} = \frac{N}{C \cdot \mathcal{L} \cdot \Delta Y} \quad (8.1)$$

where N is the number of prompt-photon events in a bin of size ΔY , C is the correction factor and \mathcal{L} is the integrated luminosity of the data sample used. The correction factor, C , was calculated using PYTHIA from the ratio of the number of reconstructed events after event selection cuts to the number of events at the hadron level using the combined PYTHIA *prompt photon with jet* and PYTHIA *inclusive dijet* MC sample which will be described in Section 8.1. The hadron level is defined in Chapter 4.3.

The correction factor corrects for both detector acceptance and purity.

To describe the prompt photon with jet data sample by a MC it must be verified that the BPRE response to photons is properly modeled by GEANT, Chapter 4.4. The modeling of the BPRE signal in the 1999-2000 ZEUS DVCS data by GEANT was verified via measurements of DVCS photons [61]. The DVCS measurement is similar to those performed for the 2004-2005 ZEUS data described in Chapter 7. DVCS provides a sample of photons with high purity, that can be compared to photons in DVCS MC.

A comparison between the 1999-2000 ZEUS DVCS data, from $\mathcal{L} = 77\text{pb}^{-1}$, and the DVCS Monte Carlo predictions [62] are presented in Figure 8.1 [10]. The DVCS MC sample describes the shape of the BPRE DVCS data distribution well, thus confirming that the BPRE response to photons is well simulated. The good agreement in the lowest BPRE signal bin confirms that the probability for a photon to convert into an e^+e^- pair before reaching the BCAL is well described by the DVCS MC.

8.1 Prompt Photon with jet + Inclusive Dijet MC Sample

Unlike the DVCS data sample, where the high photon purity is obtained from the kinematic requirements on the event, the prompt photon with jet data sample includes events where the photon candidate is something other than a photon *e.g.* a π^0 particle. For this reason the prompt photon with jet MC requires the addition of an inclusive dijet MC to describe the prompt photon with jet data.

The *prompt photon with jet + inclusive dijet* MC sample was produced by combining two independent samples generated by PYTHIA 6.3. One sample was generated to simulate the prompt photon with a jet process only and the second sample

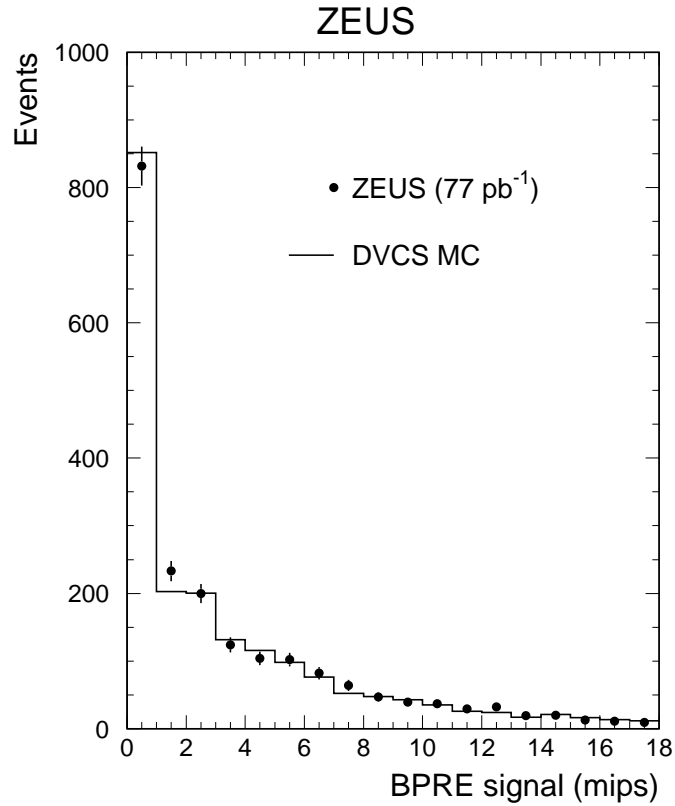


Figure 8.1: The 1999-2000 ZEUS DVCS data (points) compared to ZEUS DVCS MC (histogram).

was generated for inclusive dijet production. The inclusive dijet sample was used as the background MC to the prompt-photon with jet sample. The admixture of both samples was defined by fitting to the BPRE signal distribution to the data, which is summarized in Table 8.1. The fit was performed by the χ^2 minimization, as shown in Equation 8.2, with the additional requirement that the first bin of the BPRE distribution should not change. This requirement ensured that the overall conversion probability in the MC sample matched the data. The description of the conversation

probability in PYTHIA was proven to be correct using a clean DVCS sample, see Figure 8.1. The data and results of the fit to the data as shown in Figure 8.2, where the contributions to the final combined MC by both the prompt photon with jet signal and the inclusive dijet background MCs are shown also separately. The agreement in the first bin is required by the constraint on the fit. The tail of the distribution is also well described. The intermediate region shows some discrepancy, which means that while the global conversion rate is well described the description of a photon conversion before it begins to shower is not well described. This discrepancy will be accounted for in the forthcoming discussion of the error in the χ^2 fit.

$$\chi^2 = \sum_{i=1}^n \left(\frac{\text{Data}_i - \text{Combined MC}_i}{\text{Error}_i} \right)^2 \quad (8.2)$$

Once the minimum of the χ^2 fit is found, the fraction of the inclusive dijet MC was varied to change the χ^2 per degree of freedom by one. This variation was used to define the uncertainty in the extracted cross section due to the fit and it was found to be one of the major sources of uncertainty. When the χ^2 fit is varied the net change in the cross section is 11.4%. The error in the χ^2 fit is due to the statistical errors in reproducing the BPRE distribution and is therefore included in the statistical, not systematic, errors on the prompt photon with jet in photoproduction cross section measurements.

To confirm that the fraction of the combined prompt photon with jet + inclusive dijet MC that is from the prompt photon MC is correct, several other distributions were investigated that were sensitive to the presence of prompt-photon events. In Figure 8.3 the amount of E_T in the event not clustered into the prompt photon or

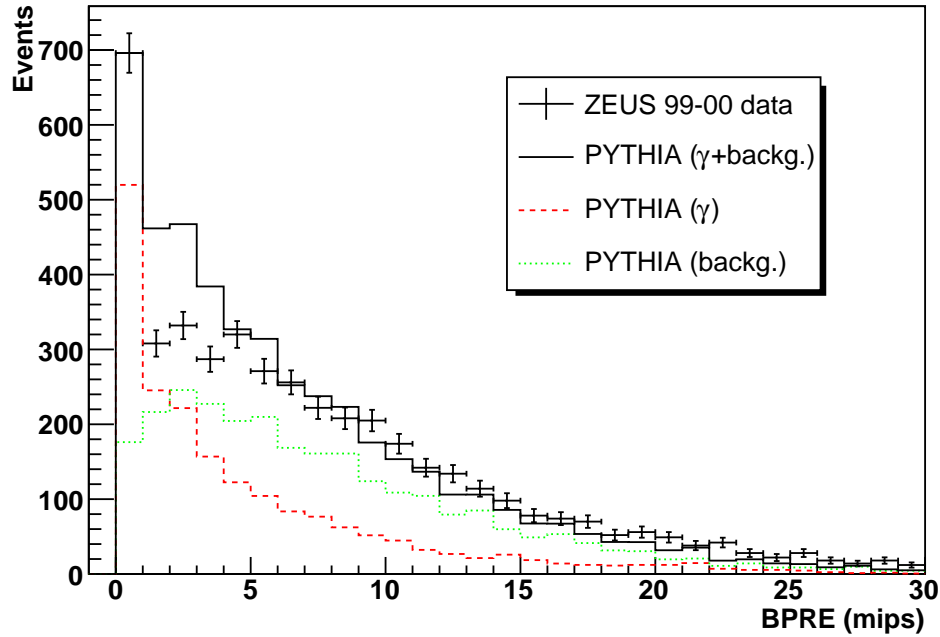


Figure 8.2: Comparison between 1999-2000 ZEUS prompt photon with jet in photo-production data and PYTHIA for the BPRE signal of the prompt photon candidate, in minimum ionizing particle units.

the jet in the ZEUS data can be seen compared to the combined prompt photon with jet + inclusive dijet MC. The distance in η, ϕ between the prompt photon and any track in the event can also be seen in Figure 8.3. The high level of agreement between the ZEUS prompt photon with jet data and the combined prompt photon with jet + inclusive dijet MC indicates that the event is well described.

In Figure 8.4 the fraction of the photon's (jet's) energy deposited in the electromagnetic section of the CAL for the ZEUS prompt photon data is compared to the combined prompt photon with jet + inclusive dijet MC. The agreement between them provides further confirmation that the photon and jet in the prompt photon with jet

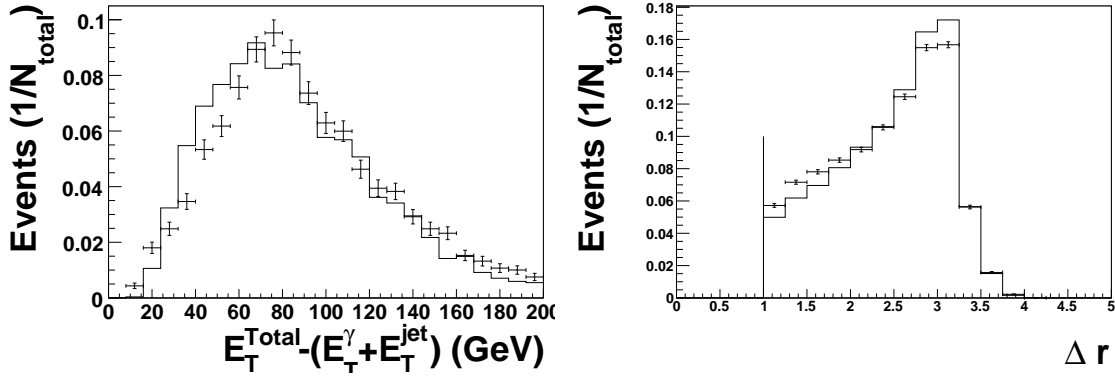


Figure 8.3: Comparison between 1999-2000 ZEUS prompt photon with jet in photoproduction data and combined prompt photon with jet + inclusive dijet MC sample for the E_T in the event not from the photon or the jet and distance between the photon and any track in the event.

data are well described by the combined prompt photon with jet + inclusive dijet MC predictions.

Once the fraction of the inclusive dijet PYTHIA events needed to model the 1999-2000 ZEUS prompt photon with jet in photoproduction data has been calculated the description of the data by the combined prompt photon with jet + inclusive dijet MC must be verified for each distribution for which a differential cross section will be measured. The detector level prompt photon with jet data distributions for E_T^γ , η^γ , E_T^{jet} , and η^{jet} are compared in Figure 8.5 to the MC predictions using the combined prompt photon with jet + inclusive dijet MC obtained from the BPRE signal fit. In Figure 8.6 the same comparison is demonstrated but for the momentum fraction of the exchanged photon, x_γ . The MC describes the data reasonably well for the E_T distributions and slightly worse for the η and x_γ distributions. The description of the η and x_γ distributions is better than the description of the BPRE distribution,

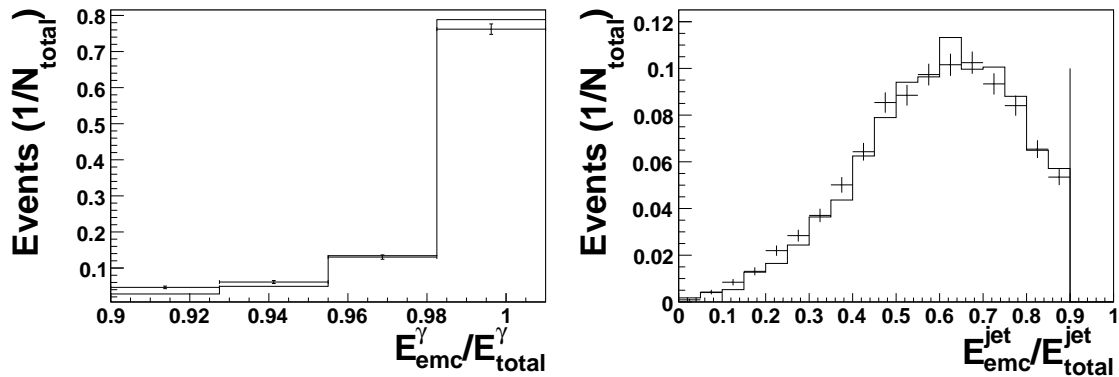


Figure 8.4: Comparison between 1999-2000 ZEUS prompt photon with jet in photo-production data and combined prompt photon with jet + inclusive dijet MC sample for the fraction of the photon's and jet's energy in the EMC section of the CAL.

therefore the uncertainty from the description of the η and x_{γ} distributions is not problematic because the uncertainty is dominated by the BPRE fit. This is confirmed by the level of agreement between this thesis and the published ZEUS cross sections, which will be shown later in this chapter, where the relative amount of inclusive dijet background events was allowed to vary from bin to bin.

Photons found with KTCLUS and $\Delta r > 1.0$			
% signal MC	% background MC	$\tilde{\chi}^2$	σ (pb)
42.0	58.0	1.89	$34.9 \pm 4.2(\text{stat.}) \pm {}^{(+4.0)}_{(-3.3)}(\text{sys.})$

Table 8.1: The measured prompt photon with jet in photoproduction cross section with the χ^2 per-degree-of-freedom minimum for the χ^2 fit on the BPRE distribution. The fraction of the combined prompt photon with jet + inclusive dijet MC that is from the prompt photon with jet MC is also given as the “% signal MC”.

8.2 Correction Factor

The combined prompt photon with jet + inclusive dijet PYTHIA MC can now be used to calculate the correction factor, C (Equation 8.3). The reconstructed events include the contribution from non-prompt photon events, mainly π^0 and η decays, while the hadron level will only include prompt photon events. The correction factors for E_T^γ , η^γ , E_T^{jet} , η^{jet} , and x_γ are shown in Figure 8.7. With the exception of the highest- η^γ and lowest- x_γ bins the correction factors only have small deviations from bin to bin. The highest- η^γ and lowest- x_γ bins have correction factors that are ≈ 3 times the size of the other bins, due to a decrease in efficiency [60] largely due to photon isolation in the forward regions.

$$C = \frac{\text{Number of reconstructed PYTHIA Events}}{\text{Number of hadron level prompt photon with jet PYTHIA events}} \quad (8.3)$$

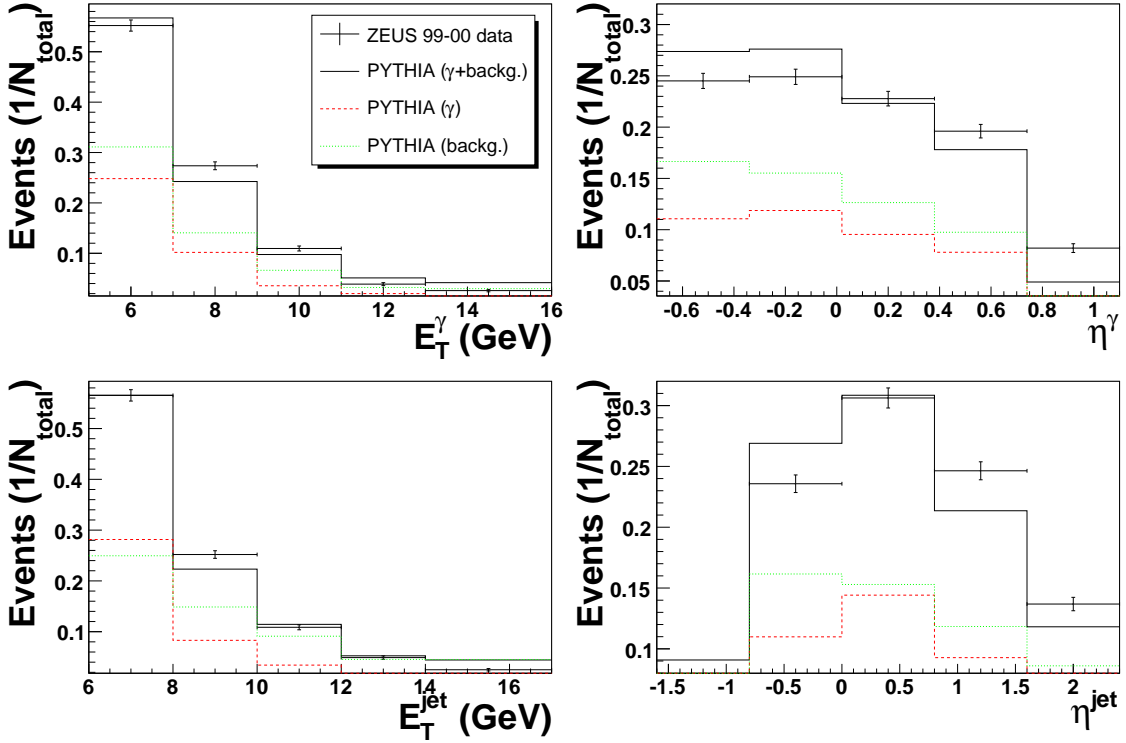


Figure 8.5: Comparison between 1999-2000 ZEUS prompt photon with jet in photo-production data and combined prompt photon with jet + inclusive dijet MC sample for E_T^γ , η^γ , E_T^{jet} , and η^{jet} . The contribution to the combined prompt photon with jet + inclusive dijet MC by the prompt photon with jet MC and inclusive dijet MC are also shown separately.

8.3 Systematic Uncertainty Estimates

The systematic uncertainties on the measured cross sections were estimated from varying the event selection by one σ of resolution of each variable [60]. The contribution to the systematic uncertainties for the main sources of systematic uncertainty, with each cut variation and contribution to the cross section given in parentheses as a percentage of the total cross section:

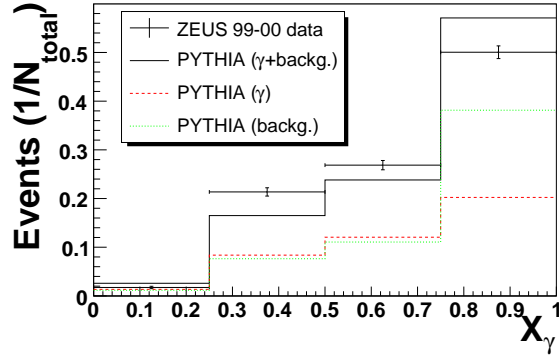


Figure 8.6: Comparison between 1999-2000 ZEUS prompt photon with jet in photo-production data and combined prompt photon with jet + inclusive dijet PYTHIA for X_γ . The contribution to the combined prompt photon with jet + inclusive dijet MC by the prompt photon with jet MC and inclusive dijet MC are also shown separately.

- Vary $E_{T,min}^\gamma$ by one σ , ± 0.4 GeV, in resolution, $(\begin{smallmatrix} +4.7 \\ -7.1 \end{smallmatrix})\%$
- Vary $E_{T,min}^{jet}$ by one σ , ± 0.86 GeV, in resolution, $(\begin{smallmatrix} +10.4 \\ -6.2 \end{smallmatrix})\%$
- Vary y_{jb} cuts by one $\sigma = 2\%$, $(\begin{smallmatrix} +1.9 \\ -1.1 \end{smallmatrix})\%$ and $(\begin{smallmatrix} +0.6 \\ -0.3 \end{smallmatrix})\%$
- Vary z_{vertex} cuts by 10%, $(\begin{smallmatrix} +0.05 \\ -0.09 \end{smallmatrix})\%$
- Vary missing P_T cut by one $\sigma = 2\%$, $(\begin{smallmatrix} +0.1 \\ -0.2 \end{smallmatrix})\%$

The overall systematic uncertainty was determined by adding the above uncertainties in quadrature. A 2% uncertainty in the luminosity measurement was not included in the uncertainty estimate. The total systematic uncertainty was determined to be $(\begin{smallmatrix} +11.5 \\ -9.5 \end{smallmatrix})\%$.

8.4 Cross sections

The total $ep \rightarrow e + \gamma_{prompt} + jet + X$ in photoproduction cross section in the region $5.0 < E_T^\gamma < 16.0$ GeV, $-0.74 < \eta^\gamma < 1.1$, $6.0 < E_T^{jet} < 17.0$ GeV, $-1.6 < \eta^{jet} < 2.4$, $0.2 < y < 0.8$, $Q^2 < 1$ GeV², and $E_T^{\gamma,(true)} > 0.9E_T^\gamma$. was measured to be

$$\sigma(ep \rightarrow e + \gamma_{prompt} + jet + X) = 34.9 \pm 4.2(\text{stat.}) \pm {}^{(+4.0)}_{(-3.3)}(\text{sys.}) \text{ pb}$$

The PYTHIA and HERWIG cross section predictions are 20.0 pb and 13.5 pb, respectively, with the difference largely attributable to the treatment of the terms for QED radiation. The prompt photon with jet cross section is also predicted by several theoretical NLO QCD calculations: $23.3^{+1.9}_{-1.7}$ pb (KZ) [15], $23.5^{+1.7}_{-1.6}$ pb (FGH) [13], and $30.7^{+3.2}_{-2.7}$ pb (LZ) [16]. The measured γ +jet differential cross sections are listed in Table 8.2. The measured γ +jet differential cross sections as functions of E_T^γ and η^γ compared to the PYTHIA 6.3 and HERWIG 6.5 predictions can be seen in Figure 8.8. The PYTHIA and HERWIG differential cross sections do not rise as steeply at low E_T^γ as do the data, which suggests that the inclusion of higher-order diagrams could improve agreement. In addition they underestimate the total cross section. The published ZEUS 1999-2000 differential cross sections as functions of E_T^γ and η^γ are shown in Figure 8.9 compared to the QCD predictions of KZ, FGH, and LZ. The QCD predictions also do not rise as steeply at low E_T^γ as do the data, but provide a significant improvement over the leading order Monte Carlo predictions. In particular the LZ prediction matches within errors for the lowest E_T^γ bin, possibly due to the treatment of the higher order terms.

The measured γ +jet differential cross sections as functions of E_T^{jet} and η^{jet} compared to the PYTHIA 6.3 and HERWIG 6.5 predictions can be seen in Figure 8.10.

The published ZEUS 1999-2000 differential cross sections as functions of E_T^{jet} and η^{jet} are shown in Figure 8.11 compared to the QCD predictions of KZ, FGH, and LZ. The PYTHIA, HERWIG and QCD predictions all underestimate the differential cross section at low E_T^{jet} . The low- E_T^γ and low- E_T^{jet} regions are where the QCD NLO predictions are most sensitive to higher order terms in their calculation [68]. The description of η^{jet} differential cross section has the largest differences between the theoretical predictions, possibly due to the different treatments of gluon radiation.

The measured γ +jet differential cross section as function of x_γ compared to the PYTHIA 6.3 and HERWIG 6.5 predictions can be seen in Figure 8.12. The largest differences between PYTHIA and HERWIG can be seen in the high- x_γ region. The published ZEUS 1999-2000 differential cross section as function of x_γ are shown in Figure 8.13 compared to the predictions of PYTHIA, HERWIG, KZ, FGH, and LZ. The KZ and FGH QCD predictions provide the best description of the data at high x_γ , which is sensitive to direct photoproduction. The LZ QCD prediction provides the best description of the data at low x_γ , which is sensitive to the resolved exchange photon contribution.

The published ZEUS results were done in parallel and with the same event selection as was done for this thesis. The only difference between the two analyses is the fitting procedure done to determine the admixture used to obtain the prompt photon with jet + inclusive dijet MC sample. A single global fraction for the amount of prompt photon events was used in this analysis, while the published ZEUS results allowed the fraction to vary linearly for E_T^γ , η^γ , E_T^{jet} , η^{jet} and x_γ . This provided the ZEUS results with a greater independence from the MC description of E_T^γ , η^γ , E_T^{jet} ,

η^{jet} and x_γ . One consequence for the published ZEUS results is the description of E_T^{jet} , η^{jet} and x_γ depend on the photon in an indirect way. This is the most likely explanation for the differences seen between this analysis and the published ZEUS results for η^{jet} shown in Figure 8.10.

E_T^γ (GeV)	$d\sigma/dE_T^\gamma$ (pb/GeV)
5.00, 7.00	9.8 \pm 1.2
7.00, 9.00	4.0 \pm 0.5
9.00, 11.00	1.9 \pm 0.3
11.00, 13.00	0.7 \pm 0.1
13.00, 16.00	0.3 \pm 0.1
η^γ	$d\sigma/d\eta^\gamma$ (pb)
-0.74, -0.34	20.2 \pm 2.6
-0.34, 0.02	22.5 \pm 2.9
0.02, 0.38	22.2 \pm 2.8
0.38, 0.74	16.6 \pm 2.3
0.74, 1.10	19.6 \pm 3.6
E_T^{jet} (GeV)	$d\sigma/dE_T^{jet}$ (pb/GeV)
6.00, 8.00	11.4 \pm 1.4
8.00, 10.00	3.3 \pm 0.4
10.00, 12.00	1.3 \pm 0.2
12.00, 14.00	0.7 \pm 0.1
14.00, 17.00	0.2 \pm 0.1
η^{jet}	$d\sigma/d\eta^{jet}$ (pb)
-1.60, -0.80	3.7 \pm 0.6
-0.80, 0.00	9.4 \pm 1.2
0.00, 0.80	12.3 \pm 1.6
0.80, 1.60	11.1 \pm 1.5
1.60, 2.40	7.4 \pm 1.1
x_γ	$d\sigma/dx_\gamma$ (pb)
0.00, 0.25	7.7 \pm 3.3
0.25, 0.50	33.8 \pm 5.0
0.50, 0.75	25.2 \pm 3.5
0.75, 1.00	72.1 \pm 9.1

Table 8.2: The differential prompt-photon with associated jet in PHP cross sections measured in the region $5.0 < E_T^\gamma < 16.0$ GeV, $-0.74 < \eta^\gamma < 1.1$, $6.0 < E_T^{jet} < 17.0$ GeV, $-1.6 < \eta^{jet} < 2.4$, $0.2 < y < 0.8$, $Q^2 < 1$ GeV², and $E_T^{\gamma,(true)} > 0.9E_T^\gamma$. The uncertainties shown are statistical.

8.4.1 Comparison with H1 Results

H1 has published cross sections in the photoproduction regime. Both inclusive samples and samples with associated jets were studied. For the most recent H1 publication the photons were required to have $5 < E_T^\gamma < 10$ GeV and $-1 < \eta^\gamma < 0.9$. The associated jets were required to have $4.5 < E_T^{jet} < 11$ GeV and $-1 < \eta^{jet} < 2.3$. A direct comparison between ZEUS and H1 is difficult because a direct comparison would require a significant model-dependent extrapolation to the lower E_T^{jet} region used by H1.

The H1 E_T^γ and η^γ differential cross sections are shown in Figure 8.14. The cross section as functions of E_T^{jet} , η^{jet} , X_γ , and X_p are shown in Figure 8.15. The data are compared to LO and NLO predictions from K&Z [15] and FGH [13]. The K&Z calculation is shown corrected to the hadron level with and without correction for multiple interactions (m.i.). The NLO corrections are substantial, particularly with increasing η^γ . The NLO/LO ratio increases from 1.2 to 1.4 with increasing η^γ . The largest ratio of NLO correction is in the direct, high- x_γ , photoproduction regime.

The overall normalizations of the H1 differential cross sections are not very well described by NLO predictions, as was seen in the ZEUS data. Neither result showed systematic differences between data and the NLO predictions that were dependent on the pseudorapidity of the photon or the jet, *i.e.* some predictions were shifted forward, some were shifted towards the rear and some were more strongly peaked than the data. In the ZEUS data (Figure 8.9 and 8.11) the largest differences with the predictions could be seen at low E_T^γ and low E_T^{jet} , while this dependence was not seen in the H1

result. One important difference between this thesis and the H1 results is that the H1 results had the minimum allowed E_T of the jet less than the minimum allowed E_T of the photon, whereas ZEUS had the minimum allowed E_T of the photon to be less than the minimum allowed E_T of the jet. It may be possible that requiring the minimum allowed E_T of the photon be less than the minimum allowed E_T of the jet is problematic for the NLO QCD calculations [14].

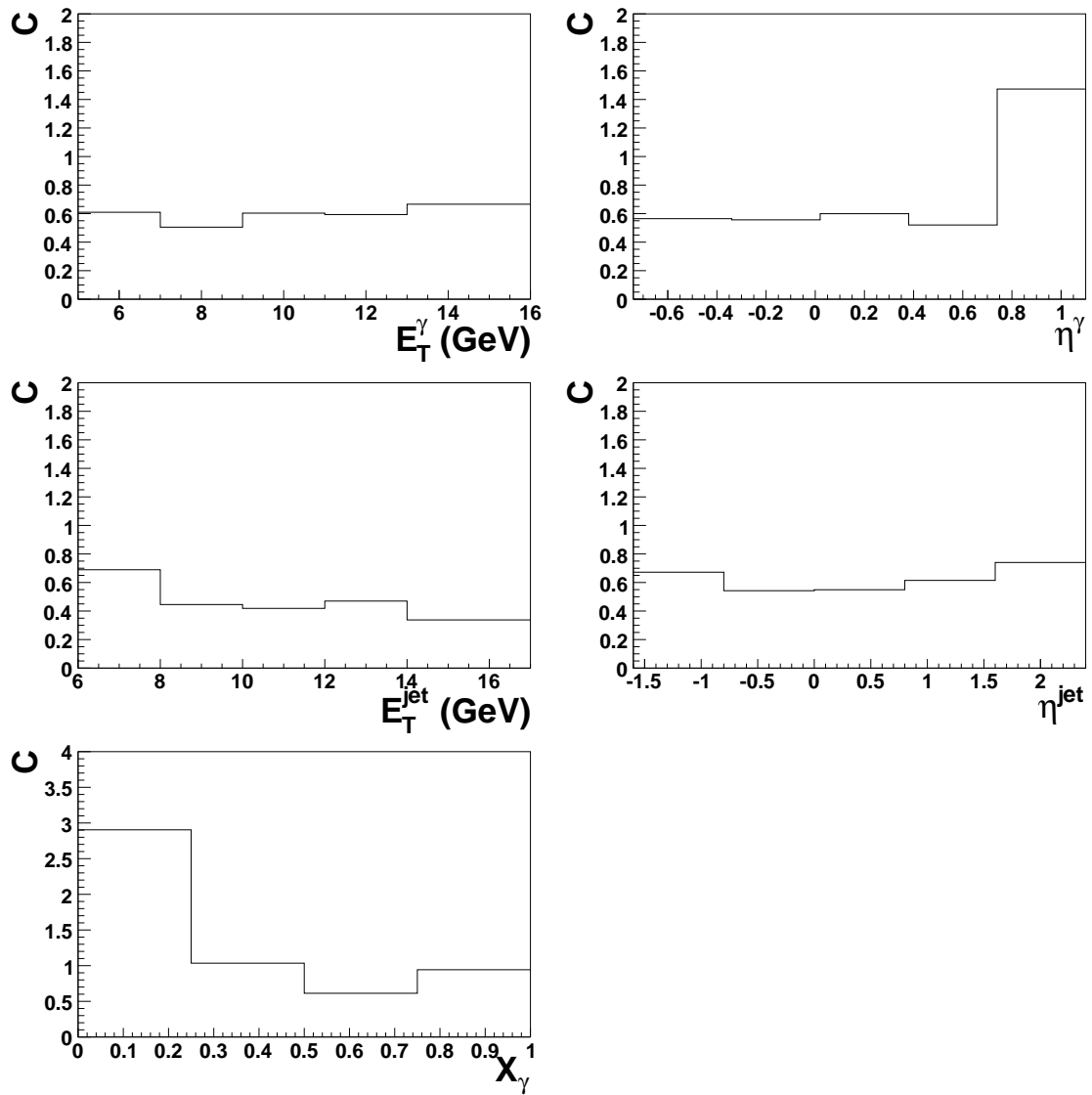


Figure 8.7: The correction factors for the E_T^γ , η^γ , E_T^{jet} , η^{jet} , and x_γ distributions.

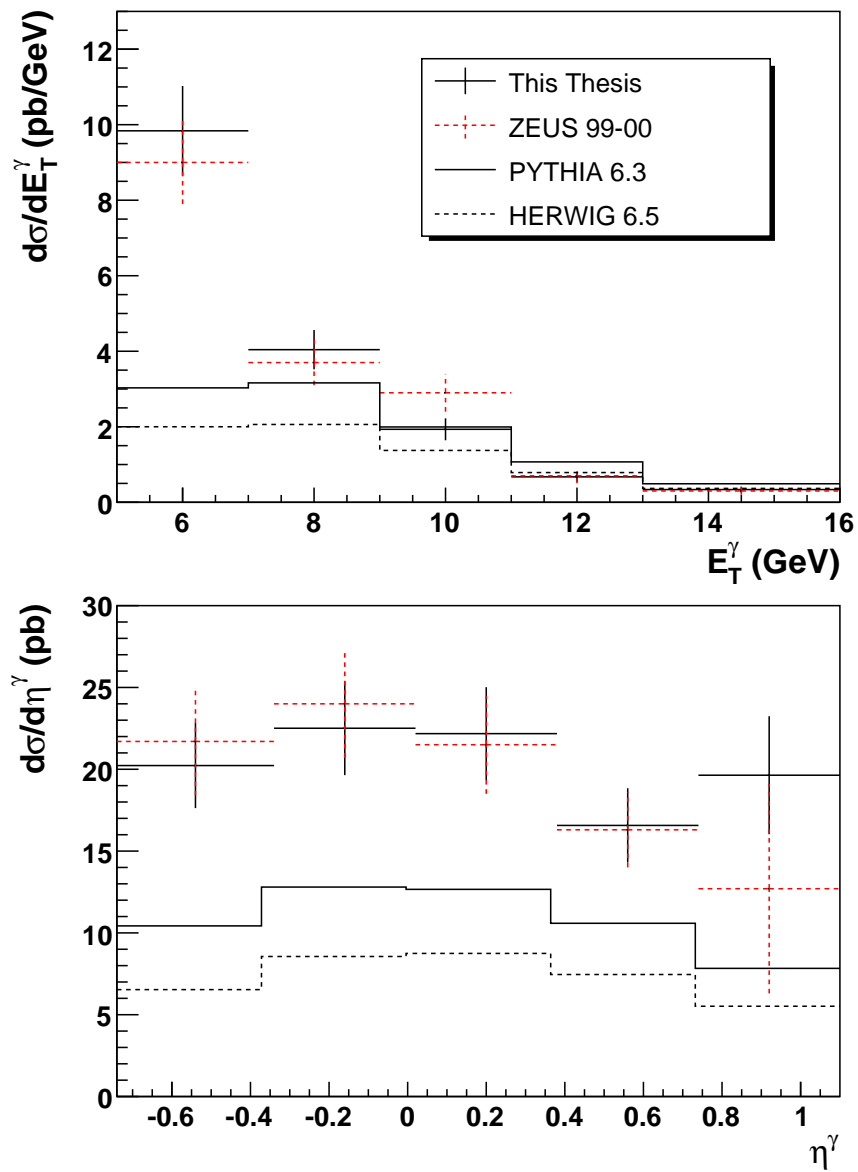


Figure 8.8: The γ +jet differential cross sections as functions of E_T^γ and η^γ . The 1999-2000 data from this thesis (solid black crosses) are compared to the published ZEUS 1999-2000 data (red dashed crosses), the PYTHIA 6.3 predictions (solid histogram), and the HERWIG 6.5 predictions (dashed histogram).

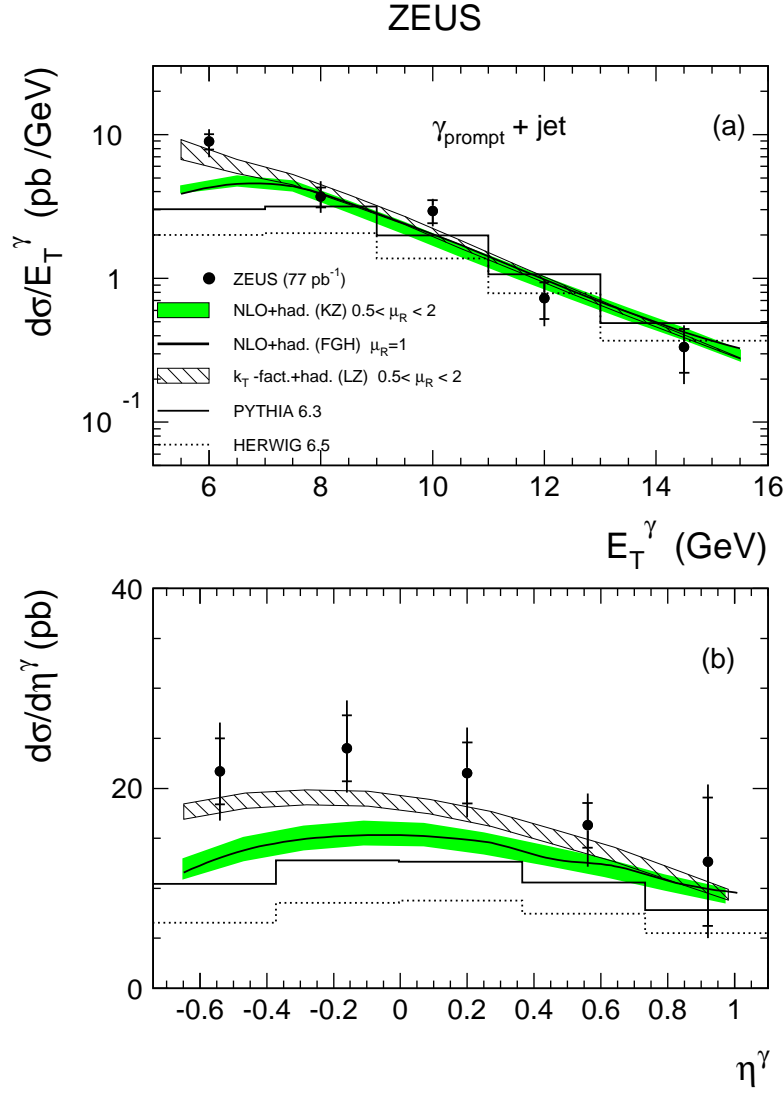


Figure 8.9: The γ +jet differential cross sections as functions of E_T^γ and η^γ . The published ZEUS 1999-2000 data (points) are compared to the theoretical QCD calculations and predictions of Monte Carlo models. The bands for the KZ and LZ predictions correspond to the uncertainty in the renormalisation scale which was changed by a factor of 0.5 and 2.

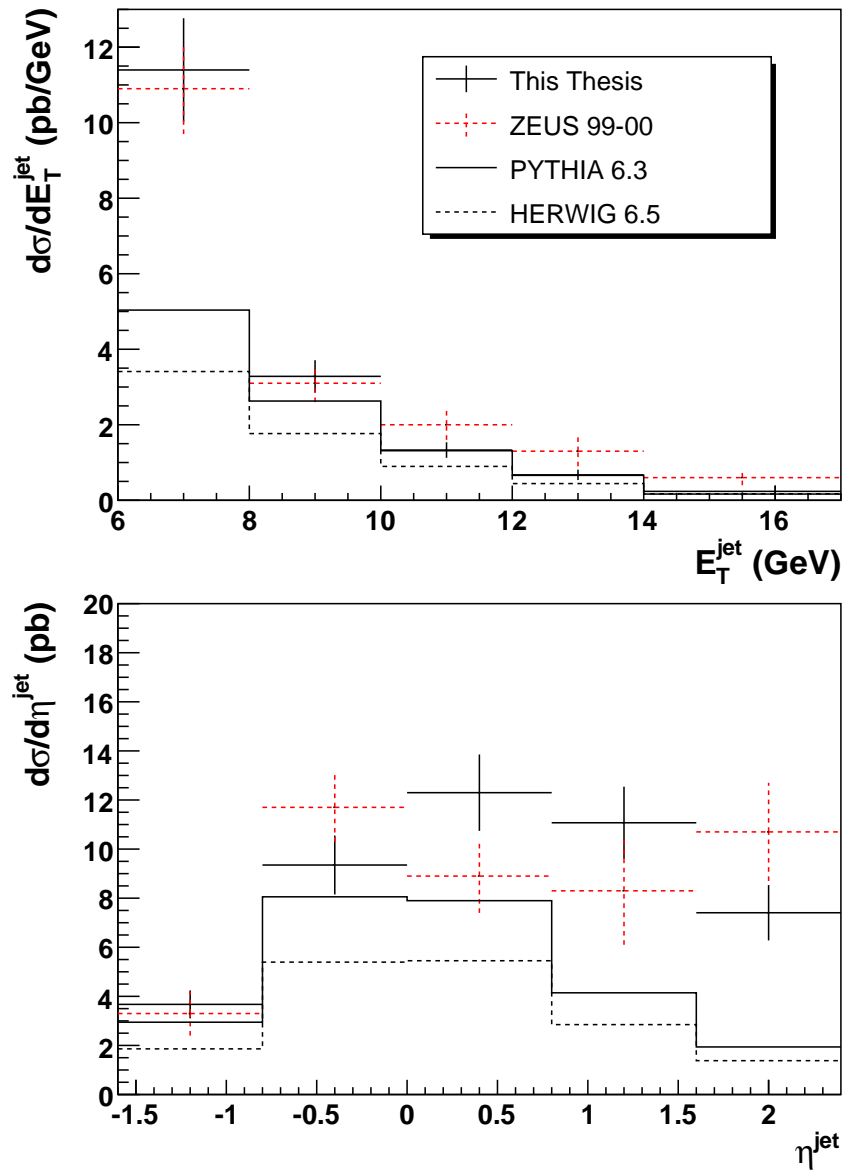


Figure 8.10: The γ +jet differential cross sections as functions of E_T^{jet} and η^{jet} . The 1999-2000 data from this thesis (solid black crosses) are compared to the published ZEUS 1999-2000 data (red dashed crosses), the PYTHIA 6.3 predictions (solid histogram), and the HERWIG 6.5 predictions (dashed histogram).

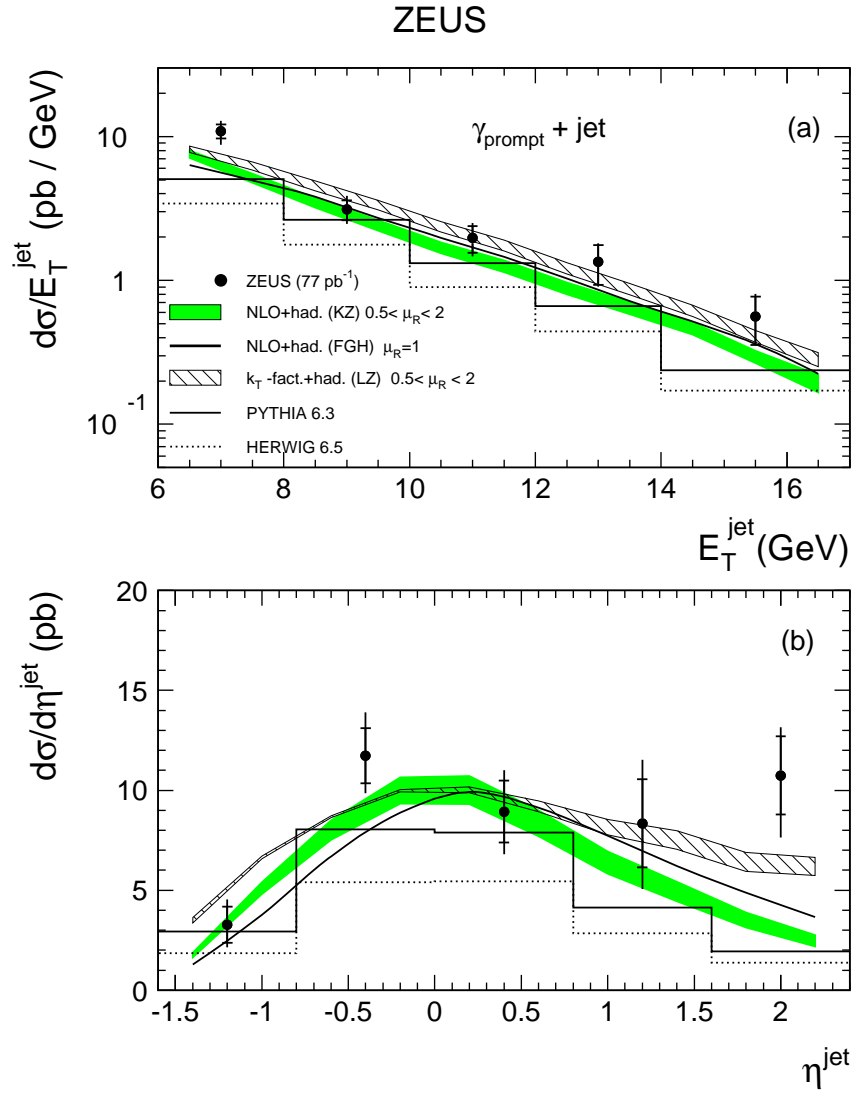


Figure 8.11: The γ +jet differential cross sections as functions of E_T^{jet} and η^{jet} . The published ZEUS 1999-2000 data (points) are compared to the theoretical QCD calculations and predictions of Monte Carlo models. The bands for the KZ and LZ predictions correspond to the uncertainty in the renormalisation scale which was changed by a factor of 0.5 and 2.

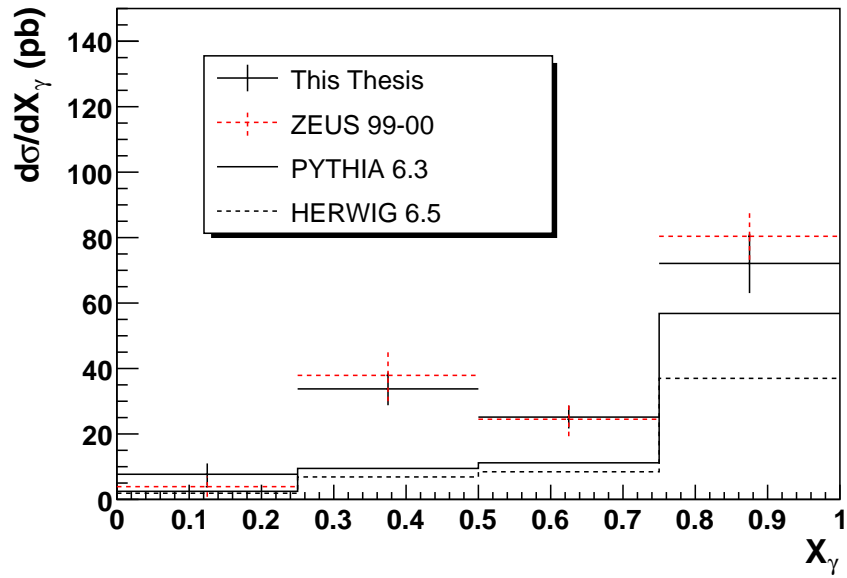


Figure 8.12: The γ +jet differential cross sections as function of X_γ . The 1999-2000 data from this thesis (solid black crosses) are compared to the published ZEUS 1999-2000 data (red dashed crosses), the PYTHIA 6.3 predictions (solid histogram), and the HERWIG 6.5 predictions (dashed histogram).

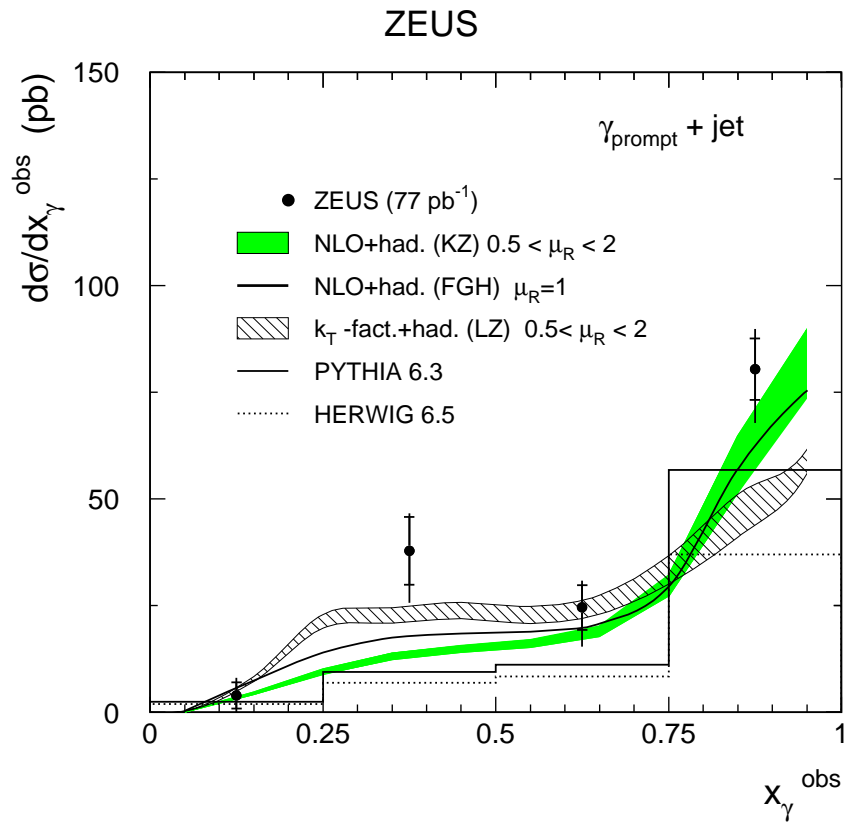


Figure 8.13: The γ +jet differential cross sections as functions of X_γ . The published ZEUS 1999-2000 data (points) are compared to the theoretical QCD calculations and predictions of Monte Carlo models. The bands for the KZ and LZ predictions correspond to the uncertainty in the renormalisation scale which was changed by a factor of 0.5 and 2.

Inclusive prompt photon

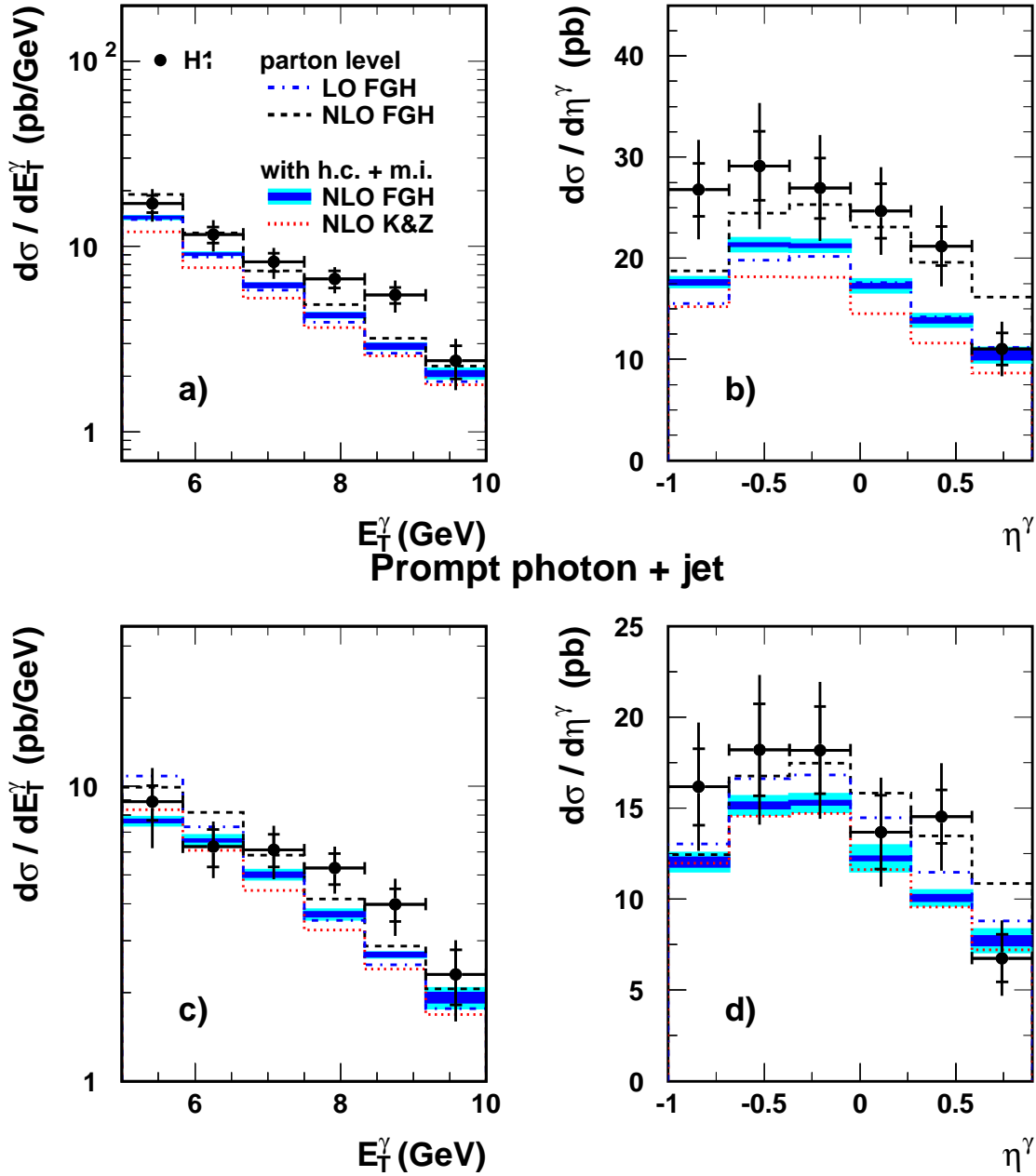


Figure 8.14: The inclusive prompt photon cross section in photoproduction (a,b) measured by H1 at $\sqrt{s} = 319$ GeV as functions of E_T^γ and η^γ , and with the additional requirement of a jet with $E_T^{jet} > 4.5$ GeV and $-1 < \eta^\gamma < 2.3$ (c,d).

Prompt photon + jet

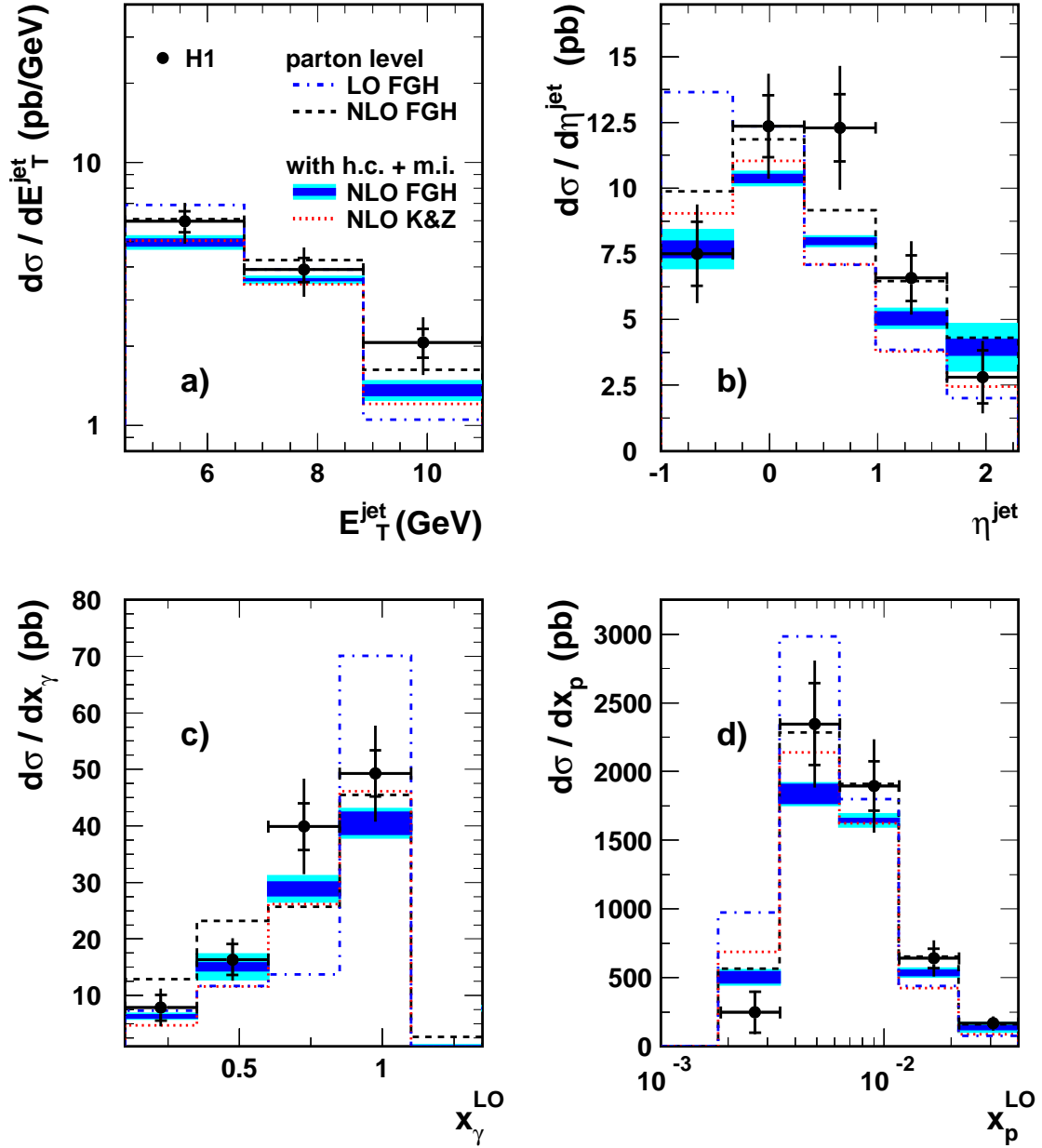


Figure 8.15: The prompt photon cross section in photoproduction measured by H1 with the requirement of a jet with $E_T^{\text{jet}} > 4.5$ GeV and $-1 < \eta^{\text{jet}} < 2.3$ as a function of E_T^{jet} and η^{jet} (a,b). The cross section as a function of the fraction of the proton's momentum involved in the collision, X_p , and the fraction of the exchange photon's momentum involved in the collision, X_γ , are also shown (c,d).

Chapter 9

Inclusive prompt photons in DIS

The sample of inclusive prompt-photon events in DIS was obtained, as described in Chapter 5. Both ELEC5 and KTCLUS methods outlined in Chapter 6.3 were used to identify prompt photons. The cross section was calculated as:

$$\sigma = \frac{N}{C \cdot \mathcal{L}} \quad (9.1)$$

where N is the number of prompt-photon events after all selection cuts, C is the correction factor and \mathcal{L} is the integrated luminosity of the sample. The correction factor was calculated as the ratio of reconstructed events after all event selection cuts to the number of generated events at the hadron level using the combined prompt photon + inclusive DIS MC sample described below.

The final MC sample, *combined prompt photon + inclusive DIS*, was produced using two different MC generators. PYTHIA 6.3 was used to generate the prompt photon in DIS events. PYTHIA was used in the previous analyses [7] and is expected to describe the prompt photon signal well. An inclusive DIS sample generated with ARIADNE 4.12 is being used by several ongoing ZEUS analyses to describe the inclusive DIS production at HERA, therefore it was selected in this case as a sample for

the background MC. The admixture of the prompt photon and inclusive DIS MC in the final sample was determined by a fit to the data.

The fit was performed independently using three different variables: BPRE signal, f_{max} , and $\langle\delta z\rangle$, for both of the ELEC5 and KTCLUS prompt photon identification methods. Each fit was performed over all the non-zero bins for a distribution: 15 bins for BPRE, 13 bins for $\langle\delta z\rangle$, and up to 20 bins for f_{max} . Only statistical errors in the data and MC were considered. The χ^2 of the fit was calculated according to Equation 8.2. After the best fit was achieved, the fit was varied such that the $\tilde{\chi}^2$ increased by 1 to estimate the error on the extracted cross section. As with the prompt photon with jet in PHP measurement the fit on the BPRE distribution for the prompt photon in DIS sample had the additional requirement that the lowest bin match.

The HERAII 2004-2005 data used corresponds to an integrated luminosity of 109 pb^{-1} . The cross section was measured for $Q^2 > 35.0 \text{ GeV}^2$, the photons were required to have $5.0 < E_T^\gamma < 20.0 \text{ GeV}$ and $-0.7 < \eta^\gamma < 0.9$. An additional isolation requirement at the hadron level of $E_T^{\gamma,(true)} > 0.9E_T^\gamma$ was applied, as was used in the theoretical calculations. This requirement ensured that the MC sample, which was used to calculate the correction factor A , contained well isolated single photons at the hadron level.

The results of the MC prompt photon to inclusive DIS fits are demonstrated in Figures 9.1 and 9.2 for ELEC5 and KTCLUS methods correspondingly and for the BPRE signal, f_{max} , and $\langle\delta z\rangle$ distributions. The extracted admixture of the prompt photon MC, values for the χ^2 -per-degree-of-freedom ($\tilde{\chi}^2$), and extracted cross sections are summarized in Table 9.1. Both the shower shape variables provide consistent

results but vary significantly from the BPRE fit. The fit to the BPRE signal has a much higher $\tilde{\chi}^2$, it predicts significantly larger amounts of signal and had larger uncertainty compared to the prompt photon with jet in PHP measurement which used HERAI data. This indicates that a final tuning of the BPRE MC simulation or recalibration of the BPRE signal for data will be needed to use it in analyses with HERAII data. This was also demonstrated in Figures 7.6 and 7.7, where the description of the DVCS signal in HERAII data was found to be worse than for the HERAI data. The BPRE was therefore not used in this analysis for the extraction of the inclusive prompt photon in DIS cross section.

Table 9.1 demonstrates that using KTCLUS method instead of ELEC5 systematically increases the number of prompt photon events needed to describe the prompt photon in DIS data and as a result leads to an increased cross section. Also shown in Table 9.1 is the convergence of the ELEC5 and KTCLUS methods for finding photons when the photon candidate is required to be well isolated from tracks. In Figure 9.3 the distance between the prompt photon candidate and its closest track for the ZEUS prompt photon in DIS data is compared to the predictions from prompt photon PYTHIA and inclusive DIS ARIADNE. When there is a high- P_T track near the photon candidate, KTCLUS will cluster it with an energy deposit causing the energy deposit being rejected as a photon candidate. For both ELEC5 and KTCLUS the prompt photon data is between the prompt photon and inclusive DIS MC predictions. This supports the assumption that the prompt photon data is described by a linear combination of the prompt photon and inclusive DIS MCs. For $\Delta r > 1.1$ both ELEC5 and KTCLUS have similar shapes for the Δr distribution.

Photons found with ELEC5 and $\Delta r > 0.2$				
Distribution	% signal MC	% background MC	$\tilde{\chi}^2$	σ (pb)
f_{max}	11.9	88.1	1.75	$5.8 \pm 1.0^{(+4.15)}_{(-3.63)}$
$\langle \delta z \rangle$	15.7	84.3	0.77	$6.9 \pm 1.3^{(+3.58)}_{(-3.89)}$
BPRE	52.2	47.8	2.86	
Photons found with KTCLUS and $\Delta r > 0.2$				
Distribution	% signal MC	% background MC	$\tilde{\chi}^2$	σ (pb)
f_{max}	30.3	69.7	0.73	$8.58 \pm 2.6^{(+5.2)}_{(-5.7)}$
$\langle \delta z \rangle$	34.7	65.3	0.72	$9.74 \pm 3.2^{(+5.6)}_{(-6.0)}$
BPRE	73.5	26.5	2.17	
Photons found with ELEC5 and $\Delta r > 1.1$				
Distribution	% signal MC	% background MC	$\tilde{\chi}^2$	σ (pb)
f_{max}	32.8	67.2	0.75	$7.31 \pm 0.35^{(+5.08)}_{(-4.68)}$
$\langle \delta z \rangle$	40.1	59.9	0.52	$8.26 \pm 0.38^{(+3.96)}_{(-4.52)}$
BPRE	64.0	36.0	1.72	
Photons found with KTCLUS and $\Delta r > 1.1$				
Distribution	% signal MC	% background MC	$\tilde{\chi}^2$	σ (pb)
f_{max}	47.4	52.6	0.59	$9.02 \pm 0.44^{(+6.12)}_{(-6.26)}$
$\langle \delta z \rangle$	54.4	45.6	0.62	$9.92 \pm 0.48^{(+7.36)}_{(-5.85)}$
BPRE	79.3	20.7	1.49	

Table 9.1: The measured prompt photon in DIS cross sections and χ^2 per-degree-of-freedom minimums for the different χ^2 fits for the ratio of prompt-photon PYTHIA DIS MC to inclusive background ARIADNE DIS MC. The contribution to the uncertainty by the χ^2 fit is listed separately and in parentheses.

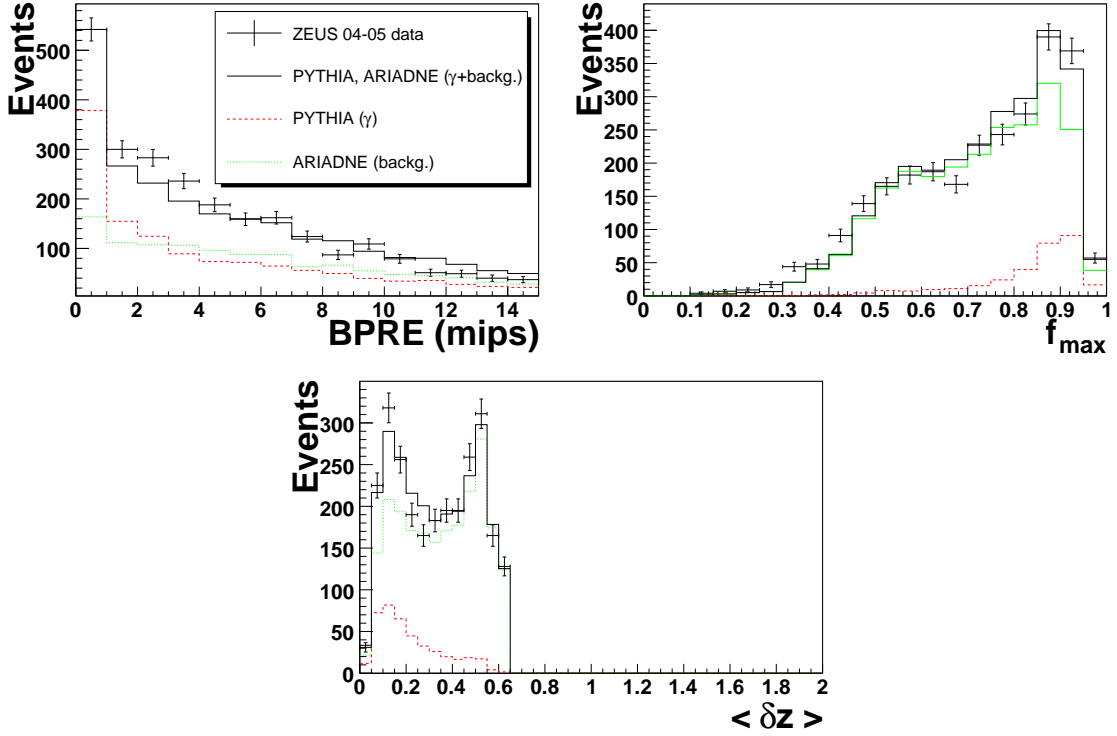


Figure 9.1: Comparison between ZEUS prompt photon data and PYTHIA MC predictions for prompt photons in DIS with and without ARIADNE background simulation. The solid line represents the result of the best fit to the data using a mixture of the prompt photon and inclusive DIS MCs. The prompt photons were identified using the ELEC5 photon finder with $\Delta r > 0.2$.

The extracted cross sections listed in Table 9.1 can be compared to the previous ZEUS measurement, which used the ELEC5 method only. The previous ZEUS cross section measurement of prompt photons in DIS, using the shower shape variables, was found to be: $5.64 \pm 0.58(\text{stat.})^{+0.47}_{-0.72}(\text{sys.})$ pb [5], with the additional requirement that the prompt photon have $E_T^\gamma < 10$ GeV. When this additional constraint is used, with this analysis, it lowers the cross section measured with $\Delta r > 1.1$ by ≈ 2.4 (≈ 2.6) for

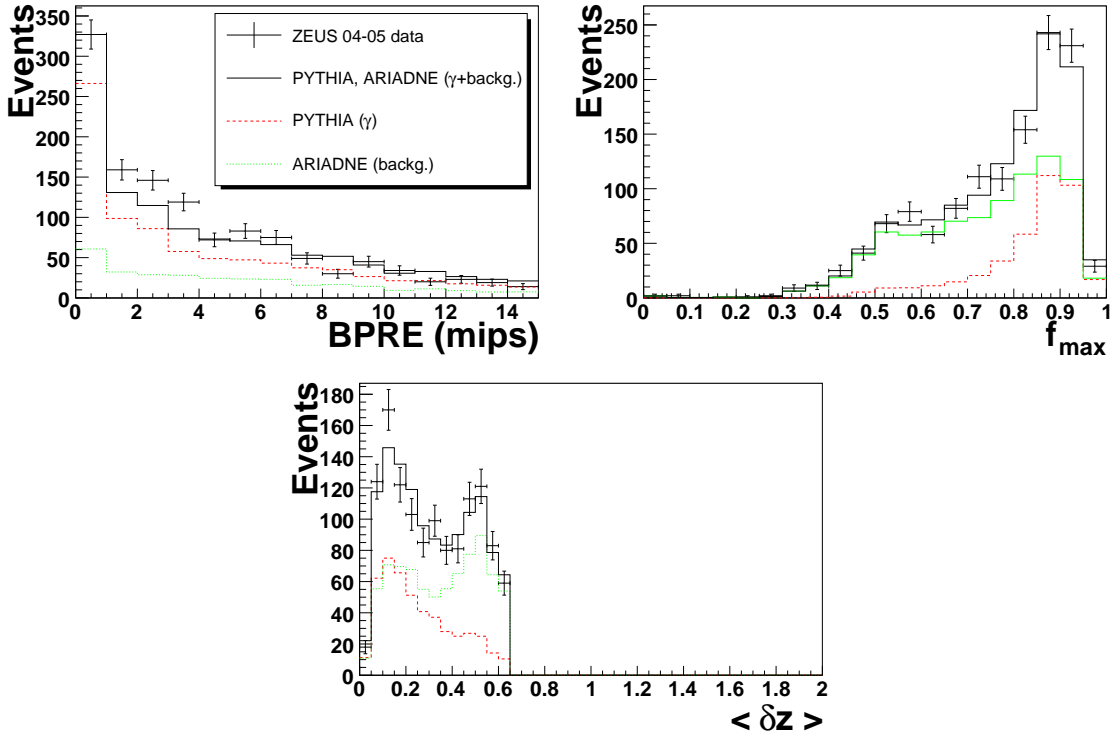


Figure 9.2: Comparison between ZEUS prompt photon data and PYTHIA MC predictions for prompt photons in DIS with and without ARIADNE background simulation. The solid line represents the result of the best fit to the data using a mixture of the prompt photon and inclusive DIS MCs. The prompt photons were identified using the KTCLUS photon finder with $\Delta r > 0.2$.

ELEC5 (KTCLUS) to between 5.9 and 7.3 pb. While consistent with the previous ZEUS measurement, the current analysis demonstrates that further improvement in the BPRE calibration and tuning of the BPRE MC simulation is still needed. Combinations of f_{max} , $\langle \delta z \rangle$, and BPRE in conjunction with increased statistics can certainly lead to a better measurement in the future. One way to accomplish this is the construction of a neural network based on the photon candidate's shower shapes and

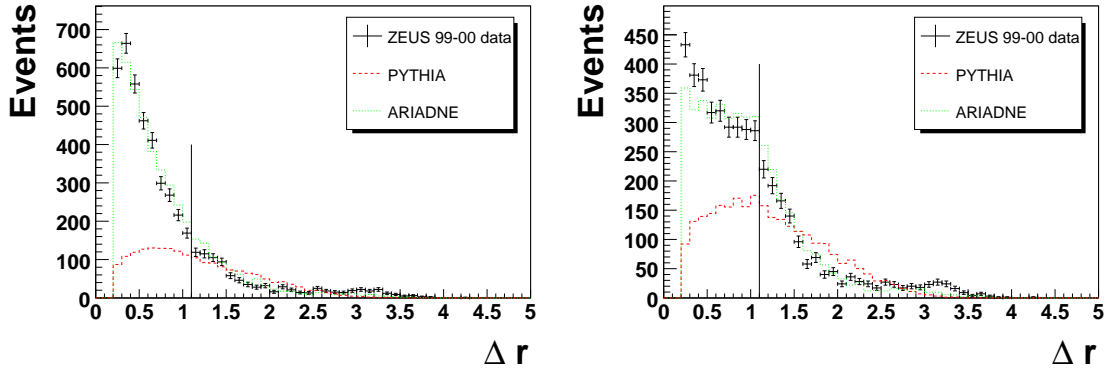


Figure 9.3: Comparison between ZEUS prompt photon data and the predictions from prompt photon in DIS PYTHIA MC and inclusive ARIADNE MC for the distance in (η, ϕ) from the prompt photon candidate to the closest track. The photons were identified with ELEC5 (Left) and KTCLUS (Right) independently. The MC predictions are normalized to the data for $\Delta r > 1.1$.

BPRE energy deposit. The neural network would need to be trained on several large single particle MC samples. The relative contribution from each type of neutral meson can be taken from the PYTHIA and HERWIG MC generators. The sensitivity to the dead material between the interaction point and the BCAL would require separate training of the neural network for the HERAI and HERAII data sets. Once trained the neural network could be tested on the Deeply Virtual Compton Scattering data and MC to confirm that it operates with a high efficiency for photons.

Chapter 10

Summary

The photoproduction of prompt photons with an accompanying jet has been measured with the ZEUS detector at HERA using an integrated luminosity of 77 pb^{-1} . The total $ep \rightarrow e + \gamma_{prompt} + jet + X$ cross section was measured, where the final state photon satisfied $5.0 < E_T^\gamma < 16.0 \text{ GeV}$ and $-0.74 < \eta^\gamma < 1.1$ and the accompanying jet satisfied $6.0 < E_T^{jet} < 17.0 \text{ GeV}$ and $-1.6 < \eta^{jet} < 2.4$. The cross section is determined for $0.2 < y < 0.8$, $Q^2 < 1 \text{ GeV}^2$, $E_T^{\gamma,(true)} > 0.9 \cdot E_T^\gamma$. The differential cross sections as functions of E_T and η for the prompt photon candidate and for the accompanying jets were measured. The differential cross section as a function of x_γ was also measured. The measured cross section,

$$\sigma(ep \rightarrow e + \gamma_{prompt} + jet + X) = 34.9 \pm 4.2(\text{stat.}) \pm ({}_{-3.3}^{+4.0})(\text{sys.}) \text{ pb}$$

is above the PYTHIA and HERWIG MC predictions, which predict a less steep rise of the cross section with decreasing E_T^γ . The discrepancy is reduced for the KZ, FGH and LZ NLO calculations. The best description of the data was found for the LZ NLO calculation based on the k_T -factorization approach and unintegrated parton densities.

The first inclusive measurement of isolated photons with high E_T^γ in DIS using HERAII data was performed. The measurement is consistent with the previous ZEUS measurement which used HERAI data, but a better understanding of the ZEUS BPRE detector after the HERA upgrade is still needed. The methods developed and investigated in this analysis provide a means for a much more precise measurement of the prompt photon data. The use of both the ELEC5 and KTCLUS to find photons provides an additional means of confirming future results, as well as providing a variety of different levels of photon isolation.

Bibliography

- [1] S. L. Glashow and S. Weinberg, Phys. Rev. **D 15**, 1958 (1977).
- [2] V.M. Abazov et al., Phys. Lett. **B 639**, 151 (2006).
- [3] M. Gluck, L. E. Gordon, E. Reya and W. Vogelsang, Phys. Rev. Lett. **73**, 388 (1994).
- [4] J.D. Bjorken, Phys. Rev. **179**, 1547 (1969).
- [5] ZEUS Coll., S. Chekanov et al., Phys. Lett. **B 595**, 86 (2004).
- [6] ZEUS Coll., J. Brietweg et al., Phys. Lett. **B 413**, 201 (1997).
- [7] ZEUS Coll., S. Chekanov et al., Phys. Lett. **B 511**, 19 (2001).
- [8] ZEUS Coll., J. Brietweg et al., Phys. Lett. **B 472**, 175 (2000).
- [9] H1 Coll., A. Aktas et al., Eur. Phys. J **C 38**, 417 (2005).
- [10] ZEUS Coll., S. Chekanov et al., Eur. Phys. J **C 49**, 511 (2007).
- [11] W. M. Yao et al., J. Phys. **G 33**, 1 (2006).
- [12] S. Catani et al., JHEP **05**, 028 (2002).
- [13] M. Fontannaz, J.P. Guillet and G. Heinrich, Eur. Phys. J **C 21**, 303 (2001).
- [14] M. Fontannaz and G. Heinrich, Eur. Phys. J. **C 34**, 191 (2004).
- [15] M. Krawczyk and A. Zembrzuski, Phys. Rev. **D 64**, 14017 (2001).
- [16] AV. Lipatov and N.P. Zotov, Phys. Rev. **D 72**, 54002 (2005).
- [17] M. Glück, E. Reya and A. Vogt, Phys. Rev. **D 46**, 1973 (1992).
- [18] TESLA Coll., Web page available on <http://tesla-new.desy.de/>. .

- [19] ZEUS Coll., U.Holm (ed.), *The ZEUS Detector*. Status Report (unpublished), DESY (1993), available on <http://www-zeus.desy.de/bluebook/bluebook.html>. .
- [20] S. Magill and S. Chekanov, *Proceedings of the IX Int. Conference on Calorimetry (Annecy, Oct 9-14, 2000)*, B. Aubert et al. (ed.)p. 625. Frascati Physics Series 21, Annecy, France (2001).
- [21] H.L. Lai et al., Phys. Rev. **D 51**, 4763 (1995).
- [22] CTEQ Coll., H.L. Lai et al., Eur. Phys. J. **C 12**, 375 (2000).
- [23] M. Glück, E. Reya and A. Vogt, Phys. Rev. **D 45**, 3986 (1992).
- [24] M. Glück, E. Reya and A. Vogt, Phys. Rev. **D 46**, 1973 (1992).
- [25] M. Glück, E. Reya and A. Vogt, Z. Phys. **C 67**, 433 (1995).
- [26] A.D. Martin, R.G. Roberts and W.J. Stirling, Phys. Rev. **D 50**, 6734 (1994).
- [27] A.D. Martin et al., Eur. Phys. J. **C 14**, 133 (2000).
- [28] A.D. Martin et al., Eur. Phys. J. **C 23**, 73 (2002).
- [29] V.N. Gribov and L.N. Lipatov, Sov. J. Nucl. Phys. **15**, 438 (1972).
- [30] L.N. Lipatov, Sov. J. Nucl. Phys. **20**, 94 (1975).
- [31] Yu.L. Dokshitzer, Sov. Phys. JETP **46**, 641 (1977).
- [32] G. Altarelli and G. Parisi, Nucl. Phys. B **126**, 298 (1977).
- [33] E.A. Kuraev, L.N. Lipatov and V.S. Fadin, Sov. Phys. JETP **45**, 199 (1977).
- [34] I.I. Balitsky and L.N. Lipatov, Sov. J. Nucl. Phys. **28**, 822 (1978).
- [35] P. Aurenche, J.P. Guillet and M. Fontannaz, Z Phys. **C 64**, 621 (1994).
- [36] G.A. Schuler and T. Sjöstrand, Phys. Lett. **B 376**, 193 (1996).
- [37] *Geant v3.13 modules GMOLI.FPP & GMOLS.FPP*, available on http://wwwasdoc.web.cern.ch/wwwasdoc/geant_html3/geantall.html.
- [38] B. Anderson et al., Phys. Rep. **97**, 31 (1983).
- [39] G. Marchesini et al., Comp. Phys. Comm. **67**, 465 (1992).
- [40] M. Bengtsson and T. Sjöstrand, Comp. Phys. Comm. **46**, 43 (1987).
- [41] T. Sjöstrand, Comp. Phys. Comm. **82**, 74 (1994).

- [42] T. Sjöstrand et al., *Comp. Phys. Comm.* **135**, 238 (2001).
- [43] G. Marchesini et al., *Comp. Phys. Comm.* **67**, 465 (1992).
- [44] G Corcella et al., *HERWIG 6.5 release note*, hep-ph/0210213 (2002).
- [45] B. Andersson et al., *Phys. Rept.* **97**, 31 (1983).
- [46] L. Lonnblad, *Comp. Phys. Comm.* **71**, 15 (1992).
- [47] G.F. Hartner, *VCTRAK Briefing: Program and Math* (unpublished). ZEUS-98-058, internal ZEUS-note, 1998.
- [48] A. Savin, *Study of Calorimeter Noise in the 1996 Data* (unpublished). ZEUS-98-007, internal ZEUS-note, 1998.
- [49] N. Tuning, *ZUFOS: Hadronic Final State Reconstruction with Calorimeter, Tracking and Backsplash Correction* (unpublished). ZEUS-01-021, internal ZEUS-note, 2001.
- [50] P.J. Bussey, *EUCCELL*. ZEUS Phantom Library.
- [51] J.E. Huth et al., *Research Directions for the Decade. Proceedings of Summer Study on High Energy Physics, 1990*, E.L. Berger (ed.), p. 134. World Scientific (1992). Also in preprint FERMILAB-CONF-90-249-E.
- [52] S. Catani, Yu.L. Dokshitzer and B.R. Webber, *Phys. Lett. B* **285**, 291 (1992).
- [53] S. Catani et al., *Nucl. Phys. B* **406**, 187 (1993).
- [54] D. Chapin, *A Measurement of Dijet Production in Neutral Current Deep Inelastic Scattering with ZEUS at HERA*. Ph.D Thesis, University of Wisconsin, Madison, 2001. Unpublished. .
- [55] R. Sinkus and T. Voss, *Nucl. Instrum. Meth. A* **389**, 160 (1997).
- [56] H. Abramowicz, A. Caldwell and R. Sinkus, *Nucl. Instrum. Meth. A* **365**, 508 (1995).
- [57] J. Repond, *ELEC5, An electron finding routine* ZEUS Phantom Library.
- [58] J. Repond,, *ELECRPOL, An electron finding routine* ZEUS Phantom Library.
- [59] J. Hamilton, *Prompt Photons in Photoproduction using the ZEUS detector at HERA*. Ph.D Thesis, University of Glasgow, Glasgow, 2005. Unpublished. .
- [60] E. brownson, S. Chekanov and S. Magill *Prompt photons with associated jets in photoproduction at HERA* Unpublished ZEUS note.

- [61] ZEUS Coll., S. Chekanov et al., Phys. Lett. **B 573**, 46 (2003).
- [62] P.R.B. Saull, *A Monte Carlo Generator for Deeply Virtual Compton Scattering at HERA*, 1999, available on <http://www-zeus.desy.de/physics/diff/pub/MC/> .
- [63] L.L. Frankfurt, A. Freund and M. Strikman, Phys. Rev. **D 58**, 114001 (1998).
- [64] T. Abe, Comp. Phys. Comm. **136**, 126 (2001).
- [65] T. Ishikawa et al., *GRACE manual: Automatic generation of tree amplitudes in Standard Models: Version 1.0*, KEK Report 92-19, 1993.
- [66] L.L. Frankfurt, A. Freund and M. Strikman, Phys. Lett. **B 460**, 417 (1999).
- [67] A.V. Belitsky, D. Müller and A. Kirchner, Nucl. Phys. B **629**, 323 (2002).
- [68] M. Fontannaz, J.P. Guillet and G. Heinrich, Eur. Phys. J **C 22**, 303 (2002).